Astrophysikalisches Institut Potsdam
Stellar Activity Group
An der Sternwarte 16
D-14482 Potsdam

ROBOTIC TELESCOPES & DOPPLER IMAGING

Measuring differential rotation on long-period active stars

Dissertation
zur Erlangung des akademischen Grades
„Doctor rerum naturalium“
(Dr. rer. nat.)

eingereicht an der
Mathematisch-Naturwissenschaftlichen Fakultät
der Universität Potsdam

von
Michael Weber

Potsdam, den 13. August 2004

Es ist nicht alles Schwindel,
aber das meiste.

Fontane

Everything you know is wrong.

Chumbawamba

Abstract

The sun shows a wide variety of magnetic-activity related phenomena. The magnetic field responsible for this is generated by a dynamo process which is believed to operate in the tachocline, which is located at the bottom of the convection zone. This dynamo is driven in part by differential rotation and in part by magnetic turbulences in the convection zone. The surface differential rotation, one key ingredient of dynamo theory, can be measured by tracing sunspot positions.

To extend the parameter space for dynamo theories, one can extend these measurements to other stars than the sun. The primary obstacle in this endeavor is the lack of resolved surface images on other stars. This can be overcome by the Doppler imaging technique, which uses the rotation-induced Doppler-broadening of spectral lines to compute the surface distribution of a physical parameter like temperature. To obtain the surface image of a star, high-resolution spectroscopic observations, evenly distributed over one stellar rotation period are needed. This turns out to be quite complicated for long period stars. The upcoming robotic observatory STELLA addresses this problem with a dedicated scheduling routine, which is tailored for Doppler imaging targets. This will make observations for Doppler imaging not only easier, but also more efficient.

As a preview of what can be done with STELLA, we present results of a Doppler imaging study of seven stars, all of which show evidence for differential rotation, but unfortunately the errors are of the same order of magnitude as the measurements due to unsatisfactory data quality, something that will not happen on STELLA. Both, cross-correlation analysis and the sheared image technique where used to double check the results if possible. For four of these stars, weak anti-solar differential rotation was found in a sense that the pole rotates faster than the equator ($\alpha < 0$), for the other three stars weak differential rotation in the same direction as on the sun was found ($\alpha >$).

Finally, these new measurements along with other published measurements of differential rotation using Doppler imaging, were analyzed for correlations with stellar evolution, binarity, and rotation period. The total sample of stars show a significant correlation of $|\alpha|$ with rotation period, but if separated into anti-solar and solar type behavior, only the subsample showing anti-solar differential rotation shows this correlation. Additionally, there is evidence for binary stars showing less differential rotation as single stars, as is suggested by theory. All other parameter combinations fail to deliver any results due to the still small sample of stars available.

Wissenschaftliche Zusammenfassung

Auf der Sonne sind viele Phänomene zu sehen die mit der solaren magnetischen Aktivität zusammenhängen. Das dafür zuständige Magnetfeld wird durch einen Dynamo erzeugt, der sich vermutlich am Boden der Konvektionszone in der sogenannten "Tachocline" befindet. Angetrieben wird der Dynamo teils von der differenziellen Rotation, teils von den magnetischen Turbulenzen in der Konvektionszone. Die differentielle Rotation kann an der Sonnenoberfläche durch beobachten der Sonnenfleckbewegungen gemessen werden.

Um einen größeren Parameterraum zum Testen von Dynamotheorien zu erhalten, kann man diese Messungen auch auf andere Sterne ausdehnen. Das primäre Problem dabei ist, dass die Oberflächen von Sternen nicht direkt beobachtet werden können. Indirekt kann man dies jedoch mit Hilfe der Doppler-imaging Methode erreichen, die die Doppler-Verbreitung der Spektrallinien von schnell rotierenden Sternen benützt. Um jedoch ein Bild der Sternoberfläche zu erhalten, bedarf es vieler hochaufgelöster spektroskopischer Beobachtungen, die gleichmäßig über eine Sternrotation verteilt sein müssen. Für Sterne mit langen Rotationsperioden sind diese Beobachtungen nur schwierig durchzuführen. Das neue robotische Observatorium STELLA adressiert dieses Problem und bietet eine auf Doppler-imaging abgestimmte Ablaufplanung der Beobachtungen an. Dies wird solche Beobachtungen nicht nur leichter durchführbar machen, sondern auch effektiver gestalten.

Als Vorschau welche Ergebnisse mit STELLA erwartet werden können dient eine Studie an sieben Sternen die allesamt eine lange (zwischen sieben und 25 Tagen) Rotationsperiode haben. Alle Sterne zeigen differentielle Rotation, allerdings sind die Messfehler aufgrund der nicht zufriedenstellenden Datenqualität von gleicher Größenordnung wie die Ergebnisse, ein Problem das bei STELLA nicht auftreten wird. Um die Konsistenz der Ergebnisse zu prüfen wurde wenn möglich sowohl eine Kreuzkorrelationsanalyse als auch die *sheared-image* Methode angewandt. Vier von diesen sieben Sternen weisen eine differentielle Rotation in umgekehrter Richtung auf als auf der Sonne zu sehen ist ($\alpha < 0$). Die restlichen drei Sterne weisen schwache, aber in der Richtung sonnenähnliche differentielle Rotation auf ($\alpha > 0$).

Abschließend werden diese neuen Messungen mit bereits publizierten Werten kombiniert, und die so erhaltenen Daten auf Korrelationen zwischen differentieller Rotation, Rotationsperiode, Evolutionsstaus, Spektraltyp und Vorhandensein eines Doppelsterns überprüft. Alle Sterne zusammen zeigen eine signifikante Korrelation zwischen dem Betrag der differenziellen Rotation und der Rotationsperiode. Unterscheidet man zwischen den Richtungen der differentiellen Rotation, so bleibt nur eine Korrelation der Sterne mit negativem α. Darüberhinaus zeigt sich auch, dass Doppelsterne schwächer differentiell rotieren.

Contents

List of Tables

List of Figures

1. Introduction

Since the discovery of variations of the Ca II H&K lines by Wilson (1978) it is known, that stars exhibit variations of their activity related parameters on many timescales. This is similar to the solar case, where the numbers of spots vary with a period of 11±1 years, superposed by a longer, more stochastic cycle which modulates the sunspot number in the cycle maximum. The original star sample from Wilson (1978) has been later extended to include stars which are less solar-like. This (still ongoing) project has shown that many stars show indeed a cyclic variation with periods similar to the 11 year sunspot cycle, and that some stars exhibit seemingly stochastic variations, while others exhibit no detectable variations.

These Ca II H&K measurements (Donahue et al. 1996) and photometric measurements (Hall 1991; Henry et al. 1995a) have been used to derive differential rotation on the stellar surfaces. If one assumes that the stellar rotation is constant in time, variations in the measured photometric periods could be caused by spots migrating to different latitudes. If the star rotates differentially (i.e. if the rotation rate is a function of latitude) this can be used to derive a measure for the differential rotations. Unfortunately, from this the question if the pole rotates faster than the pole or vice versa can not be answered. Since there is theoretical and observational evidence that antisolar differential rotation exists (Kitchatinov & Rüdiger 2004), an additional survey using a method that is capable of recovering the sign of the differential rotation is needed.

Doppler imaging has been used for a number of years to determine the direction and the magnitude of surface differential rotation of rapidly rotation stars (Donati & Collier Cameron 1997). Recently, evidence for anti-solar differential rotation on giant stars has been found (Strassmeier et al. 2003) and theoretical work has been done that links antisolar differential rotation to strong meridional circulation caused by large magnetic features.

The robotic observatory STELLA, which is equipped with a high-resolution spectrograph that is capable to deliver data for Doppler imaging, will become available soon. This facility will be the perfect instrument to perform a long term study of active stars to learn more about the correlation of differential rotation with other stellar parameters and if differential rotation stays constant with time or varies like suggested by Donati et al. (2003).

The remainder of this chapter gives a brief introduction into activity related phenomena on the Sun and on stars, a little more detailed look at differential rotation on the Sun, and an again brief overview of what theory has to say about the solar and stellar dynamos and differential rotation.

The second chapter explains the Doppler imaging technique in general and the specific code used for this work, while the third chapter introduces the robotic observatory STELLA and explains how it can be used as a Doppler imaging machine.

The last chapter presents the results of observations done with a telescope that was dedicated for Doppler imaging for almost ten weeks. This covers at least two stellar rotations for each of the stars in the sample, which is long enough to derive a measure for differential rotation in most cases with a certain reliability, but naturally too short to cover seasonal variations. Even though the quality of the data will be considerably better using STELLA, this data set gives a good impression on what can be achieved with a robotic telescope working as a Doppler imaging machine.

Finally, the appendix covers a few tests of our Doppler imaging program which have not been published so far. These have mainly to do with the inclusion of differential rotation.

1.1. Solar activity

On first sight, the Sun seems to be a very quiet star. It produces the (approximately) same amount of energy throughout the year, which is good for our life down here. But looking closer one can find many inhomogeneities like spots, plages, and eruptions which are mostly connected to some cyclic behavior. These phenomena are usually dubbed *solar activity*, since they seem to be in contrast with the usual solar quiescence as they are of non thermal origin. This section gives a very brief overview about activity-related phenomena seen on the Sun. See the web page of the NASA's Marshall Space Flight Center, of the Stanford Solar Center (solar-center.stanford.edu), the SOHO (sohowww.nascom.nasa.gov) mission pages or the excellent book by Stix (2004) for more in-depth information.

1.1.1. Sunspots

The most obvious of these activity related phenomena are the sunspots. The first records of sunspots in Europe have been made in the summer of 1612 by Galileo, a facsimile of one of his original drawings is shown in figure 1.1. Sunspots are dark spots appearing in an equatorial band approximately 35–40° north and south of the equator. The number of spots on the surface of the Sun varies considerably on the timescale of months, and the lifetime of one individual spot is approximately one solar rotation (26 days) or a little longer.

Since their discovery, sunspots have been studied in great detail. One of the most well known properties is, that sunspots come and go periodically. The period is 11 years in average, but the interval varies and can be 8 to 15 years. Sometimes (as last happened during the *Maunder* minimum from 1645–1715, no spots can be seen at all. Figure 1.2 shows the sunspot numbers since the *Maunder* minimum, which vary periodically but not quite regularly.

But not only the number of sunspot very throughout the 11 year cycle. At the beginning of the cycle sunspots emerge at higher latitudes than at the end of the cycle. Plotting the average sunspot area per latitude over time, one gets the butterfly diagram (figure 1.3). One can see, that at the end of each cycle, when there are still a few spots near the equator, the first spots from the new cycle appear already (at approximately 35° latitudes). Another property is Hale's polarity law,

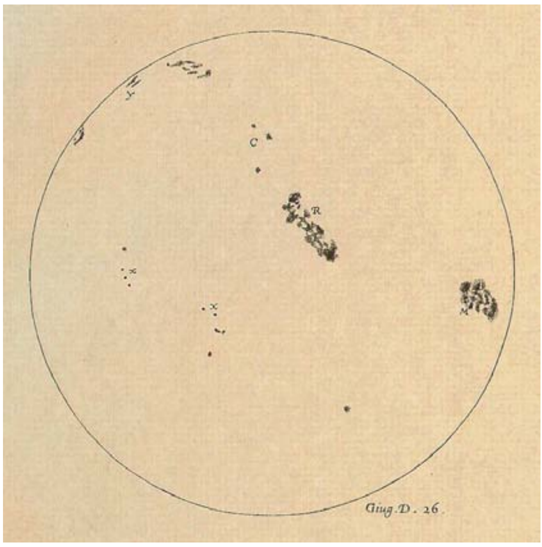

Figure 1.1.: This is the June 26 example of the sunspot drawings Galileo made in 1612 during the summer months, which were published in Istoria e Dimostrazioni Intorno Alle Macchie Solari e Loro Accidenti Rome (History and Demonstrations Concerning Sunspots and their Properties, 1613). Image courtesy of Biblioteca Nazionale Centrale Firenze.

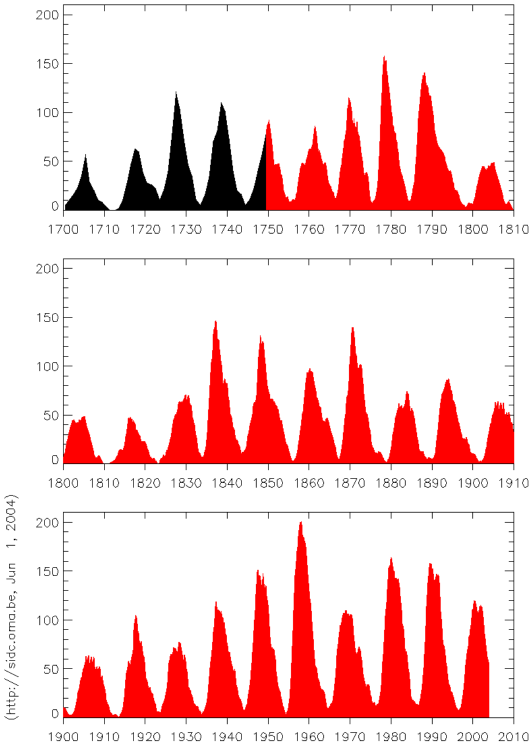

Figure 1.2.: The monthly sunspot number since 1750.The data before 1750 represent yearly averages. Image credit: SIDC, RWC Belgium, World Data Center for the Sunspot Index, Royal Observatory of Belgium, 2004.

which states that the polarity of the leading spot in one hemisphere is opposite that of the leading spots in the other hemisphere. These polarities change sign from one cycle to the next, extending the real solar cycle to 22 years. And last but not least there is Joy's law, which states that the linear extension of sunspot groups is tilted in respect to the east-west direction.

1.1.2. Plages and filaments

When looking at the Sun through an Hα or Ca II H&K filter one notices bright features, usually associated with sunspots visible in white-light images of the Sun. These bright regions, called plages, extend several thousand kilometers and are

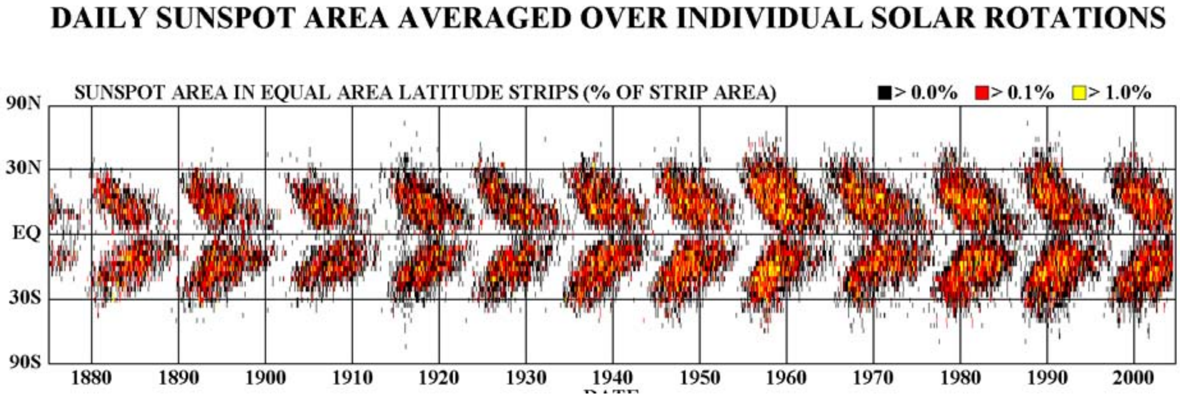

Figure 1.3.: Solar butterfly diagram for the last 120 years. Image courtesy NASA/NSSTC/HATHAWAY 2004.

approximately 300 K hotter than the Sun. Figure 1.4 shows one white-light image with only one small sunspot visible to the south-east of the disk center. The solar cycle is approaching a minimum at the time this image was taken. The Hα image taken at the same time shows an extended bright region at the same location.

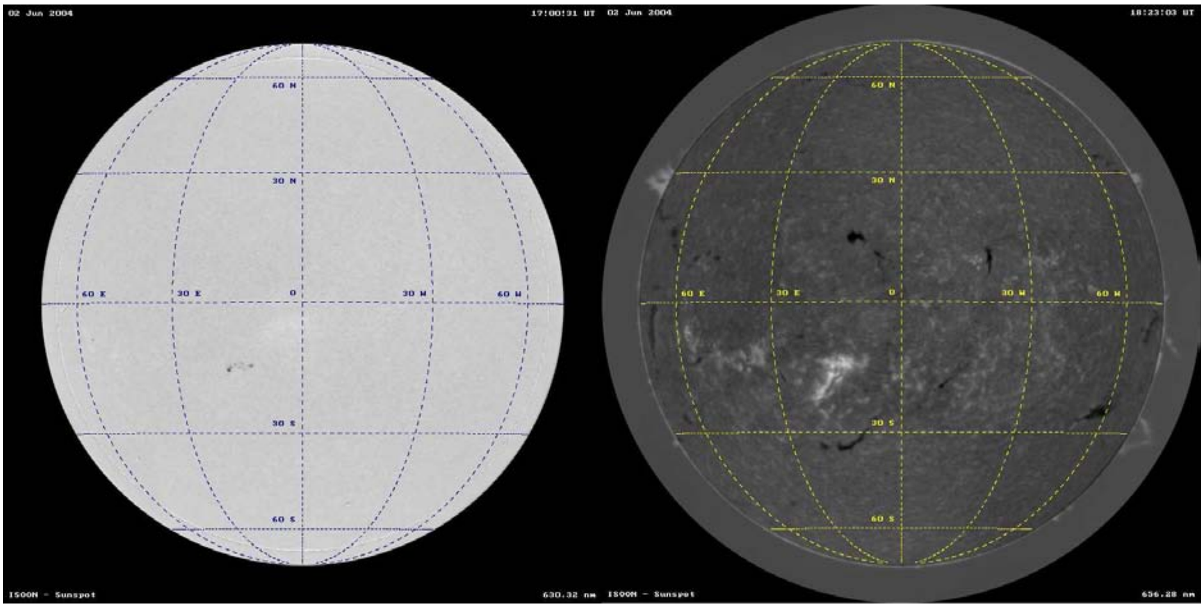

Figure 1.4.: Comparison of a white-light Sun image with a Hα image. Note the sunspot on the south-east of the center of the disk. Image courtesy US Air Force Research Laboratory and National Solar Observatory (Sacramento Peak)/AURA/NSF.

Also visible in figure 1.4 are dark string-like structures on the disk (filaments) and bright structures extending outward over the limb (prominences). These are condensations of cooler gas which seem dark if seen in front of the solar disk, but scatter light in our direction if seen above the solar limb. These features can be long lived and therefore can be seen travel across the solar disk.

1.1.3. Flares

Flares are huge explosions on the solar surface. They appear close to sunspots, usually between areas of opposite magnetic polarity. They release their energy in form of X-rays, gamma rays, particles, and mass flows. When a flare occurs close to a spot that is interconnected to another part of the solar surface, a flare can be triggered there simultaneously (see figure 1.5).

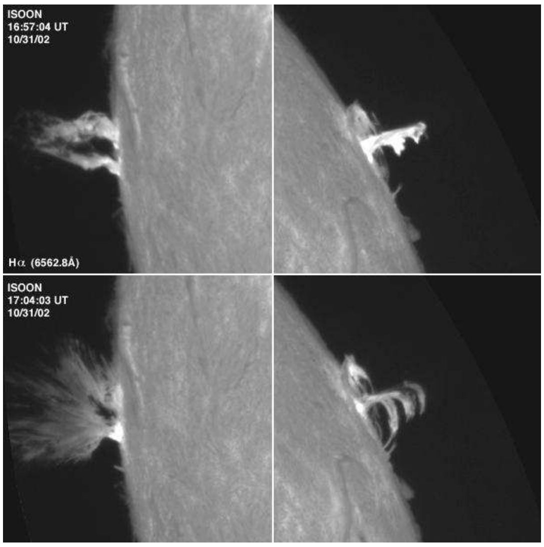

Figure 1.5.: A pair of flares that erupted on opposite sides of the Sun on 31 October 2002. Such events are known as sympathetic flare events. Image courtesy US Air Force Research Laboratory and National Solar Observatory (Sacramento Peak)/AURA/NSF.

1.1.4. Coronal mass ejections

Coronal mass ejections (CME) are huge bubbles of gas threaded with magnetic field lines that are ejected from the Sun over the course of several hours (see figure 1.6). They existence were unrealized before space observatories were available, because with ground based coronographs, only the innermost corona can be seen above the brightness of the sky. CMEs are very frequent, about one per week during quiet phases of the Sun up to two or three per day during solar maximum. If directed towards Earth, they can cause major electromagnetic disturbances.

1.1.5. Solar irradiance variation

Since solar activity maximum also means spot maximum, one expects the Sun to be fainter during solar activity maximum and brightest during its quiescent state. But in practise it is exactly opposite (see figure 1.7). In the visible part of the spectrum, the contribution of the (bright) plages is exceeding that of the (dark) spots. Since the optical part of the spectrum is dominant, the total irradiance follows that trend. If one would look only in e.g. the X-rays the effect would be a lot more pronounced, since the quiescent Sun does not emit any X-rays.

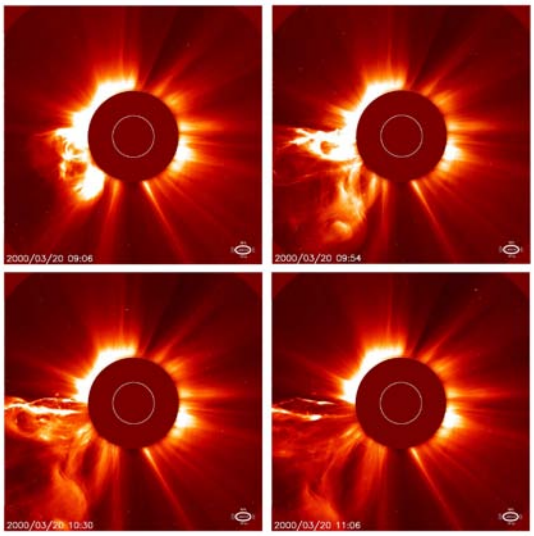

Figure 1.6.: A coronal mass ejection seen over the course of two hours. Image courtesy Solar & Heliospheric Observatory (SOHO). SOHO is a project of international cooperation between ESA and NASA.

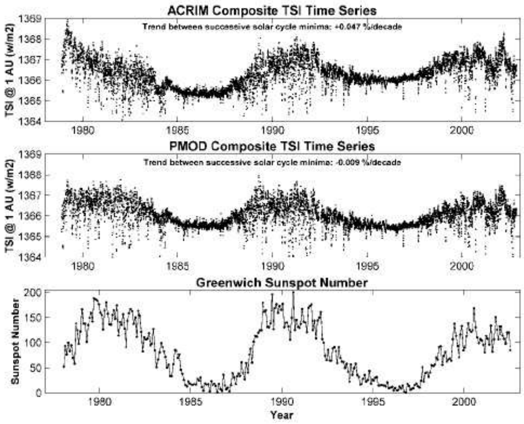

Figure 1.7.: Two different measures of the solar irradiance (ACRIM and PMOD) compared to the Greenwich sunspot number. Note that the Sun is brighter when it is most spotted. (from Willson & Mordvinov 2003).

1.2. Stellar activity

The term *Stellar activity* has been keyed in the mid of the last century to describe phenomena of the the solar-stellar connection. The availability of better observing technologies made it obvious that features connected to the solar activity (e.g. light variation due to spots and Ca II H&K emission and its modulation) can also be seen in stars. The following section gives a short introduction into this field.

1.2.1. Rotational modulation

In the mid of the 20th century it became clear, that there are stars that show periodic light variations which could best be explained with starspots. The idea of starspots producing light variations has been spooking around almost since the discovery of sunspots, but up until RS CVn (Hall 1976) and BY Dra (Bopp & Fekel 1977) systems have been identified, other mechanisms were responsible for the light variations.

Spots on the surface of rapidly rotating stars modulate the brightness of the star. An example for the light variation of a RS CVn binary system is shown in figure 1.8. A simple model of two spots on the stellar surface reproduce the pho-

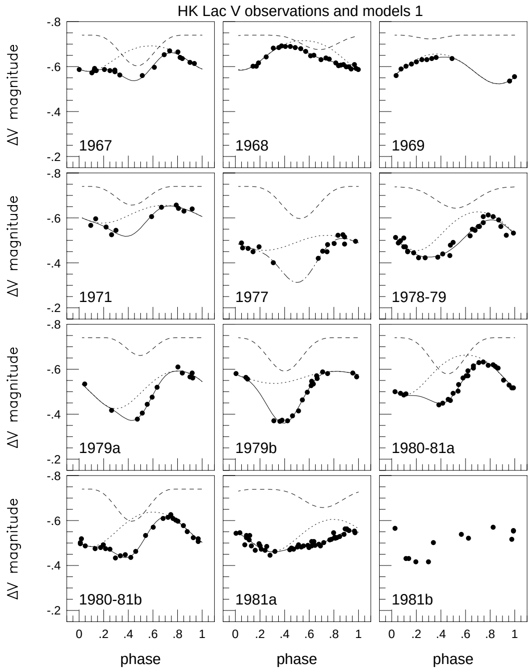

Figure 1.8.: Photometric light variation of the RS CVn binary system HK Lac. The lines are the two individual contributions of a two spot model and its total effect. (from Oláh et al. 1997).

tometric data very well. Applying such spot models to long term data can be used to track the variation of spot longitudes and spot sizes.

1.2.2. Stellar activity cycles

The discovery of stellar activity cycles by Wilson (1978) in solar-like stars made clear that indeed the mechanisms responsible for solar activity are universal. Due to its big success, the program was continued and expanded to include some stars that are not as solar-like as the original sample. Besides the before mentioned cycles in some of the stars (other stars show erratic variations while the rest appears practically constant), a correlation between the short term variation and the average activity level was found.

A sample of stars from Wilson's Ca II H&K survey is also monitored photometrically (Radick et al. 1998). This study shows that most stars become fainter as their activity level (as defined by the Ca II H&K flux) rises on small timescales (stellar rotation). This is exactly as is the case for the Sun. But on large timescales (activity cycles), the sample breaks down into two subgroups. The older stars (like the Sun) then become brighter as the activity cycle approaches a maximum, and the young stars which behave just oppositely (see figure 1.9).

1.3. Differential rotation on the sun

Differential rotation of the Sun has been measured since Carrington (1863), and a wealth of information has been published about this topic since then. Only a small but hopefully representative selection of this work is presented here. A much more detailed overview can be found in a review article by Beck (2000).

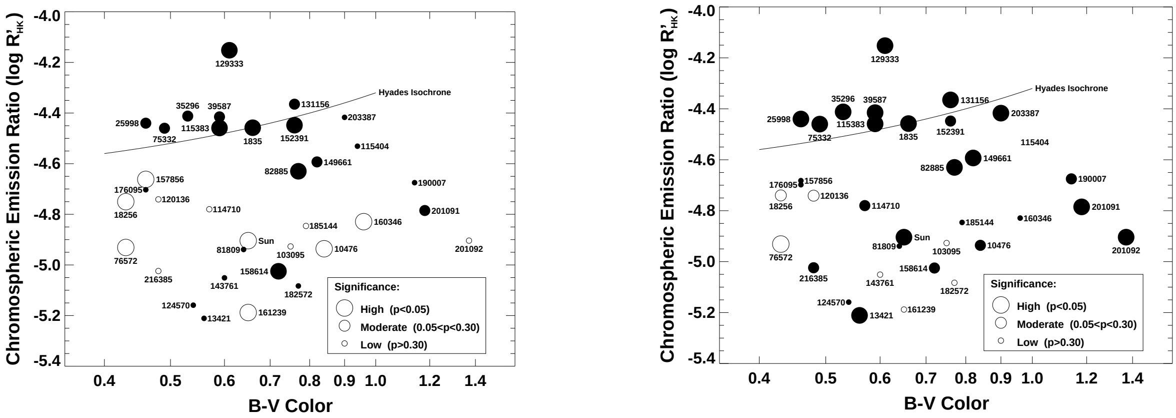

Figure 1.9.: Correlation between photospheric brightness variation and HK emission variation. **Left.** Long term variation. **Right.** Short term variation. Filled circles present anti-correlation between brightness and HK variation, open circles correlation. (from Radick et al. 1998).

1.3.1. Tracer measurements

The most straight forward way to measure the solar rotation rate is to measure the rotation of tracers on the solar surface. The earliest measurement, using sunspots as tracers, goes back to Carrington (1863), who measured the longitude and latitude of sunspots from 1855 to 1861 at Redhill observatory. Newton & Nunn (1951) used photographic images to measure the time when sunspots cross the meridian on two successive solar rotations. Recently, the sunspot positions measured off the white light images from Kodaikanal observatory have been merged with similar measurements from Mt. Wilson (Sivaraman et al. 1993, 2003). The dataset are very complimentary since the observatories are located at almost opposite geographic longitudes, and both cover solar images since the early 20th century up into the 1980s. The most surprising effect found, was a correlation between spot lifetime and first-day spot rotation rate (see figure 1.10). This can be explained by an evolution of anchor depth with spot lifetime, driven by magnetic buoyancy acting on the fluxtube causing the particular sunspot. This also explains the fact that recurrent sunspots rotate generally faster than young spots (Zappala & Zuccarello 1991).

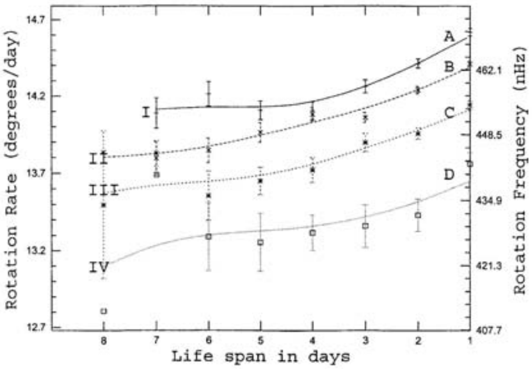

Figure 1.10.: First-day spot rotation for different latitudes and spot lifetimes. I, II, II and IV designate the latitude bands 1–10°, 10–20°, 20–30°, and 30–40°, respectively. A, B, C, and D mark the first day rotation rates for spots with a lifespan of only one day. The solid lines are spline fits to the data (Sivaraman et al. 2003).

Besides sunspots, magnetic features can also be used to determine the solar rotation rate. They have the main advantage over sunspots that magnetic features are visible on the whole solar disk and not restricted to certain latitude regions, and are visible during active and quiet states of the Sun. Meunier (1999) used maps from the MDI (Michelson Doppler Imager) instrument on the SOHO spacecraft and cross-correlates the consecutive images (taken 96 minutes apart) in longitude and latitude. He reports faster rotation and higher poleward meridional circulation during activity minimum, and also a decrease of the meridional circulation by a factor of two in active regions compared to the small magnetic structures outside the active regions.

Supergranulation is another tracer than can be used to detect the rotation rate of the Sun. Snodgrass & Ulrich (1990) correlated the 32 latitude bins of the Mt. Wilson magnetograms from 1967 to 1987 after removing the rotational pattern and limbshift effects and contributed the remaining velocity pattern to supergranulation.

1.3.2. Spectroscopic measurements

Spectroscopic measurements are most direct way to detect solar rotation since one can measure the exact Doppler shift of spectral lines at the corresponding optical depth all over the solar disc. Ulrich et al. (1988) use Mt. Wilson data to measure the solar rotation rate, as is done by several other groups. The results agree to a large extent, and in general the equatorial rotation rate derived is smaller than is the case for the tracer measurements above, while the differential rotation is roughly the same.

1.3.3. Helioseismology

The Sun oscillates in a very large number of acoustic oscillations (p modes) which get altered due to the solar rotation. By inverting the oscillation measurements, one can reconstruct the rotational behavior of the Sun throughout the convection zone. To measure the frequencies continuously there are currently two projects going on. One is the GONG project (Global Oscillations Network Group), which measures the oscillations on the Sun continuously from six sites distributed around the globe. The other project is onboard the SOHO spacecraft, the MDI/SOI (the Michelson Doppler Imager, Solar Oscillations Investigation). Both have in common that they monitor the Sun continuously, and both are in operation since about 1996.

The big advantage of this method over the others is its ability too look inside the solar convection zone. Figure 1.11 shows the variation of solar rotation with depth for several latitudinal bands. Note that after the tachocline (located at the bottom of the convection zone), the rotation rates are gradually increasing until the reach a maximum at about 0.95$R_\odot$. Then the rotation decelerates until it reaches the solar surface.

Additional to the depth variation, very accurate close-to-surface differential rotation has been measured since the start of these experiments (end of 1995 for GONG, approximately solar activity minimum). Figure 1.12 shows residual rotation of a layer 7 Mm below the solar surface. Bands of lower and higher rotational

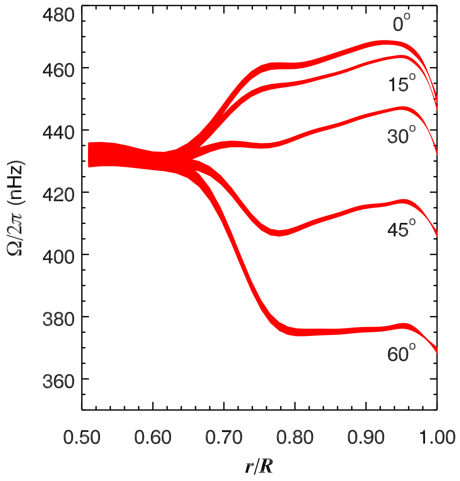

Figure 1.11.: Variation of the solar rotation rate with solar radius for five different longitudes. These are results from the GONG project (Courtesy of NSF's National Solar Observatory).

velocity move towards the equator as the solar activity develops from its near minimum at the start of the time series towards the solar activity maximum. This observation is compatible with torsional oscillation which are found when differential rotation and meridional circulation is subtracted from measured surface rotation rates (Zhao & Kosovichev 2004).

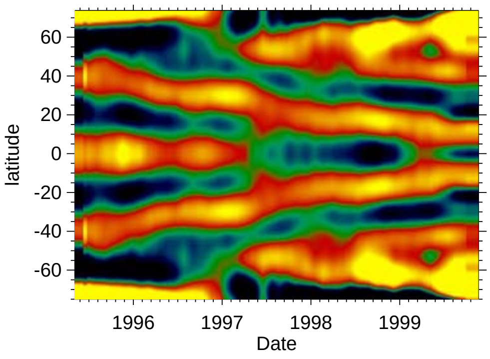

Figure 1.12.: Residual rotation rate close to the solar surface (about 7 Mm below). Bright colors indicate rotation rates faster than average, dark colors slower rotation rates. Clearly visible are bands of higher rotational velocity moving towards the equator (Image by Rachel Howe, Rudi Komm, Frank Hill/NSO/AURA/NSF).

1.3.4. Summary

Putting the different measurements together, the picture becomes almost complete. Fluxtubes, which are anchored at a certain depth as their surface, display the rotation rate of the anchor point. As the spot ages, the flux tube rises due to buoyancy and therefore accelerate until the reach approximately $0.95\,R_\odot$, the radius of the peak of the solar rotation rate. From there, the spot decelerates until it vanishes. Figure 1.13 shows functions of solar rotation with depth for different latitudes. The spot rotation rates depending on spot lifetime derived by Sivaraman et al. (2003) are projected onto these curves. Spots with a small lifetime appears to anchor very close to the surface, while long-living spot start out closer to the bottom of the convection zone. The spot rotation rate at the surface varies according to the rotation rate at the anchor depth. Figure 1.14 illustrates the variation of the rotation rate with age of the sunspot. When projecting the first-day rotation rate of a sunspot onto the subsurface rotation curve, one gets a radius somewhere in the middle of the convection zone for short lived spots, and a radius close to the bottom of the convection zone for long lived spots. The evolution of the rotation rate with sunspot age suggests that the anchor point of the sunspot rises and therefore the spot rotation rate increases in general.

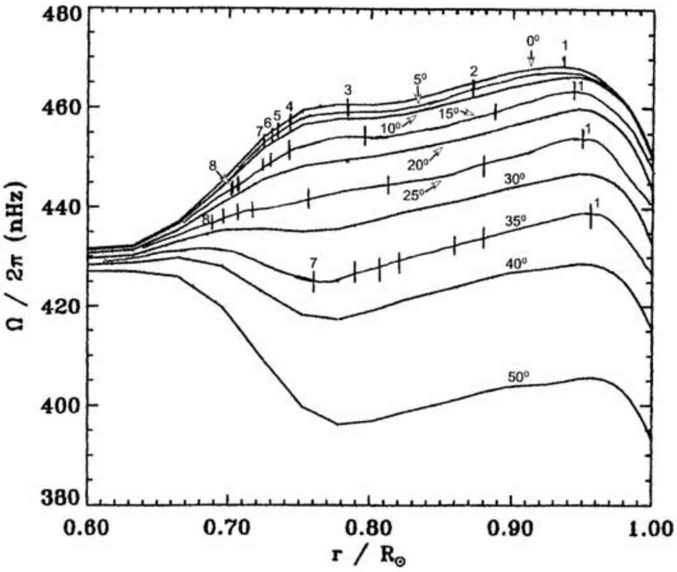

Figure 1.13.: First-day rotation rates of sunspots at certain latitudes. The rate is then projected onto the GONG data for the corresponding latitude, and the lifetime of the spot is noted on the intersecting point (Sivaraman et al. 2003).

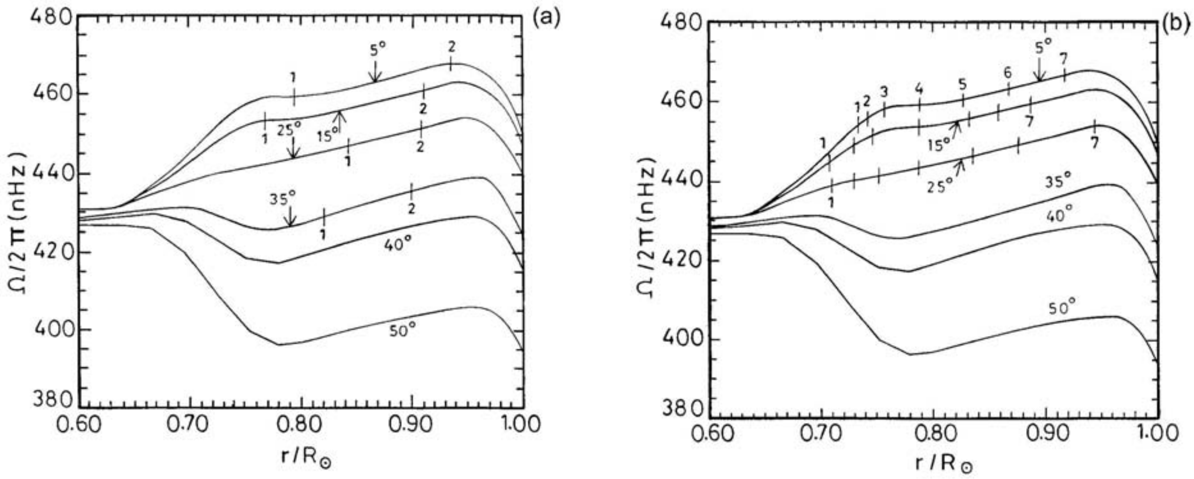

Figure 1.14.: Rotation rates of sunspots with age and lifetime of the spot. The rate is then projected onto the GONG data for the corresponding latitude. The left panel shows short-lived spots, the right panel spots with a life span of up to seven days, which is the longest possible value (Sivaraman et al. 2003).

1.4. Solar dynamo models

A short overview over aspects of current global mean field dynamo models relevant of this work is given here. A detailed analysis of the solar dynamo can be found in the recent review by Ossendrijver (2003), and a very extensive review about general astrophysical dynamos has been done by Brandenburg & Subramanian (2004).

1.4.1. Mean-field theory of the solar dynamo

The complex flow fields in the solar convection zone make it impossible to analytically solve the induction equation, but the main interest of dynamo theory lies in the large-scale magnetic field. This can be accomplished by averaging, so that only statistical properties of the large fields need to be known (Steenbeck et al. 1966; Hoyng 1992). For example the magnetic field is split to a mean (index 0) and a fluctuating (index 1) part $\boldsymbol{B}_0 \equiv \langle \boldsymbol{B} \rangle$ and $\boldsymbol{B}_1 \equiv \boldsymbol{B} - \langle \boldsymbol{B} \rangle$. By averaging the induction equation and subtracting the mean, and with $\mathcal{D}_0 \boldsymbol{B} = \nabla \times (\boldsymbol{U}_0 \times \boldsymbol{B} - \eta \nabla \times \boldsymbol{B})$ and $\mathcal{D}_1 \boldsymbol{B} = \nabla \times (\boldsymbol{U}_1 \times \boldsymbol{B})$, one gets

$$\frac{\partial \boldsymbol{B}_0}{\partial t} = \mathcal{D}_0 \boldsymbol{B}_0 + \boldsymbol{\epsilon} \tag{1.1}$$

$$\frac{\partial \boldsymbol{B}_1}{\partial t} = \mathcal{D}_0 \boldsymbol{B}_1 + \mathcal{D}_1 \boldsymbol{B}_0 + \boldsymbol{G}, \tag{1.2}$$

where $\boldsymbol{\epsilon} \equiv \langle \boldsymbol{U}_1 \times \boldsymbol{B}_1 \rangle$ is the turbulent electromagnetic force (EMF) and $\boldsymbol{G} \equiv \mathcal{D}_1 \boldsymbol{B}_1 - \langle \mathcal{D}_1 \boldsymbol{B}_1 \rangle$. To derive a closed equation for $\boldsymbol{B}_0$, $\boldsymbol{G}$ is assumed to vanish. This is called *first-order smoothing approximation* (FOSA), or *second order correlation approximation* (SOCA) and can be justified if at least one of the following conditions is satisfied:

- $|\boldsymbol{G}| \ll |\mathcal{D}_1 \boldsymbol{B}_0| \Leftrightarrow |\boldsymbol{B}_1 \ll \boldsymbol{B}_0|$
- $|\boldsymbol{G}| \ll |\mathcal{D}_0 \boldsymbol{B}_1| \Leftrightarrow \mathrm{Rm} \ll 1$ or $U_1 \ll U_0$
- $|\boldsymbol{G}| \ll |\partial \boldsymbol{B}_1 / \partial t| \Leftrightarrow S \ll 1$

In the Sun, the first two conditions are not satisfied, and the last condition may be marginally satisfied. If S (the ratio of correlation time to turnover time) < 1, considering higher order approximations may be useful. If $S \geq 1$, other methods need to be used.

For convection in a rotation sphere, one can write the EMF as:

$$\boldsymbol{\epsilon} = \boldsymbol{\alpha} \circ \boldsymbol{B}_0 + \boldsymbol{\beta} \circ \mathrm{curl} \boldsymbol{B}_0 + \ldots \tag{1.3}$$

Using FOSA, one obtains

$$\alpha \approx -\frac{1}{3} \tau_c \langle \boldsymbol{u} \cdot \boldsymbol{\omega} \rangle \tag{1.4}$$

$$\beta_1 \approx \frac{1}{3} \tau_c \langle |\boldsymbol{u}^2| \rangle, \tag{1.5}$$

where α describes the famous α-effect, while $\beta_1 \equiv \eta_t$ is the scalar turbulent diffusivity.

Using a very simple solar model which takes only the differential rotation $\boldsymbol{U}_0 = \Omega(r,\theta)r\sin\Theta\boldsymbol{e}_\phi$, one α effect $\alpha_1\boldsymbol{e}_r\boldsymbol{e}_z = \alpha_1\cos\Theta$ and scalar turbulent diffusion η_t into account, one gets

$$\frac{\partial\boldsymbol{B}_0}{\partial t} = \nabla\times(\boldsymbol{U}_0\times\boldsymbol{B}_0 + \alpha_1\cos\Theta\boldsymbol{B}_0 - \eta_t\nabla\times\boldsymbol{B}_0). \tag{1.6}$$

If one decomposes the magnetic field into poloidal and toroidal components ($\boldsymbol{B}_0 = B_{0t}\boldsymbol{e}_\phi + \nabla\times A_{0p}\boldsymbol{e}_\phi$) one sees, that differential rotation converts B_{0p} into B_{0t}, and the α effect generates B_{0p} from B_{0t} and vice versa. Turbulent diffusion leads to enhanced decay and diffusive transport on time scales of $\tau_d \equiv L^2/\eta_t$.

One can define a dynamo number

$$D = D_\alpha D_\Omega \equiv \frac{\alpha_1 L}{\eta_t}\cdot\frac{\Delta\Omega L^2}{\eta_t}. \tag{1.7}$$

L is the typical length scale of the dynamo, $\Delta\Omega$ the typical difference in rotation rate, and also α_1 and η_t are understood to be typical values. The numbers D_α and D_Ω represent turbulent magnetic Reynolds numbers, and dynamo action (defined as exponential growth of $\boldsymbol{B}_0$) occurs if $|D|$ exceeds a geometry dependent critical value.

On the Sun, α_1 is believed to be $\approx 0.1\mathrm{ms}^{-1}$, η_t is of the order of $2\cdot10^7\mathrm{m}^2\mathrm{s}^{-1}$, $L\approx 2\cdot10^8\mathrm{m}$, and $\Delta\Omega\approx 2.5\cdot10^{-7}\mathrm{s}^{-1}$. Using these values, one finds τ_d to be approximately 100 years, $|D_\alpha|\approx 2$, and $D_\Omega\approx 10^3$. Thus $|D_\alpha| \ll D_\Omega$, which justifies the $\alpha\Omega$-approximation, which ignores the α effect in the equation of the toroidal mean magnetic field. If the two dynamo numbers are of the same order of magnitude, the dynamo is of $\alpha^2\Omega$-type, if $|D_\alpha| \gg |D_\Omega|$ the dynamo is of α^2-type. For an $\alpha\Omega$-dynamo, $|\boldsymbol{B}_{0p}|/|\boldsymbol{B}_{0t}| \approx |D_\alpha/D_\Omega|^{-1/2}$, which explains why $|\boldsymbol{B}_{0t}| \gg |\boldsymbol{B}_{0p}|$ in the Sun. The ratio is of the order of one for an α^2-dynamo.

1.4.2. Mean-field theory of rotation

Similar to the technique outlined before, one can make a mean-field theory of stellar convection and rotation (Rüdiger 1989). The azimuthal average of the angular momentum is:

$$\frac{\partial}{\partial t}\rho s^2\Omega + \nabla\cdot(\rho s^2\Omega\boldsymbol{U}_{0m} + \rho s\langle u_\phi\boldsymbol{u}\rangle) - L_\mathrm{M} = 0, \tag{1.8}$$

where $s \equiv r\sin\Theta$ and

$$L_\mathrm{M} \equiv \frac{1}{\mu_0}\nabla\cdot s(B_{0\phi}\boldsymbol{B}_0 + \langle b_\phi\boldsymbol{b}\rangle) \tag{1.9}$$

represents the Lorentz torque. Using FOSA-like assumptions, one can derive an expansion of the turbulent Reynolds stress tensor $Q_{ij} \equiv \langle u_i u_j\rangle$ in terms of the mean rotation. The most important (azimuthal) coefficients are

$$Q_{r\phi} \approx -\nu_\mathrm{t} s\frac{\partial\Omega}{\partial r} + \Lambda_\mathrm{r}\Omega\sin\Theta \tag{1.10}$$

$$Q_{\Theta\phi} \approx -\sigma\nu_\mathrm{t}\sin\Theta\frac{\partial\Omega}{\partial\Theta} + \Lambda_\mathrm{h}\Omega\sin\Theta, \tag{1.11}$$

with ν_t being the turbulent kinematic viscosity and σ a scaling factor. The diffusive terms try to establish a uniform rotation, while the terms containing the Λ-effect are responsible for angular momentum transport. The radial Λ-effect is responsible for establishing $\partial\Omega/\partial r$, while Λ_h and the meridional circulation both contribute to $\partial\Omega/\partial\Theta$.

Applications of the mean-field theory of rotation

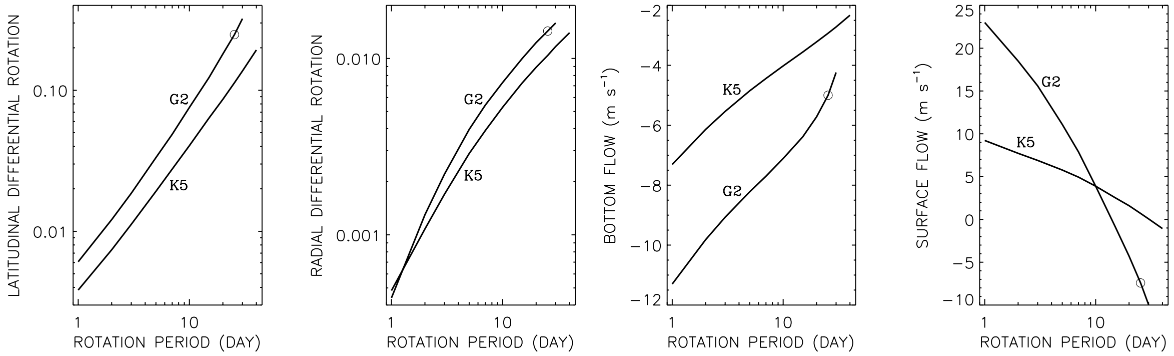

Figure 1.15.: Latitudinal and radial differential rotation (left) and meridional flow (right) for G2 and K5 MS dwarfs. The circles represent the Sun. (Kitchatinov & Rüdiger 1999).

Kitchatinov & Rüdiger (1999) modeled the dependence of differential rotation and meridional flow for a model G2 (Sun) and K5 dwarf star from the solar rotation period down to a rotation period of one day. They find that differential rotation and meridional flow at the bottom of the convection zone increases with rotation period, while the surface flow decreases and even changes its sign (see Fig. 1.15). Fitting a power law $\Delta P/P = P^{n'}$ to these curves, they find a variable slope of n'=1 for the fastest rotator and a slope of 1.56 for the solar rotation rate, the average being 1.15 for the G2 stars. For the K5 stars, those values are 0.95, 1.21, and 1.04, respectively.

Küker & Stix (2001) calculate the rotation pattern for the Sun at various evolutionary stages (from PMS to present) and for various rotation rates (see Fig. 1.16). They find a good agreement between their present day solar model and the observed velocity fields on the Sun, even though details at the surface and the tachocline are not well reproduced. This also results in a contradictory sign of the surface meridional circulation. For earlier evolutionary stages they find that differential rotation plays a smaller role, which is in agreement with the assumption that the magnetic activity of PMS stars comes from a α^2-dynamo (Küker & Rüdiger 1997).

Recently, Kitchatinov & Rüdiger (2004) extended their model (Kitchatinov & Rüdiger 1999) to include the possibility of antisolar differential rotation due to deviations from spherical symmetry in the gravity or temperature distribution on stars. Gravity inhomogeneities could be due to a binary component, while temperature inhomogeneities are common features in active late-type stars. They use a model of a giant star with a higher than normal rotational velocity. Modeling for the non-magnetic case results in solar-like differential rotation, but adding

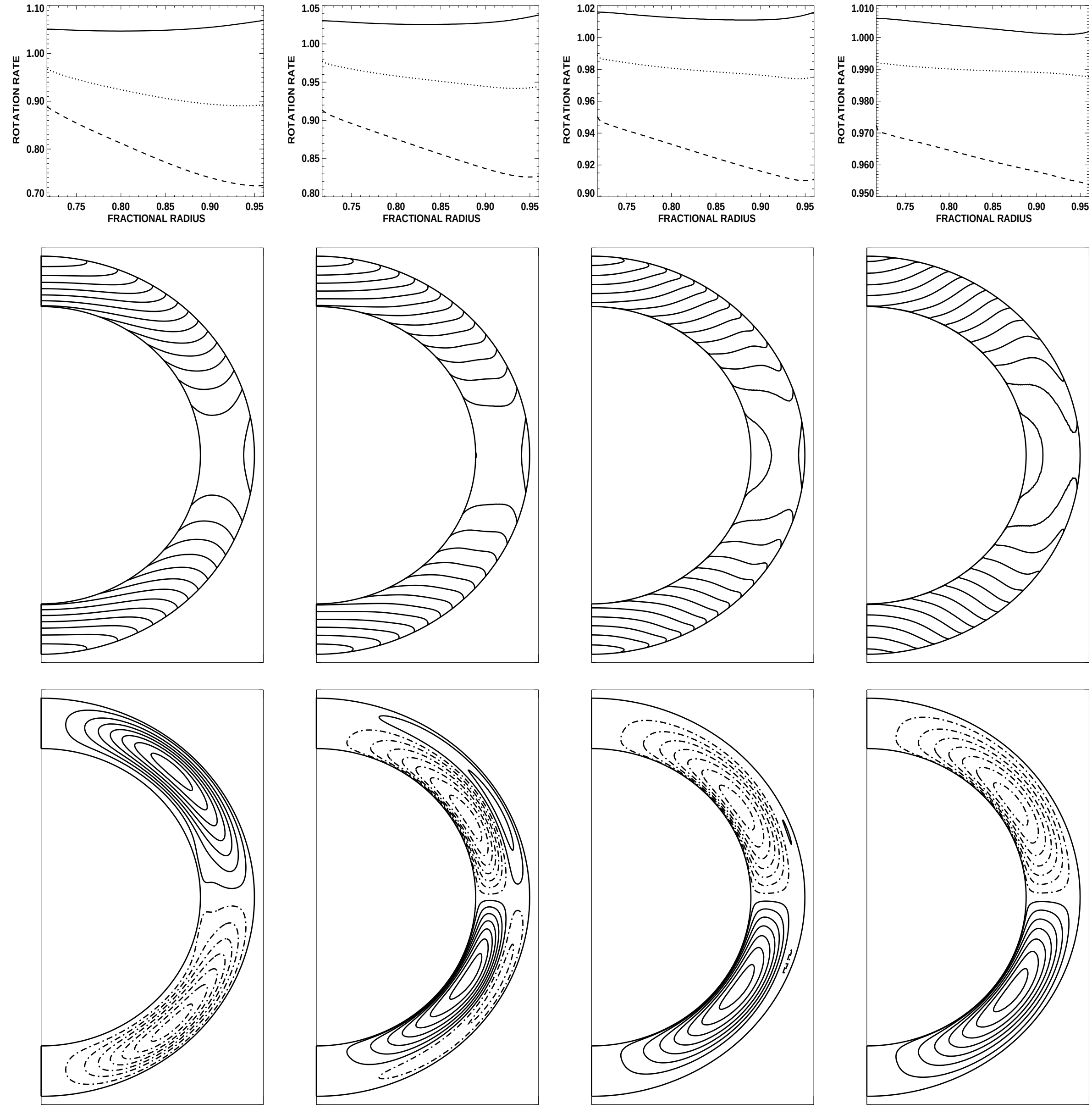

Figure 1.16.: Model of the solar differential rotation and meridional circulation at rotation periods of 56, 28, 14, and 7 days (Küker & Stix 2001).

a poloidal field at first decreases the amount of differential rotation and finally changes its sign above a magnetic field strength of ≈ 200G. The results confirm well with HD 31993 (Strassmeier et al. 2003), the only single star observed so far with undisputed anti-solar differential rotation. The case of gravity inhomogeneities has yet to be modeled.

2. Doppler Imaging

2.1. The principle

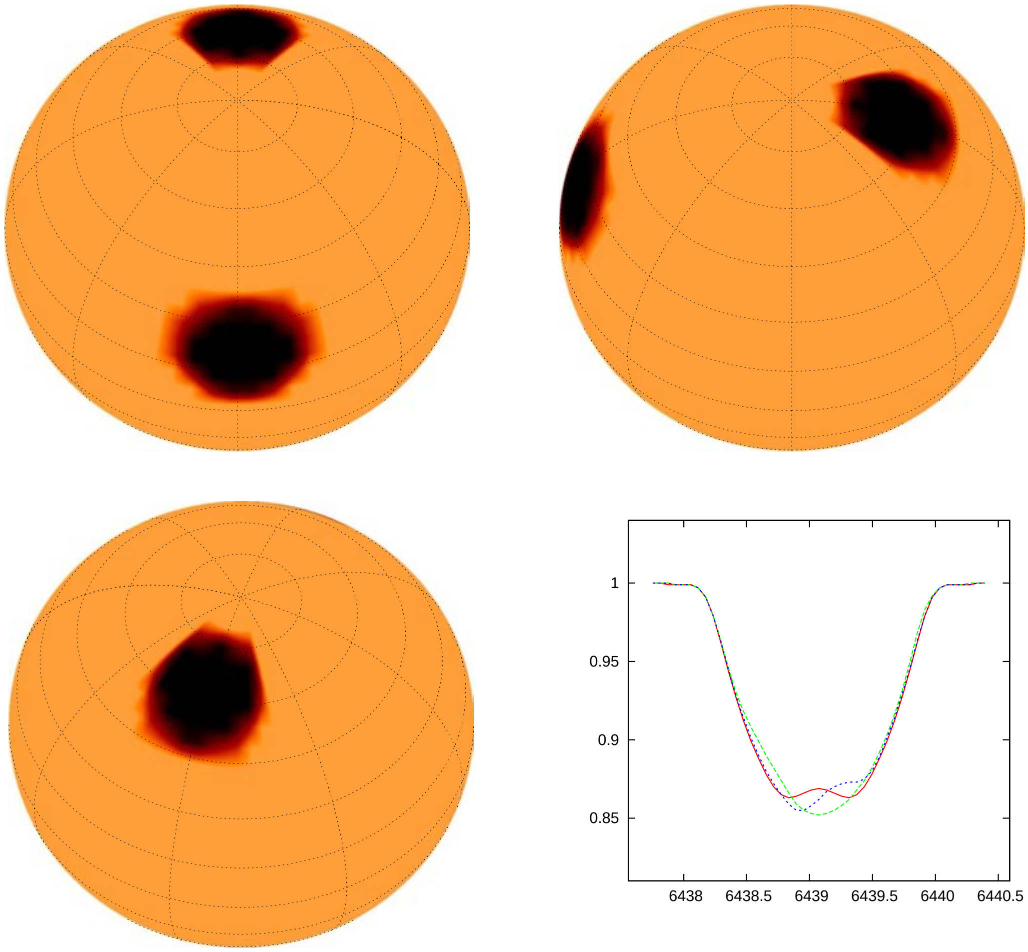

Figure 2.1.: Principle of Doppler imaging: A cool spot on the surface of the star usually emits less light in a specific line than the surrounding continuum. The result is a bump in the line profile center if the spot is in the center of the stellar disk, or in the blue or red line wing if the spot rotates into or out of sight, respectively. The solid, dashed, and dotted belong to the first, second, and third rotational phase, respectively.

The basic idea of Doppler imaging is simple: If a rapidly rotation star has a big dark spot on its surface, the flux that would origin at that spot is missing in the observed spectrum. The sign of such a spot is therefore a bump in the line profile, since the missing absorption results into a (pseudo-)emission. The position of the bump in the line profile is determined by the Doppler shift caused by the rotational velocity of the spot. This is illustrated in figure 2.1 with a very simple cartoon-star.

If one observes a star with spots throughout a rotation period, it is possible to reconstruct the spot configuration on the stellar surface. The spot longitudes can determined very accurately, but the signatures of the spot latitudes are more subtle. A low latitude spot moves all the way through the spectral line, while a high latitude spot can only be seen close to the center of the spectral line. The extreme case is a symmetrical polar spot which stays constant regardless of the rotational phase. If the star's rotational axis is perpendicular to the line of sight, no distinction between the two hemispheres can be made. If the axis is inclined, this ambiguity is resolved, but part of the stellar surface remains invisible. The extreme case being a star seen pole-on, where one half of the star is permanently invisible. In this case the surface elements do not exhibit Doppler shift because of the lack of a velocity component in the line-of-sight direction, and therefore Doppler imaging fails.

2.2. Prerequisites

From the simple view sketched above it is already clear that only a few special stars can be imaged using this technique.

2.2.1. Projected rotational velocity

The rule of thumb is, that the projected rotational velocity $v \sin i$ should be at least $20 \mathrm{km\,s}^{-1}$. This corresponds to a half-width of the spectral line of 0.4Å, which again corresponds to a resolution of eight surface elements if a spectral resolution of 0,1Å (64,000) is available. Of course the surface resolution in this example is better than 1/8, following a similar argument as is true for resolving double stars. One can in principle increase the spectral resolution to increase also the surface resolution, but the practical lower limit is the intrinsic line width of the star, which is mostly caused by turbulent convection on the star. Thus, a $v \sin i$ of $10 \mathrm{km\,s}^{-1}$ poses a quite rigid lower limit.

Since most stars are seen under an inclination angle i, the true rotational velocity has to be higher by the factor $1/\sin i$. True solar-like stars are therefore out of reach of this technique, thus for late-type stars one can only observe stars which are strange in terms of (at least) rotational velocity compared to most such stars. This imposes a methodological bias one has to be aware of.

2.2.2. Signal strength & phase smearing

To construct a reliable Doppler image, one needs data with a signal/noise ratio of at least 200. Multiline techniques like least-squares deconvolution (LSD, see e.g. Donati & Collier Cameron 1997) can be used to boost the signal strength, or filtering techniques (Savanov 2004) can be applied to loosen the requirements to a signal/noise ratio of about 30.

Unfortunately, another restriction plays a role here: Phase smearing. While a spectrum is taken, the star continues to rotate. Keeping the phase smearing below 1° is easy for long period stars. A star with a rotation period of 20 days takes 80 minutes to rotate that far, thus the signal/noise ratio can be improved by exposing as long as possible. For a star with a rotation period of 3 days, this time shrinks already to 12 minutes, while for very fast rotators with 0.5 days rotation period it takes only two minutes to rotate one degree.

The signal strength also connects to the spectral resolution mentioned above. If one would have an ideal spectrograph-camera which delivers a continuous spectrum, one would have to find a balance between spectral resolution and signal/noise ratio which depends on the specific implementation of the Doppler imaging technique used.

2.2.3. Rotation period & phase coverage

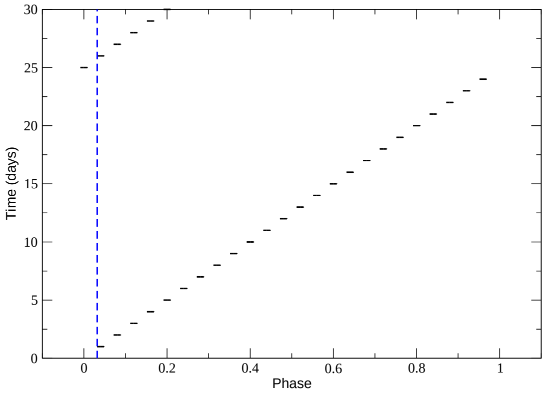

Figure 2.2.: Example phase diagram for a star with a rotation period of 25 days. Solely one observation per night has to be done to obtain a good phase coverage, but phase gaps take another 25 days to be filled.

The simplest case from a phase coverage point-of-view are stars with rotation periods of approximately 10 days and longer. One simply takes one or two spectra each night until at least one stellar rotation is fully covered (see Fig.2.2). This requires a very long continuous observing run, and can easily fail if a continuous block of observing time is clouded out. In the case of a star with a 10 day period, 7 continuous good days are not enough. This makes Doppler imaging an ideal program for robotic telescopes.

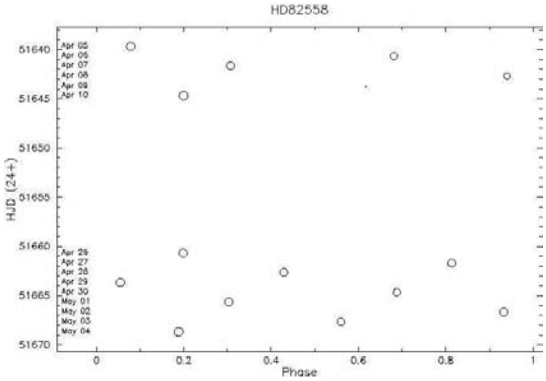

Figure 2.3.: Example phase diagram for LQ Hya, a star with a rotation period of 1.6 days.

A similar case are stars with rotation periods of less than half of a day. These stars are usually observed during a whole night, and the individual spectra are later combined to obtain a good balance between signal strength and phase smearing.

More tricky are the stars which have such rotation periods, that they can not be observed within one rotation. To keep the possibility of spot reconfiguration small, one tries to obtain a good phase distribution in as few nights as possible. Careful planning of these observations is required, which again calls for a robotic telescope to do these routine tasks. Fig. 2.3 shows an example of a star where the rotation period of 1.6 days makes it easy to cover many different phases in a few nights. The top part of this figure also shows that it is impossible to make up for bad weather if the observation's schedule is fixed.

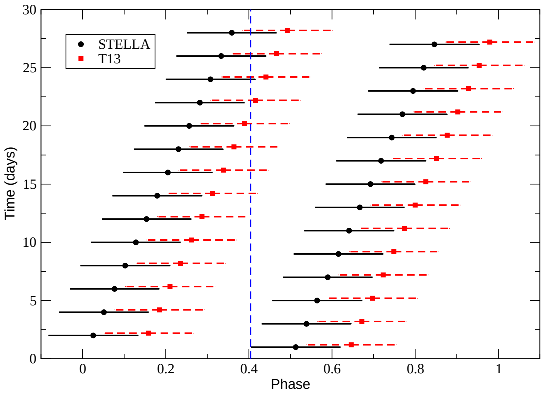

Figure 2.4.: Example phase diagram for EI Eri, a star with a rotation period of 1.95 days. The black lines correspond to the observable phases from the STELLA site, while the red lines correspond to observations done in Arizona (T13 is a Tennessee-state university telescope situated at Fairborn observatory)

A very special example of a star with an unfriendly rotation period is EI Eri. It's 1.95 days period makes it necessary to observe for three weeks to get a full phase coverage (Fig. 2.4). Since this includes ten stellar rotations, changes on the stellar surface are quite probable during this time. In this case, observations from another observatory, preferably far away in a longitudinal sense, greatly improve the situation (see red part of Fig. 2.4). Shown in this figure are observable phases from STELLA (black lines) and from T13 or any other telescope in Arizona (red lines). Again, a robotic observatory can be very helpful, because it can be forced to observed at the same time as an observing block is granted at a non-robotic telescope in a different part of the world.

2.3. TEMPMAP

The Doppler imaging program TEMPMAP used here is described in detail by Rice et al. (1989), and is based on the numerical solution of this inverse problem by Goncharskii et al. (1977, 1982):

$$R^*(\lambda,\phi) = \frac{\int\int I(M,\theta)R[M,\theta,\lambda+\Delta\lambda_D(M,\phi)]\cos\theta dM}{\int\int I(M,\theta)\cos\theta dM} \tag{2.1}$$

where

$R^*(\lambda,\phi)$	observed line profile depth at wavelength λ and phase ϕ
I	continuum intensity
M	position on the stellar disk (longitude/latitude pair)
θ	angle between normal to the stellar surface and line of sight
$\Delta\lambda_D(M,\phi)$	Doppler shift at position M due to the stellar rotation at phase ϕ
R	local line depth at position M

The integrations are over the visible disk of the star. This is a set of coupled integral equations, where each wavelength bin and each observational phase make up one equation.

Using a simple model for the intrinsic line profile one can attempt to solve these equations, but the problem turns out to be ill posed, because there are an infinite number of solutions consistent with the observations. The problem needs to be regularized. Two common methods are implemented in TempMap: Maximum Entropy, where entropy is defined as (again integration is over the surface of the star)

$$S(\tau) = -\int\int f(\tau(M))dM, \tag{2.2}$$

f being a suitable defined function and $\tau(M)$ the optical depth.

One now has to minimize the functional

$$M^\alpha(\tau) = \Phi(\tau) + \alpha S(\tau) \tag{2.3}$$

where $\Phi(\tau)$ is the discrepancy between observed and computed line profiles R_O^* and R_C^*, respectively

$$\Phi(\tau) = \sum_\lambda \sum_\phi [R_C^*(\lambda,\phi) - R_O^*(\lambda,\phi)]^2. \tag{2.4}$$

Various expressions can be used for the smoothing function $f(M)$, the results usually don't differ significantly from each other if the signal/nose ratio is sufficiently high:

$$f(M) = (\frac{\partial\tau}{\partial l})^2 + (\frac{\partial\tau}{\partial b})^2 \tag{2.5}$$

$$f(M) = \tau(M)\ln\tau(M) \tag{2.6}$$

If not otherwise noted, the Maximum Entropy Method (MEM, equation 2.6) is used throughout this work. As noted above, the differences between the two regularization functions are very small (cf. Rice et al. 1989). MEM tries to minimize the information content, while the Tikhonov regularization (equation 2.5) tries to correlate neighboring pixels.

2.3.1. TempMap modifications

Two small modifications were made to the TempMap code as described by Rice et al. (1989) and Rice & Strassmeier (2000), both are related to the treatment of differential rotation (i.e. a latitude-dependent rotation rate).

The first modification is done to the rotational profile of the spectral line. The rotational velocity for a surface element for a rigid rotator is $v = v_{\mathrm{equ}} \sin i \cos b \sin l$, b being the latitude and l the longitude. For a star with the differential rotation parameter $\alpha = \delta\Omega/\Omega$, the additional term $(1 - \alpha \sin^2 b)$ has to be added, which make the pole lag behind the equator for positive α.

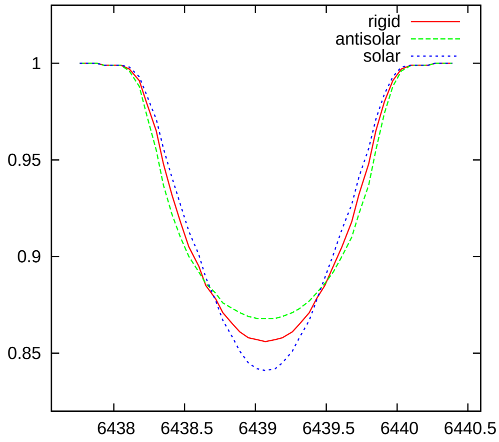

Figure 2.5.: Influence of differential rotation on the shape of the integrated line profile. A (approximately solar) value of α=±0.25 was used for this plot.

The influence of the differential rotation parameter α on the shape of the integrated line profile is illustrated in figure 2.5. Solar-type differential rotation creates a line profile that is more pointed than for the rigid rotator case. Antisolar differential rotation creates a flat line core, which somewhat resembles the effect of a polar spot.

The second modification takes into account that the differential rotation changes the location of the spots in time.

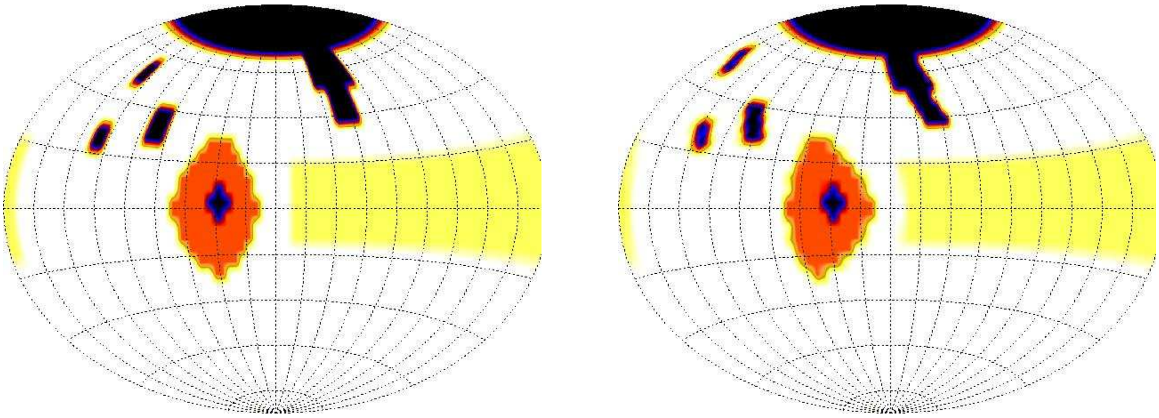

Figure 2.6.: Influence of differential rotation on the spot positions. The image at the left is the initial spot configuration of an artificial test star, the image at the right is the final configuration after two stellar rotations (cf. appendix A).

The resulting phase shift is illustrated in figure 2.6 for solar-like differential rotation. The plots present the star in the rest frame of the equator, thus the spots appear to move to smaller phases, i. e. they lag behind the equator. These two images are part of the test-case discussed later in appendix A.

3. STELLA

The STELLA[1] observatory is a new robotic observatory dedicated to research in stellar activity. Similar to the Mt. Wilson Ca II H&K survey[2], a sample of stars will be monitored for an extended period of time. This will be done by producing resolved surface temperature maps (using the *Doppler imaging* technique) periodically to look for variations of surface features like differential rotation on timescales of months and years.

3.1. Location

The observatory is located at the peak Izaña, close to the volcano Teide on Tenerife, Canary islands, Spain. The Teide observatory is located at 2400m altitude, 16°30'35" eastern longitude and 28°18'00" northern latitude, and hosts a number of other solar and stellar observatories like the German Vacuum-tower-telescope VTT and the new generation German solar telescope GREGOR. Fig. 3.1 shows a panoramic view of the Teide observatories with the STELLA building marked with a red arrow. Also visible are (from right to left) the GREGOR solar telescope, the ESA Optical Ground Station and the infrared telescope *Carlos Sánchez* in front of the distant peak of the Teide.

Figure 3.1.: A panoramic view of the Teide observatory. The STELLA observatory building is marked with a red arrow.

---

[1] STELLA is an acronym for Stellar Activity

[2] Mount Wilson Observatory

3.2. Building automation

3.2.1. Roll-off roofs

The observatory building is equipped with a roll-off roof. Fig. 3.2 shows the building during construction with both roofs in the open position. The roof is driven by Demag crane drives, with one motor and gear box per side per roof, thus four motors in total. The second roof starts moving with a short delay of about five seconds after the first one to minimize the starting current.

The roof is designed to be closed with the telescopes being in any arbitrary position. In case of bad weather or a technical failure, the roof closes in approximately 90 seconds. An UPS supplies power for at least 15 minutes to close the roof and to orderly shut down the telescopes and close the mirror covers. The roof electronics is controlled by a RS-485 relay module, and the roof status information like limit switches and motor failures are read by RS-485 digital input modules. The system is set up in such a way, that power failure of the control electronics, a failure of the RS-485 bus line, and failures of the control computers result in immediate closing of the roof (watchdog function).

In case the roof drive is broken or the electronics damaged, the roof has to be closed by hand. Since the gear boxes have a very high friction, electrical winches driven by automotive batteries (which are connected to a charger at all times) have to be used to force the roof shut. This has to be done by observatory staff on the site, since a cable has to be attached to the roof by hand for each of the two roofs.

Figure 3.2.: Outside view of the STELLA building in construction. The roofs are fully open, visible are the blocks at the end of the rails and the black energy chains used for power and signal cables to the moving roof.

3.2.2. Weather stations

The observatory hosts two weather stations, one at the top of each roof. Each weather station has temperature, humidity, rain, and wind speed sensors for increased reliability, while sensors for brightness, wind direction, and barometric pressure are available only once. The measured values are collected by RS-485 analog input modules and read out once per second. In addition to those physical sensors, logical ones can also be used. Examples that are implemented are the zenith distance of the Sun (depends only on time) and the dewpoint sensors (function of humidity and temperature). An advanced feature would be a weather forecast which could depend on many sensor readings and their trends (smoothed first derivatives).

In addition to the two outdoor weather stations, additional sensors are put inside the building. Temperature and humidity are available in the telescope bay, the spectrograph room and the electronics room, one additional pressure sensor is available in the spectrograph room, and temperature sensors are available on the spectrograph table and on one of the rails to probe for freezing conditions and possible ice. More sensors will be available to probe the telescope structure and mirror temperatures.

All weather sensors are recorded continuously to evaluate the current weather conditions. In order to avoid repeated opening and closing of the roof (“swinging”), the weather has to stay good for an extended period of time (e.g. for 15 minutes) before the weather status is considered good again. Five-minute average measurements are stored in a database for later retrieval of current observing conditions and to perform a more detailed analysis of the weather pattern.

3.2.3. Computers

The computers used for building automation and instrument control are off-the-shelf industrial computers. The main deviations from standard PCs are that we use VIA-C3 processors instead of Pentium/Celeron ones to be independent of a working CPU-cooling fan, and we use the watchdog capabilities of the computers to detect and solve lock-ups by rebooting. The basic operating system used is Debian/GNU Linux, which is installed on steady-state Compact-Flash (CF) cards. These CF-cards are plugged in directly on the mainboard and can be fairly easily exchanged. This makes a system upgrade which is tested on a physically different machine possible by merely replacing the CF-card, and those cards have no moving parts which makes them less prone to physical damage.

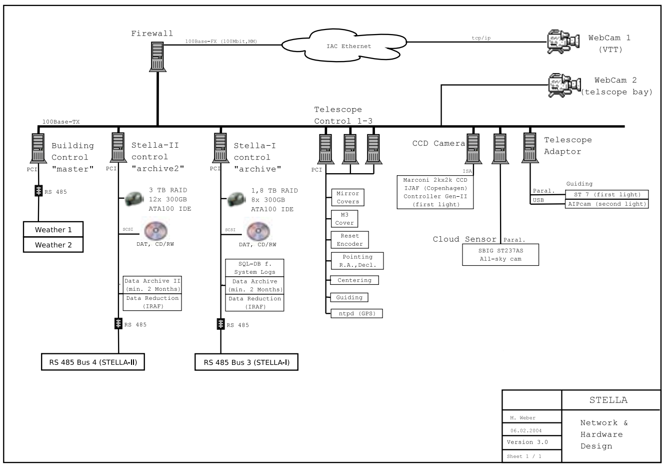

Figure 3.3.: Overview of the STELLA computer configuration. An attempt to use as few different parts as possible was done to minimize maintenance and stock-keeping efforts.

The STELLA computer network is connected directly to the IAC network switch, which is located in the residence building of the Izaña observatory. All network packets go through a firewall, which is made up of the same hardware as the control computers, but runs a special Linux-based firewall software (Linux Embedded Appliance Firewall). Only encrypted connections from the control center in Potsdam are allowed to the control computers. As a backup communication link a GSM-module is available. This allows slow speed Internet connection via the built in GSM-modem and the possibility of sending and receiving text messages (SMS) independent of a working Internet connection.

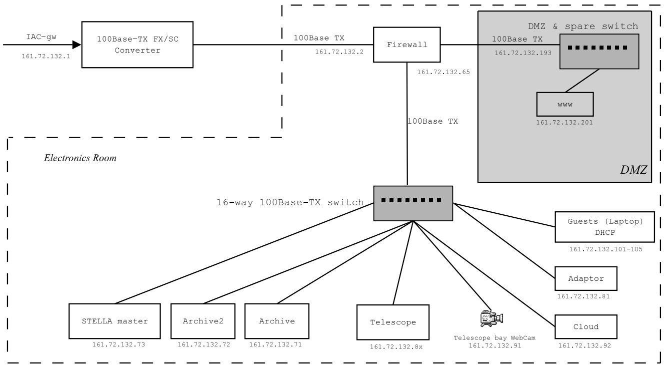

Figure 3.4.: Schematics of the STELLA computer network configuration. A firewall filters all traffic to the main computers except encrypted & trusted access from the control center in Potsdam.

All of the status data like log files, weather data, error messages are collected in a PostgreSQL database. This database is physically stored on the main data archive disks (*archive* in Fig. 3.3) and replicated to the data archive at the control center in Potsdam. The current data archive is made up of a RAID-5 system with six disks plus one spare disk plus one redundant disk, and has space for about 1.5 TBytes worth of scientific data.

The scientific data, which are basically all raw FITS files, also need to be transfered to Potsdam. But since this involves a very large data rate it can not be done in real time but has to be planned. The different scenarios are outlined in section 3.4.3

3.3. Instruments

The observatory will be equipped with two telescopes built by Halfmann Teleskoptechnik, Augsburg, Germany. For first light, one telescope with a diameter of 1.2m diameter, f-number 1/8, Alt/Az mount, Nasmyth focus and ø24' field of view will be available. It will be equipped with two instruments, one in each of the two Nasmyth foci: The STELLA échelle spectrograph (SES) and one wide field Stella imaging photometer (WIFSIP-I). A second version of the wide-field imaging camera will be mounted on the second telescope as its first light instrument. A detailed overview of the current status is given in Strassmeier (2004).

3.3.1. STELLA échelle spectrograph

The STELLA échelle spectrograph is a modern fiber-fed spectrograph based on the white-pupil design. It is optimized for optimum throughput at red wavelengths and is lacking any moving parts. The complete optical waveband from 390nm to 860nm is covered with a single exposure at a spectral resolution of 50 000 (see

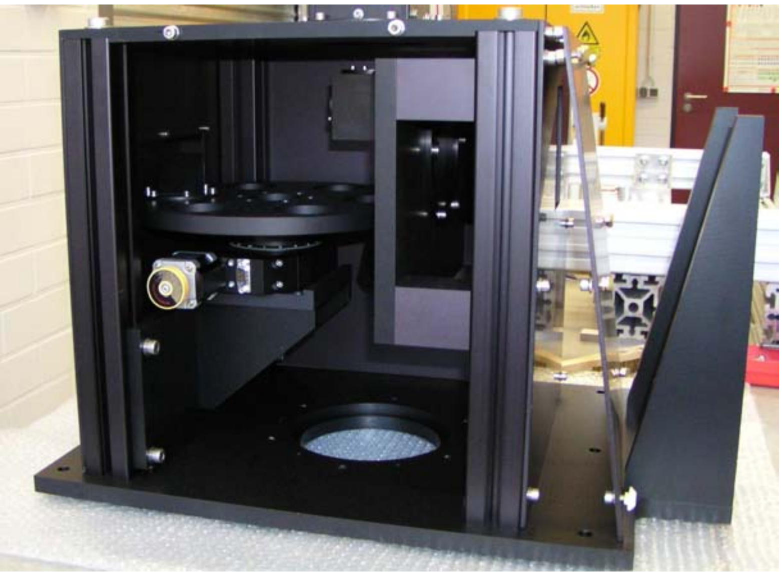

Figure 3.5.: The acquisition and guiding unit for the STELLA échelle spectrograph. The rotary stage is used to swivel in a flat mirror to feed calibration light into the fiber.

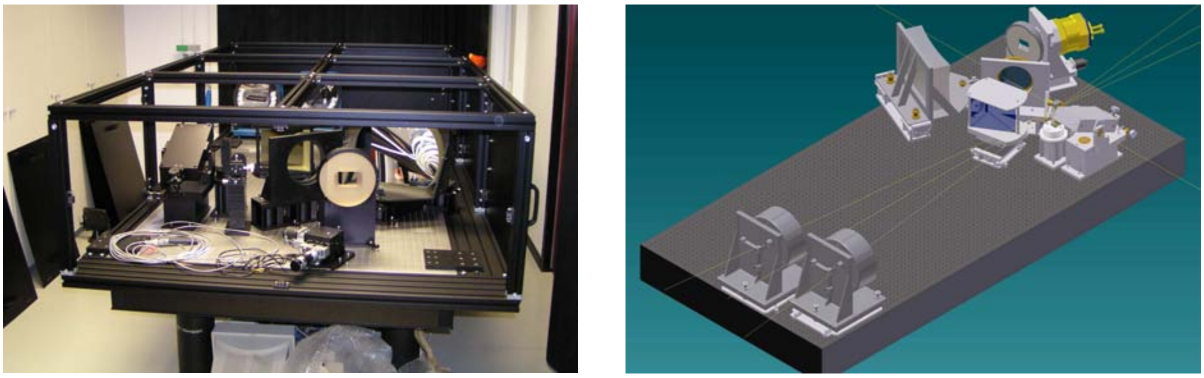

Figure 3.6.: The STELLA échelle spectrograph in the laboratory, seen from the camera side.

table 3.1). The light from the telescope enters the spectrograph through a 100μm optical fiber and a beam splitter that boosts the spectral resolution to the desired value. The main dispersion is done by a 31 lines per mm R2 grating from RGI, the cross-dispersion is handled by two prisms. The light beam is then picked up by a mirror and passes into the f/2.7 katadioptic camera with a 20cm corrector plate. The detector used in the camera is a 2048x2048 pixels, 13.5μm per pixel E2V 42-40 CCD, which is driven by a second generation Copenhagen University Observatory controller.

Since the original E2V CCD has slightly worse characteristics as specified, an otherwise identical replacement CCD was delivered by E2V, which will be driven by the more modern Magellan controller. This is built into a backup detector system, which will eventually replace the existing system once a second instrument is online. Again, the purpose of this is to keep the number of different parts as small as possible.

Table 3.1.: Central wavelengths and free spectral range of the SES

Order No.	free spectral range (nm)	λ_{central} (nm)	Order No.	free spectral range (nm)	λ_{central} (nm)
1	13.4062	871.40604	44	4.85608	524.45734
2	13.0030	858.20292	45	4.76739	519.64580
3	12.6178	845.39392	46	4.68110	514.92175
4	12.2494	832.96166	47	4.59714	510.28282
5	11.8969	820.88975	48	4.51541	505.72672
6	11.5594	809.16275	49	4.43585	501.25126
7	11.2361	797.76609	50	4.35837	496.85432
8	10.9261	786.68601	51	4.28290	492.53385
9	10.6288	775.90949	52	4.20937	488.28787
10	10.3435	765.42423	53	4.13773	484.11447
11	10.0695	755.21857	54	4.06789	480.01180
12	9.80633	745.28148	55	3.99981	475.97809
13	9.55327	735.60250	56	3.93343	472.01160
14	9.30989	726.17170	57	3.86868	468.11068
15	9.07569	716.97965	58	3.80552	464.27371
16	8.85021	708.01741	59	3.74389	460.49913
17	8.63304	699.27645	60	3.68375	456.78542
18	8.42376	690.74869	61	3.62504	453.13114
19	8.22200	682.42642	62	3.56773	449.53486
20	8.02740	674.30229	63	3.51177	445.99522
21	7.83963	666.36933	64	3.45711	442.51088
22	7.65838	658.62084	65	3.40372	439.08056
23	7.48333	651.05049	66	3.35156	435.70302
24	7.31422	643.65219	67	3.30058	432.37704
25	7.15078	636.42014	68	3.25076	429.10146
26	6.99276	629.34881	69	3.20206	425.87513
27	6.83992	622.43289	70	3.15445	422.69696
28	6.69203	615.66731	71	3.10789	419.56587
29	6.54889	609.04723	72	3.06235	416.48083
30	6.41029	602.56801	73	3.01781	413.44082
31	6.27605	596.22519	74	2.97423	410.44487
32	6.14598	590.01451	75	2.93159	407.49203
33	6.01991	583.93188	76	2.88986	404.58137
34	5.89768	577.97339	77	2.84902	401.71200
35	5.77914	572.13528	78	2.80903	398.88304
36	5.66413	566.41393	79	2.76988	396.09365
37	5.55253	560.80587	80	2.73154	393.34300
38	5.44419	555.30777	81	2.69400	390.63029
39	5.33899	549.91643	82	2.65722	387.95474
40	5.23681	544.62877	83	2.62119	385.31559
41	5.13754	539.44183	84	2.58589	382.71211

Table 3.1.: Central wavelengths and free spectral range of the SES (continued)

Order No.	free spectral range (nm)	λ_{central} (nm)	Order No.	free spectral range (nm)	λ_{central} (nm)
42	5.04106	534.35276	85	2.55129	380.14357
43	4.94727	529.35881	86	2.51739	377.60928

3.3.2. Wide field STELLA imaging photometer

The Wide field STELLA imaging photometer (WIFSIP) instrument will be available on the second focus on the STELLA-I telescope and on the first focus of the STELLA-II telescope. The first version will be specialized in narrow band filters: Strömgren uvby, Hα and Hβ narrow and wide, Bessel-Johnson UBVRI, and the Sloan filters will be available. It will allow for a usable field of view of 22'x22' at a scale of 0.32"/Pixel. The detector is a single 4096x4096 back-illuminated thinned CCD with 15μm Pixels and a peak QE$> 90\%$ from University of Arizona ITL.

The guiding on this instrument will be off center at the edge of the telescope's field of view. To make sure a guiding star is available for the chosen field, at least one specific guiding star has do be picked during target preparation using a graphical software tool. Here the target field and the derotator angle can be tuned to make sure a guide star exists in the guiding field. The guiding system is also equipped with a focus pyramid to make focusing (and controlled de-focusing) of the telescope easy, although we expect that the focus positions will be a constant function of temperature and altitude.

For time-series work, defocusing to approximately 3–5” is foreseen to obtain an accuracy of 1mmag in Strömgren v. The limiting magnitude will be around 19mag in V, while the guiding limit will be close to 17th magnitude.

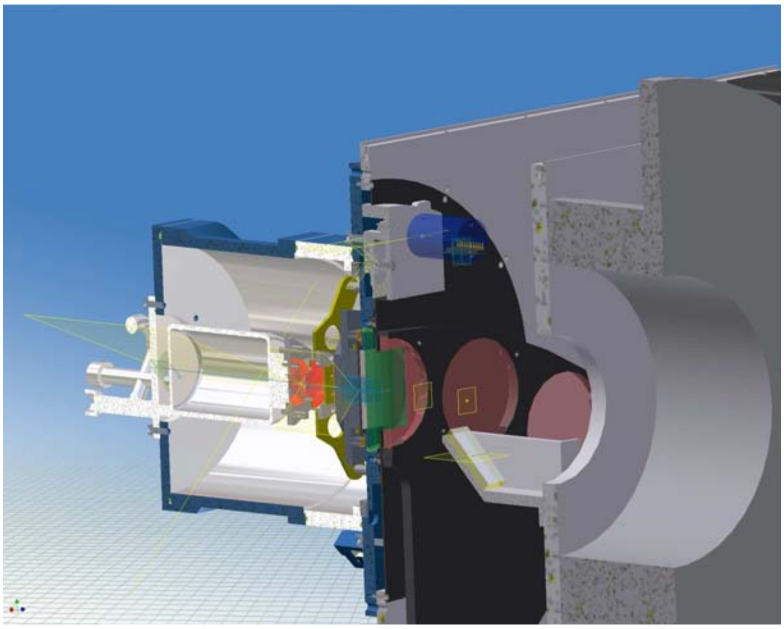

Figure 3.7.: The design for the wide field STELLA imager and photometer (WIFSIP).

3.4. Operations

All operations of the observatory are controlled from Potsdam. The robotic control software of the observatory has a pool of possible observations to choose from, and picks the observation with the highest merit at any given time (dispatch scheduling, see Granzer (2004)).

3.4.1. Target specification

The targets that are to be observed are described in a target definition file. The file format is xml, and a format definition is available to check if all necessary information is present and consistent. A unique identifier, a resolvable object name, the maximum exposure time, and the desired signal-to-noise ratio have to be specified as parameters. Additional to these, at least one scheduling parameter has to be supplied, and quality criteria like moon distance, seeing, airmass can be given.

Observations can be chained together, which is useful for observations that depend on each other. If not all chained observations meet the specified quality like seeing, signal/noise ratio, all members of the chain will be observed again. If submitting each of the observations individually, only the observations that fail will be repeated.

```
<!DOCTYPE Target SYSTEM "http://www.aip.de/stella/target.dtd">
<Target type="single" access="enabled">
  <TargetName>HD 97334</TargetName>
  <Email>
    <Address>obs-list@sro.aip.de</Address>
    <Notify>
      <Onfirstpick/>
      <Oncomplete/>
    </Notify>
  </Email>
  <Exception for="this">
    <Delay>DROP_TARGET</Delay>
    <Abort>TARGET_NOT_AVAILABLE</Abort>
    <Block>TARGET_AMBIGUOUS</Block>
  </Exception>
  <Select>
    <Requires>
      Roofopen &AND; GuidingAvailable &AND; Goodweather
    </Requires>
    <Constraint>
      <Variable>AltTarget</Variable>
      <Min>2.50000</Min>
    </Constraint>
    <Merit>
      <Timeslot class="stella.xml.OneObservationMerit">
        <Constant class="java.lang.Integer">
          <Constantname>maxobservations</Constantname>
          <Constantvalue>10</Constantvalue>
        </Constant>
      </Timeslot>
      <Gain class="stella.xml.WindowMerit">
      </Gain>
    </Merit>
  </Select>
</Target>
```

Figure 3.8.: An excerpt of a target definition description. The parts specifying the notifications, abort handling, and scheduling rules are shown.

3.4.2. Scheduling constraints

Scheduling constraints are mathematical formulas that are evaluated at the time a new object is selected. A merit function provided can be split up in several classes (Granzer 2004):

- Related to the target position: In this category fall all merits which depend on the positions on the sky, like airmass, moon avoidance, and slew-time.

- Based on previous observations: In this category fall the after-pick merit (which is useful for follow-up observations), time-out merit (basically the opposite of the previous case), number of observations (disables a target when it has been observed the requested number of times) and phase coherence (for phase critical observations like Doppler imaging targets).

- Time: This is for targets that should be observed at exactly one given time, or not before, or not after a specific time. See Fig. 3.9 for an example "not after" merit function.

- User fairness: This merit function makes sure that the telescope time is distributed evenly over all institutes and groups.

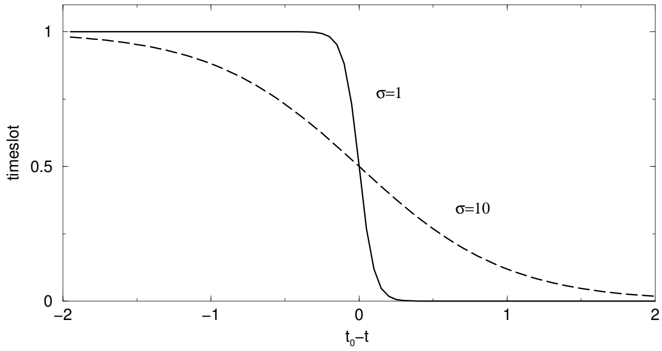

Figure 3.9.: Am merit function that terminates a target after a specified expiry date. The steepness of the inflection point can be adjusted (Granzer 2004).

The merit functions can be combined to achieve the desired result. This is illustrated in the case of a Doppler imaging target in Fig. 3.10. The basic function is a phase coherent merit which make sure that the observations are distributed evenly in rotational-phase space. This is combined with a merit-function that rises after the first observation is done to increase the chance each of the peaks of the underlying function leads to one observations. Finally the merit function drops to zero after (in this case three) a certain number of stellar rotations. If not all phases have been observed by that time, the observation is completed unsuccessfully.

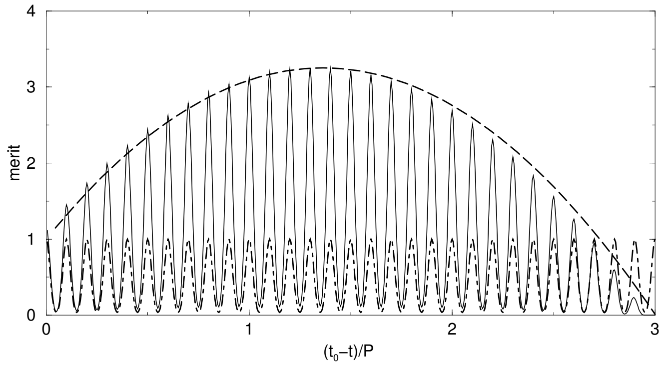

Figure 3.10.: The merit function for a Doppler imaging target. A phase-coherent merit function is combined with a merit that rises after the first observation (Granzer 2004).

3.4.3. Data size & transfer

Data product sizes

The SES is equipped with a 2x2k CCD operated by the Copenhagen Generation-II controller. The digitized data have a 16bit Integer format, therefore each raw image is exactly 8 MByte in size. The metadata that are contained in the image file (FITS header) can be estimated to have at most 25 kByte in the case of 100 header entries, and can thus be neglected here. Using lossless compression (White & Percival 1994; Sabbey 1999), the size of the raw images can be cut approximately in half, thus the average size of one raw image frame is 4 MByte.

If part of the data reduction process is done on site, namely the extraction of the echelle-orders, a considerable decrease in image size can be obtained. The number of echelle-orders is 86, thus the size of the reduced image is $86 \times 2048 \times 4$ ≈700kByte uncompressed. Even for a compression ratio significantly smaller than 2 for floating point data this amounts to less than 10% of the raw data.

The WIFSIPs (two are planned, one for each of the two STELLA telescopes) are equipped with a 4kx4k CCD. As above, the data size is a 16bit integer per pixel, which amounts to a raw image size of 32 MByte. The amount of metadata contained in these images will be of similar size than for the smaller SES-CCD, thus it has even less weight in this case. Assuming a similar average lossless compression rate as for the spectroscopic data, the final average image size is 16 MByte. The actual compression rate varies a lot, mainly due to different levels of sky background, but tests have shown that an average compression rate of two can be obtained.

Fully or partly reduced images from this instrument would generally not create smaller intermediate data products, with the exception of photometric data. A partially reduced image consisting of 32 bit floating point pixels is of course double size uncompressed, but up to three times as big after compression, since compression is much less effective on floating point data.

Data rate & bandwidth

The bandwidth of the Internet line from Potsdam to the STELLA observatory was measured in April 2004 (see Fig. 3.11). It is usually above 50 kBytes per second, with a peak of close to 200 kBytes per second. The bottleneck of the line is the connection from the IAC headquarters in La Laguna to the observatory at Izaña. The bandwidth of that line is 2 Mbit per second, which corresponds to the observed transfer rate of ≈200 kBytes per second.

To estimate the needed bandwidth we assume 100 images per night from the SES and 300 WIFSIP images per night. Both represent sustained averages, thus bad weather or nights with longer (and therefore less) observations can compensate for nights with many short exposures. Also, it is not clear when both telescopes will be available to simultaneously operate both instruments at the same time. Since an upgrade of the current 2 Mbit line to 10 Mbit is being proposed, the bandwidth problem may get smaller soon.

100 SES images make up 400 Mbyte per night, 300 WIFSIP images add up to 4800 Mbyte. To transfer these data amount during a 24 h time-span, bandwidths

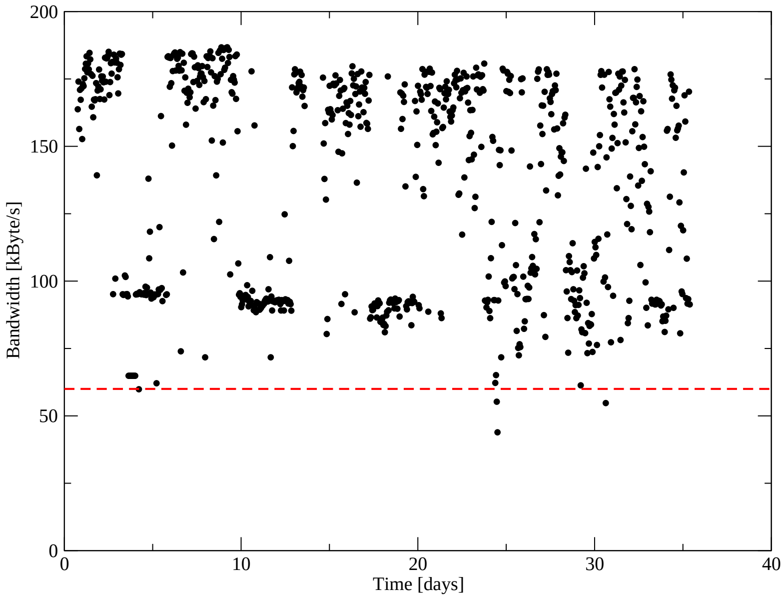

Figure 3.11.: Measurements of the bandwidth in April 2004 from the STELLA observatory to the robotic control center in Potsdam.

of approximately 5 and 55 kBytes per second are needed. This appears to be possible with the available infrastructure, but the data can not be transfered in real time. Therefore to allow for time critical observations a priority scheme for data transfer is needed. To save bandwidth, reduced data should not be transfered if not absolutely necessary. In case both WIFSIP instruments operate during a large fraction of the time, the cumulative data rate rises to 110 kBytes (if no spectroscopic observations are carried out).

In case the data rates needed are not achievable, data transfer using magnetic tapes is foreseen. All data will be archived on magnetic tapes, and a second copy will be prepared for data transfer. In this case real-time transfer of lossy-compression images is necessary to allow for quality assessment of the data. These images are then replaced by the lossless images transfered by air mail when they have arrived.

3.4.4. Data reduction

Spectroscopic data

The data from the SES is reduced by a data reduction pipeline based on IRAF. Since the spectrograph is of fixed format, the positions of the apertures have to be defined only once. Since no SES data are available yet, the pipeline has been tested on VLT/UVES data.

Data reduction includes bad pixel correction, bias subtraction, scattered-light subtraction, cosmic-ray correction, flatfielding, optimal aperture extraction, emission-line identification in the reference images, and wavelength calibration. Automatic normalizing of the spectra is not yet implemented and has to be done by hand, the same holds true for radial velocity measurements and telluric line subtraction. A more in depth description of the data reduction pipeline is available at the STELLA homepage.

In case the bandwidth is not sufficient to transfer the raw images from the spectrograph (see section 3.4.3), automatic data reduction can take place on site in Tenerife. Otherwise only raw images will be transfered to lighten the load of the line as much as possible.

Imaging data

This data pipeline is currently in the design phase. It is planned to use the EIS/MVM (Vandame 2002; da Costa 2004) software for as many reduction steps as possible. For photometry either MOMF (Kjeldsen & Frandsen 1992) or doPHOT (Schechter et al. 1993) will be used, but detailed tests have to be done to decide between those two or possibly other software packages are chosen. Detailed documents will be also published at the STELLA homepage when available.

Data post procession

The possibility to do automated analysis of the reduced data will be implemented. Every time new reduced data are available, a post procession script can be called. Examples for the spectroscopic data are abundance analysis and rotational velocity measurements using pre-calculated grids of model spectra as described in Allende Prieto (2004). For previously observed Doppler imaging targets, a first-order Doppler image can be computed once the requested observation set is successfully completed. In the case of imaging data, photometric magnitudes can be extracted and added to a variability database.

3.4.5. STELLA, a Doppler imaging machine

Of course the time spent on Doppler imaging targets will only cover a small fraction of the STELLA observing time. Not only because it is a shared instrument and most users have other interests, but also because scheduling Doppler imaging observations puts many restrictions onto the other observations. If too many programs try to restrict each other the results will not be as expected. The scheduler decides on what target to pick next in real time, no optimization is done beforehand. This should work well if only a few restrictive programs (say at most 30%) swim in a pool of not time-critical observations.

As described in the next chapter, reliable high-quality observations are needed for Doppler imaging. This will be the main advantage of STELLA over other instruments. As a dedicated instrument, data quality will be monitored constantly and many possible sources of problems like liquid nitrogen cooling, wavelength setup, and spectrograph camera focus are eliminated due to design decisions.

STELLA will obtain spectroscopic observations of constant quality whenever the conditions allow. During conventional observing runs, phase gaps can sometimes not be filled, because a different observer and/or instrument is scheduled at that telescope exactly when the missing phases are observable again. Avoiding this should drastically decrease the amount of “wasted” telescope time. But it also means that the requirements have to be specified in more detail before observations start. During a conventional observing run one tries to fill the time that is granted, while in the case of STELLA an observation block for Doppler imaging is aborted if the requested phase coverage is unreachable in the (also specified) amount of time left. This opens many niches for programs with non time-critical observations, that would be too small or too long-term for a traditional semester based time allocation committee.

4. Differential rotation on long period stars

This chapter demonstrates how to obtain reliable differential rotation measurements for stars with long rotational periods. The data used here originates mostly from one more than two months long observing run dedicated to Doppler imaging. Some additional data for the same stars from shorter observing runs at different observatories is added where available.

The first section describes the observations, subsequent sections deal with one star. Then two more stars are presented which have been published before, but additional work has been done concerning differential rotation. Finally, the results are summarized and compared to other differential-rotation measurements using Doppler imaging.

4.1. Observations

4.1.1. Spectroscopic Observations

Figure 4.1.: **Left.** The McMath–Pierce telescope at Kitt Peak, Arizona, where most of the observations were done. In the background the NSO vacuum telescope, which now hosts the SOLIS instrument. **Right.** Lightpath in the tunnel of the McMath–Pierce telescope. The star- (or sun-) light is reflected by the ceolostat (mirror 1) at the top of the building into the tunnel. At the bottom of the tunnel (buried into the ground) the light is reflected back up to mirror 3 (the one shown in the picture), which can be adjusted to reflect the light to the appropriate instrument. Images courtesy of NOAO/AURA/NSF.

Most of the spectroscopic observations presented here were obtained at the National Solar Observatory (NSO) with the McMath–Pierce telescope from October 31, 1996 to January 8, 1997. The stellar spectrograph together with the 800×800-pixel TI CCD (TI-4 chip, 15μ pixels) allowed for a resolution of $\approx$40,000 and a useful wavelength range of about 45 Å around 6430 Å. The mean FWHM of th-ar spectra taken each night was between 1.7 and 2.2 pixels, corresponding to a spectral resolution of 30 000 to 40 000. Fig. 4.3 shows the cross section of an example object spectrum (300 sec. exposure of HK Lac from November 21, 1996). The frame corresponds to the wavelength region 6395–6480Å, and the vignetting of the field lens and the rows of bad pixels are marked. We adjusted the center wavelength to make sure the main mapping lines Fe I 6430 and Ca I 6439 are between the bad pixels at columns 277 and 484. Unfortunately, this moved all other mapping lines except Fe I 6421 and sometimes Fe I 6411 (depending on the radial velocity of the target: it is usable in HK Lac as shown in the example image above, but not for e. g. HD 218153) off the usable range of the chip. Thus the usable wavelength region of our images is reduced from 85Å to 45Å.

Figure 4.2.: The KPNO 2.1m telescope (left) with the ceolostat with its little garage (center) and the coudé feed tower (right). The starlight goes from the ceolostat (mirror 1) to the tower (mirror 2) into the observing room, where mirror 3 reflects it into the coudé spectrograph. Image courtesy of NOAO/AURA/NSF.

Additional observations spanning one rotation of the stars HK Lac and IL Hya were taken by Washuettl (1998) in Dec. 1997/Jan. 1998 with the coudé feed telescope at Kitt Peak National Observatory (KPNO). A very similar 800×800 TI CCD (TI-5 chip, 15μ pixels) was used in combination with grating A, camera 5, and the long collimator, resulting in a resolving power of 38,000 in the 6420Å-region. Two more spectra from HD 218153 and single spectra from HD 208472 and HK Lac in the 6500-Å region included Hα and were obtained with the same instrumental set-up at the coudé feed telescope in April 1998 but utilized the 3096×1024 CCD (F3KB chip, 15μ pixels). The resolving power was 28,000, and the useful wavelength range was 300 Å. Exactly the same setup was used for the acquisition of two additional datasets of IL Hya spanning one stellar rotation each and taken one rotation apart in March/April/May 2000.

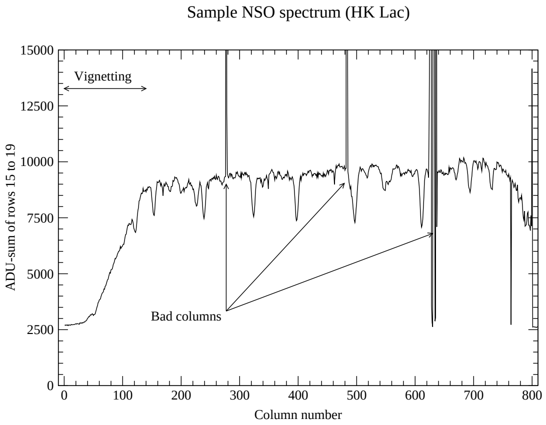

Figure 4.3.: Example of a spectrum taken at NSO/McMath. The TI-4 CCD has 800 pixels in dispersion direction, but vignetting cuts off approximately 150 pixels on the left (blue) edge, and a series of bad columns make the space above 600 pixels basically unusable. Two additional bad columns in the middle of the remaining space made careful centering of the two mapping lines necessary.

All data were reduced using IRAF[1], which included bias subtraction, flat field-

---

[1] Image Reduction and Analysis Facility distributed by NOAO/KPNO.)

ing, cosmic-ray removal, and an optimal aperture extraction. Usually twenty flat-field exposures with a Tungsten reference lamp were taken at the beginning of the night and again at the end of the night. These forty flat fields were co-added and used to remove the pixel-to-pixel variations in the stellar spectra. Spectra of bright radial-velocity standards were obtained several times throughout the night to ensure an accurate wavelength calibration. The following IAU velocity standard stars were used: α Ari (K2III, $v_{\rm r} = -14.3$ km s^{-1}), β Gem (K0III, $v_{\rm r} = 3.3$ km s^{-1}), and 16 Vir (K0.5III, $v_{\rm r} = 35.7$ km s^{-1}).

Data peculiarities

Besides the fact that only a fraction of the nominal wavelength range could be used due to the combination of vignetting effects and bad pixels (see fig. 4.3), several other effects had to be taken care of.

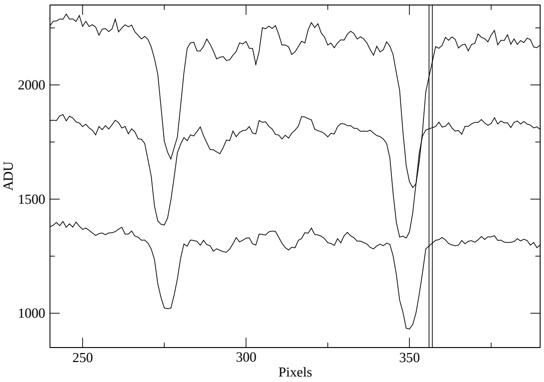

Figure 4.4.: Example spectra of HK Lac to illustrate the effect of two bad pixels affecting some of the data. The vertical lines mark the range covered by those two pixels. The effect of the interpolation can be easily seen, adding additional uncertainties to this data set.

- The dynamic range of the TI-4 CCD was very low. Nonlinearity started below 10 000 ADUs. This made it necessary to make several subexposures for high signal/noise observations.

- Depending on the position of the star in the sky, the position of the spectrum on the chip changed. We attempted to correct for this by using guiding offsets, but the position nevertheless changed by ±1 pixel.

- On days with bad seeing and/or high winds, the width of the star spectrum could slightly exceed the width of the corresponding flat field.

- Two pixels which are usually outside of the aperture were non-linear. In the HK Lac spectra the position of these two pixels often were within the Ca I 6439 line. Therefore a correction using interpolation was attempted in that case (see fig. 4.4). Unfortunately the spectral resolution and the pixel sampling are too low to effectively correct for this effect (also see section 4.6).

4.1.2. Photometric Observations

The photometric data in this paper were obtained with the Amadeus 0.75-m automatic photoelectric telescope (APT), part of the University of Vienna twin APT

Figure 4.5.: The Fairborn observatory; the telescopes Wolfgang and Amadeus are the middle ones of the four visible telescopes. The telescope in front is the TSU-T8 telescope, the one in the back the T5.

at Washington Camp (Strassmeier et al. 1997). Fairborn observatory is located in Southern Arizona close to the Mexican border town Nogales. It hosts a total of fourteen telescopes (as of Mid-2004), all of them operated robotically.

The telescope is equipped with Johnson/Cousins (Bessell 1979) $V(RI)_C$ filters, but usually only V and I_C are used here. The measurements are carried out differentially in respect to a comparision and a check star. The order of observations is as follows: N-CK-S-C-V-C-V-C-V-C-S-CK, where N is a bright navigation star, CK the check star, S the sky background, C the comparison star, and V the main target (variable star).

In order to obtain standardized magnitudes, a number of standard stars is observed every night. For Doppler imaging we use magnitudes relative to the comparison star. The standardized magnitudes of the comparison star in the different bandpasses were derived by averaging long term data, and that value was used to shift the relative magnitudes of the Doppler imaging targets for plotting purposes.

4.2. HD 208472

4.2.1. Introduction

Interest in HD 208472 (V2075 Cyg) was awakened after its strong Ca II H&K emission was detected in 1991. Very little was known about this star before. Henry et al. (1995b) discovered periodic light variability of HD 208472 (V2075 Cyg) with an amplitude of $0\overset{m}{.}36$. They measured a photometric period of 22.54±0.05 days and a projected rotational velocity $v \sin i$ of 21±2km s^{-1}. They also found the orbital period to be 22.6 days, determined the spectral type to be G8, and noticed large Hα-emission. A later photometric study by Strassmeier et al. (1999) showed a constant decrease in lightcurve amplitude to $0\overset{m}{.}12$ in late 1996 and $0\overset{m}{.}07$ in early 1997. The photometric period they found was 22.42±0.12 days. A detailed reanalysis of the orbital parameters was done by Fekel et al. (1999), who refined the orbital period to be $P_{\rm orb}$=22.62293.

4.2.2. Observations

All observations presented here are from the NSO 1996 observing run. The period of approximately 22 days allows for a coverage of three rotations of HD 209472, but due to bad weather at the end of the run the third data sub-set suffers from big gaps. It is still treated the same as the other two subsets, but one should keep this in mind when examining the results from that sub-set. The main details of the spectroscopic observations are listed in table 4.1. $P_{\rm orb}$=22.62293 and T_0=2449252.391 (Fekel et al. 1999) were used to calculate the orbital phases, the column *map* assigns the observation to one of the three blocks, which correspond to the three stellar rotations covered here. The distribution of spectroscopic observations over time are also shown graphically in figure 4.6. Photometric observations in Johnson V and Cousins I have been conducted with the University of Vienna twin APTs at Washington Camp (see section 4.1.2). A total number of 56 photometric datapoints have been observed simultaneous to the spectroscopic data, a detailed description thereof (including additional data taken up to June 1997) is given in Strassmeier et al. (1999).

Table 4.1.: Spectroscopic log and radial velocity data ($v_{\rm rad}$ of HD 208472).

HJD (24+)	Phase (°)	$v_{\rm rad}$ (km s^{-1})	$\sigma_{\rm rad}$	S/N	Rotational cycle	Telescope
50388.756	83.0	12.9	1.2	90	map 1	NSO
50390.612	112.6	3.0	1.8	30	-	NSO
50391.580	128.0	3.2	1.2	90	map 1	NSO
50392.574	143.8	-2.3	1.5	90	-	NSO
50393.571	159.7	-2.7	1.1	80	map 1	NSO
50394.571	175.6	-5.7	1.0	110	map 1	NSO
50395.657	192.9	-3.8	1.0	110	map 1	NSO
50396.589	207.7	-1.3	0.9	120	map 1	NSO
50398.574	239.3	-0.4	0.9	100	-	NSO

Table 4.1.: Spectroscopic log of HD 208472 (continued)

HJD (24+)	Phase (°)	$v_{\rm rad}$ (km s^{-1})	$\sigma_{\rm rad}$	S/N	Rotational cycle	Telescope
50399.577	255.2	5.9	1.1	120	map 1	NSO
50400.570	271.0	10.3	0.8	110	map 1	NSO
50401.570	287.0	15.1	0.8	110	map 1	NSO
50402.576	303.0	19.1	1.2	100	map 1	NSO
50404.571	334.7	21.4	1.0	120	map 1	NSO
50405.562	350.5	25.5	0.8	110	map 1	NSO
50406.566	6.4	25.7	1.1	120	map 1	NSO
50407.564	22.3	23.2	0.9	130	map 1	NSO
50408.579	38.5	27.6	1.1	130	map 1	NSO
50409.562	54.1	18.1	1.0	110	map 1	NSO
50410.587	70.4	17.2	1.1	110	map 1	NSO
50411.560	85.9	11.5	1.1	120	map 2	NSO
50412.557	101.8	5.8	1.1	120	map 2	NSO
50413.555	117.7	1.4	0.9	110	map 2	NSO
50414.558	133.6	-2.1	0.7	110	map 2	NSO
50415.556	149.5	-3.5	1.0	110	map 2	NSO
50416.568	165.6	-5.8	0.7	110	map 2	NSO
50417.583	181.8	-4.5	1.1	110	map 2	NSO
50418.595	197.9	-4.1	1.0	120	map 2	NSO
50419.547	213.0	-4.4	0.9	110	map 2	NSO
50421.558	245.0	3.6	1.2	110	map 2	NSO
50422.553	260.9	7.3	0.8	120	map 2	NSO
50423.569	277.0	12.9	1.1	110	map 2	NSO
50424.565	292.9	19.6	1.2	110	map 2	NSO
50425.554	308.6	20.5	1.2	120	map 2	NSO
50427.555	340.5	26.0	1.0	120	map 2	NSO
50429.554	12.3	26.1	0.9	110	map 2	NSO
50430.553	28.2	25.8	0.9	120	map 2	NSO
50431.545	43.9	21.6	0.8	130	map 2	NSO
50432.548	59.9	17.3	0.9	120	map 2	NSO
50434.549	91.8	9.0	1.1	110	map 3	NSO
50435.553	107.7	4.1	1.1	100	map 3	NSO
50436.582	124.1	2.2	1.1	120	map 3	NSO
50437.541	139.4	-1.1	1.8	90	-	NSO
50438.552	155.4	-5.5	1.0	110	map 3	NSO
50440.563	187.5	-4.4	0.9	70	map 3	NSO
50441.553	203.2	-5.0	1.3	100	map 3	NSO
50446.547	282.7	13.0	1.4	90	-	NSO
50447.554	298.7	16.0	0.9	100	map 3	NSO
50450.559	346.5	24.3	1.5	100	map 3	NSO
50451.555	2.4	25.7	1.3	90	map 3	NSO
50454.568	50.3	19.7	1.1	80	map 3	NSO
50457.564	98.0	7.4	0.9	100	map 3	NSO

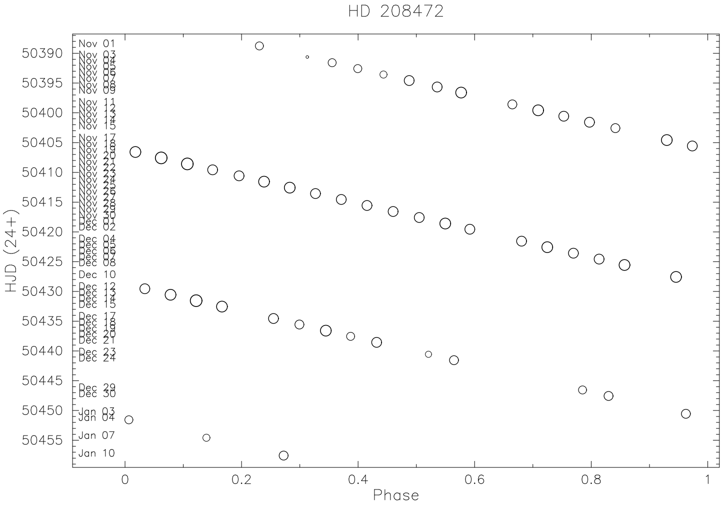

Figure 4.6.: Distribution of the rotational phases of HD 208472 versus date. The sizes of the circles are proportional to the S/N ratio of the spectra, where the average value is about 100:1.

Physical parameters

A collection of physical parameters of HD 208472 is listed in table 4.2. The orbital period has been very accurately determined by Fekel et al. (1999), the photometric period, which is almost the same as the orbital period which puts this star into the group of RS CVn systems, is taken from Strassmeier et al. (1999). The spectral type is taken from Henry et al. (1995b), the effective temperature is from Bell & Gustafsson (1989), distance from Hipparcos (ESA 1997), the radius is a derivative of $v \sin i$, $P_{\rm rot}$ and the stellar inclination angle, the latter being also the source for the high uncertainty. An initial guess of 20km s^{-1} for the projected rotational velocity ($v \sin i$) has been taken from Fekel (1997) and 45° was assumed for the inclination of the stellar rotation axis. The optimized values for these two parameters listed here are derived in the next section.

Fine tuning $v \sin i$ and inclination

Measuring the projected rotational velocity by cross-correlation with a template star usually leads to a slight underestimation of $v \sin i$ due to the unknown rotational velocity of the template star. Since Doppler imaging is very sensitive to wrong rotational velocities, one can find a more accurate value by variation of $v \sin i$ while keeping all other parameters constant. The $v \sin i$ value that produces the Doppler image with the smallest corresponding χ^2 is the most probable one (see figure 4.7).

The most direct method to determine the inclination of the stellar rotation axis is to calculate the minimum radius R$\sin i$ from $v \sin i$ and $P_{\rm rot}$ on the one hand, and to estimate the real radius from the spectral type on the other hand. This fails in the case of giant stars, since the radii for the respective spectral types are too uncertain. A more reliable procedure is to use the inclination-sensitivity of Doppler imaging to find a better estimate for the inclination angle. A test of this procedure on artificial data is described in appendix A The fine-tuning results for the inclination of HD 208472 is shown in figures 4.8.

Table 4.2.: Stellar parameters of HD 208472

Parameter	Value
Spectral type	G8 III
$\log g$	2.5 ± 0.5
$T_{\rm eff}$	4900 ± 100 K
V	7.49 mag
$(B-V)$	1.066 ± 0.009mag
$(V-I)$	1.03 ± 0.01 mag
$v \sin i$	22.0 ± 1.0 km s^{-1}
Inclination i	$35^\circ \pm 15^\circ$
Distance d	157 ± 18 pc
Radius R	17.1 ± 4.5 $R_\odot$
Orbital period $P_{\rm orb}$	22.62293 ± 0.00097 days
Rotation period $P_{\rm rot}$	22.42 ± 0.12 days
Equatorial velocity $v_{\rm equ}$	$32.3^{64.3}_{28.7}$ km s^{-1}
Microturbulence ξ	2.0 km s^{-1}
Macroturbulence $\zeta_{\rm R} = \zeta_{\rm T}$	4.0 km s^{-1}
$\log[Ca]$ abundance	0.9 dex below solar
$\log[Fe]$ abundance	0.9 dex below solar

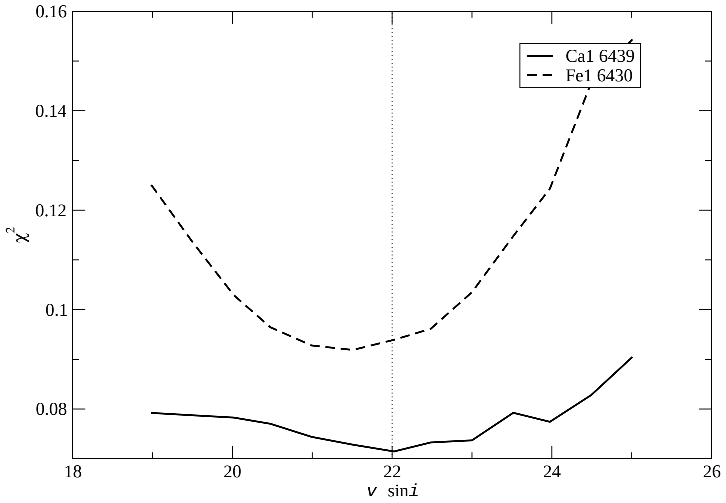

Figure 4.7.: Parameter variation to determine the most probable projected rotational velocity $v \sin i$. All spectra were combined and all other parameters were fixed. A value of 22km s^{-1}(as indicated by a vertical dashed line) was adopted.

4.2.3. Time-series Doppler imaging

As in almost all objects observed during the NSO 1996 run, only two spectral lines could be used. The other lines in the observed wavelength range where not usable due to vignetting and bad columns on the CCD chip. The two spectral lines are Fe I 6430 with a $\log gf$ value of -2.0 and Ca I 6439 with a $\log gf$ value of +0.47. A total of 52 spectra (see table 4.1) were taken, of which 5 were too noisy to be used for Doppler imaging. The data are spanning exactly three stellar rotations and is therefore divided into three subsets labeled *map 1*, *map 2* and *map 3* in table 4.1, respectively.

Using the physical parameters from table 4.2 we computed one Doppler image for each stellar rotation and spectral line, thus altogether six images. Fig.4.9 and 4.10 show the resulting Doppler images in two pseudo-projections, the line profile data and fits, and the photometric data points with the synthetic lightcurve from

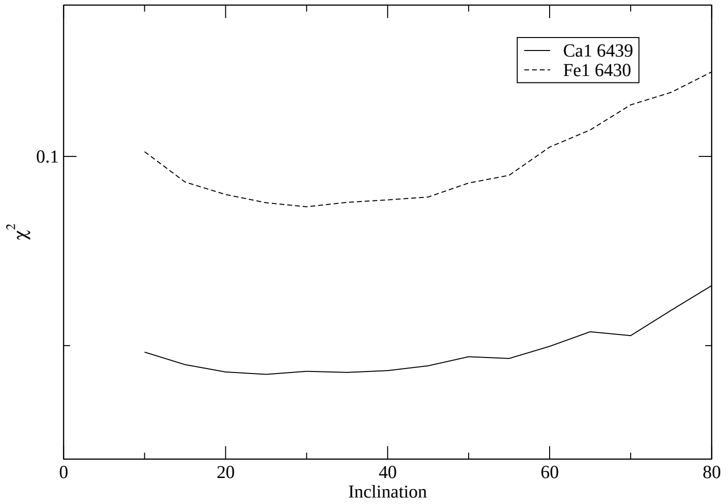

Figure 4.8.: Parameter variation to determine the most probably inclination value for HD 208472. All spectra were combined and all other parameters were fixed. Plotted is the resulting χ^2 for the two spectral line regions for inclination angles of 10° to 80°. An inclination angle of 35° was adopted.

the Doppler image. The maps from all three data blocks seem very similar. The third map has very scarce phase coverage at the end and is therefore based on far less phases than the other two maps (17 & 19 for the first two maps, 11 for the third). One has to also keep in mind, that the observations have a spectral resolution of approximately 0.19Å, which results in only 5 resolution elements across the stellar disk (or 70° per resolution element). Notable is the absence of spot features above 50°. Most of the recovered spot area is lined up along the sub-observer latitude (which corresponds to the inclination angle of 35°), with the exception of the feature at ℓ=210° which appears to be closer to the equator. The almost even distribution of spots along all longitudes is also the reason for the low lightcurve amplitude of $0\overset{\mathrm{m}}{.}12$, compared to $0\overset{\mathrm{m}}{.}36$ reported by Henry et al. (1995b). Obviously, the spots were concentrated much more at the time of their observations (end of 1993).

Cross-correlations

To determine the temporal variations of the stellar surface structure during the observed time range, the three images of each spectral region were cross correlated with each other. The result, three cross-correlation images for each of the two spectral lines, is shown in figure 4.11 and 4.12. The first image (figure 4.11a) is computed by cross-correlation of the first and the second map (see figure 4.9 and 4.9 for the input maps), the second (figure 4.11b) using the second and third, and the last one (figure 4.11c) using the first and last Doppler map. All figures show the respective cross-correlation map where darker colors mean a better agreement. Additionally a dotted line marks the rotation rate for a rigid rotator matching the orbital period. The solid line represents a rotation rate corresponding to an average differential rotation law derived later.

An examination of the individual cross-correlation images shows large differences between them. The difference between the cross-correlations representing different time-spans can easily be explained with spot reconfigurations, or more probable with the lower quality of the third data block. But the discrepancy between the two spectral-line regions can only be explained with the comparably low signal-noise ratio of the data (see Tab. 4.1 for a list of signal-noise ratios). Never-

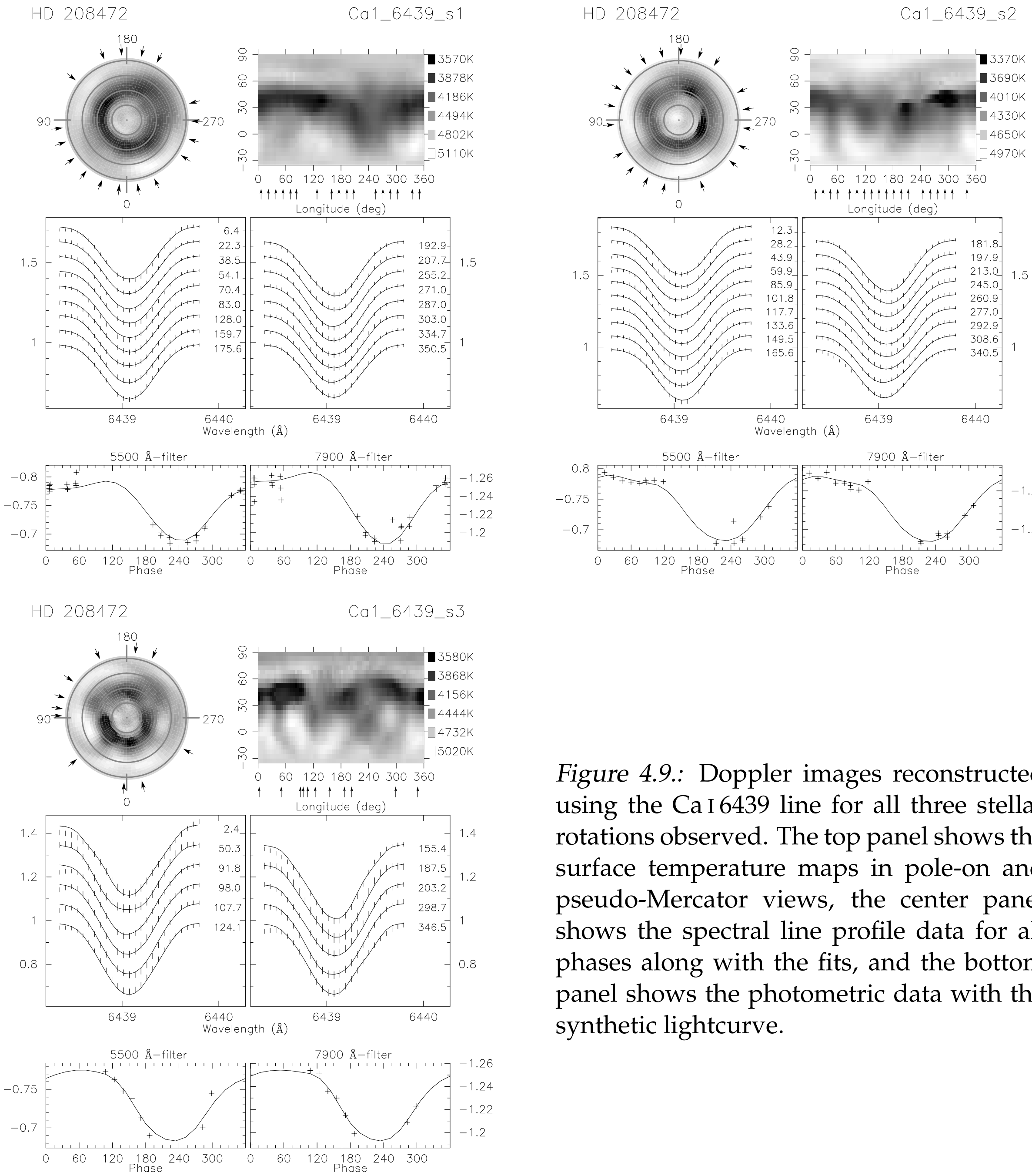

Figure 4.9.: Doppler images reconstructed using the Ca I 6439 line for all three stellar rotations observed. The top panel shows the surface temperature maps in pole-on and pseudo-Mercator views, the center panel shows the spectral line profile data for all phases along with the fits, and the bottom panel shows the photometric data with the synthetic lightcurve.

theless, the two cross-correlation images for the first and second block look very much alike. One has to keep in mind, that the spots are concentrated at a latitude of 35°, with the exception of one small feature at 25°. The dotted line corresponds to the orbital period. If the star would rotate rigidly with this period, a sharp vertical feature should be visible along this line. But this feature is only visible at ±20° north and south of the equator. Its width is compatible with the surface resolution expected from the spectral data (70° corresponds to about 3°/day in that cross-correlation image). The circular isolated features (at about 12°/day, 25° in the first map of figure 4.11) have a distance to the center that corresponds to the expected surface resolution. This makes them probable aliases which come from

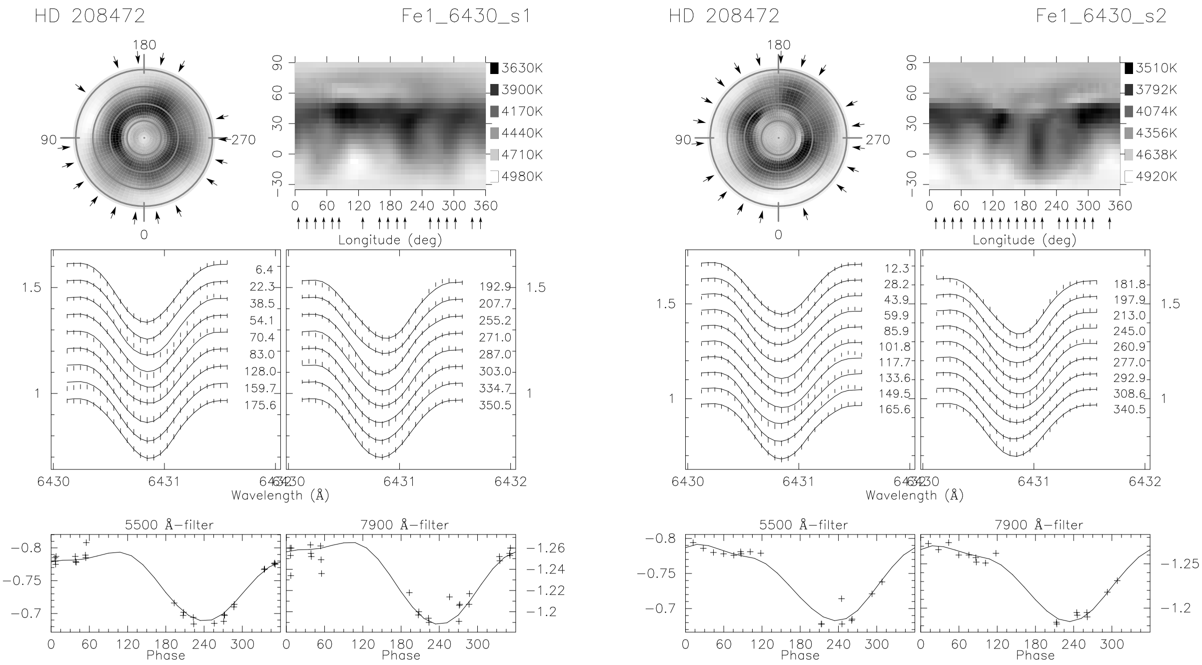

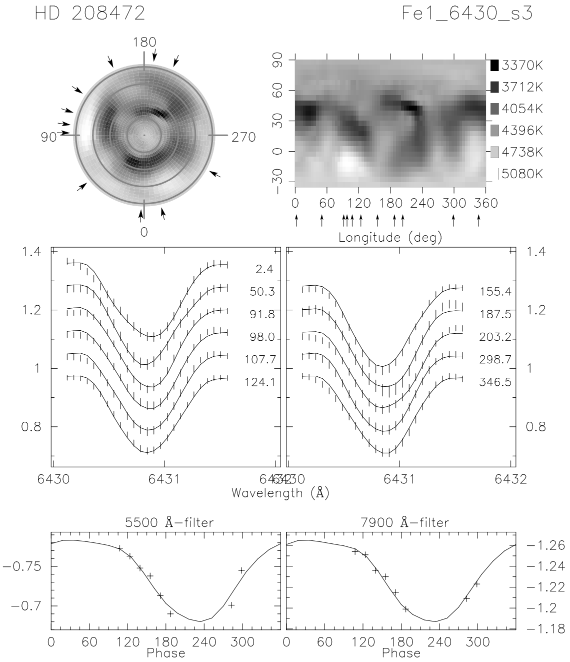

Figure 4.10.: As in Fig. 4.9 but for the Fe I 6430 line.

latitudinal elongations of spots due to the higher uncertainties in longitudinal spot positions. The solid line shown in all cross-correlation maps in figures 4.11 and 4.12 correspond to a probable differential rotation function derived further down in this section. Not only because of the poor match of this line, all these cross-correlation images appear to be noise dominated. Another possible explanation, that the spot distribution changes on timescales smaller than the rotation period thus rendering the cross-correlation technique useless, is improbable due to the stability of the lightcurve shape over several rotation periods.

To enhance the differential-rotation signal in the cross-correlation images, the data set was divided into 23 subsections, each spanning 23 days (approximately

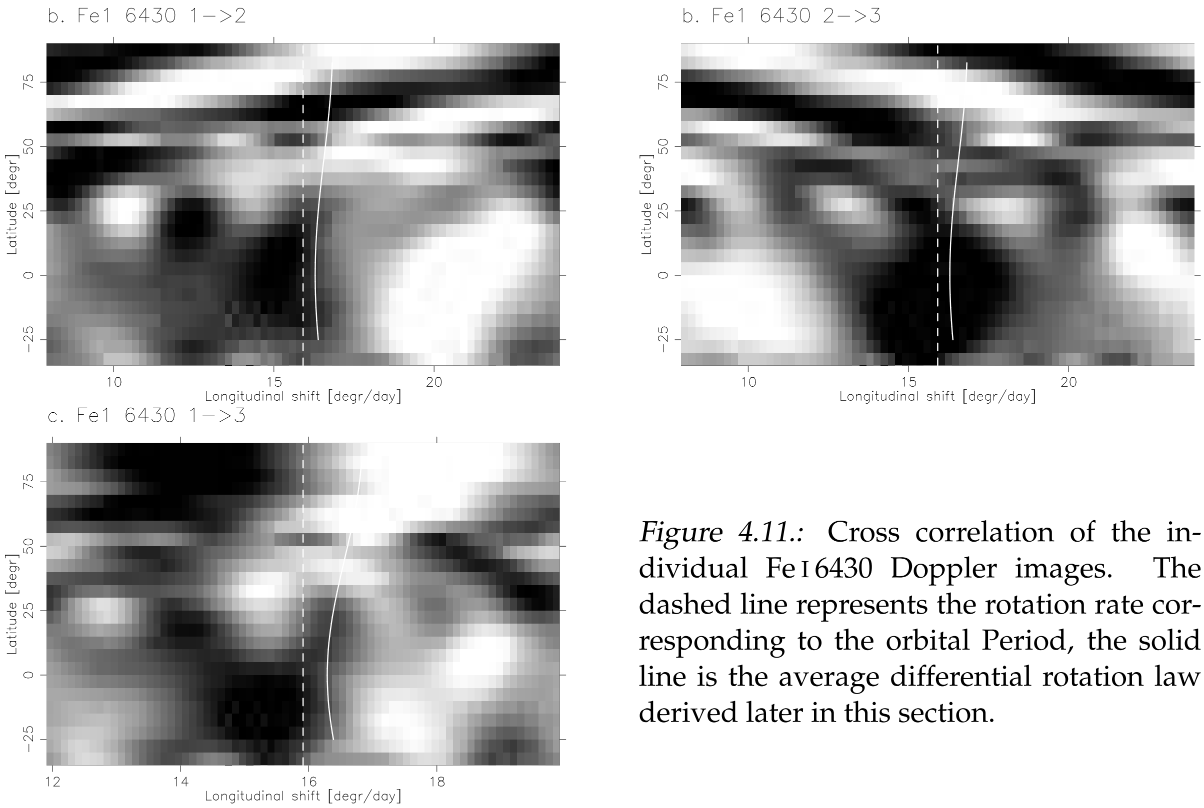

Figure 4.11.: Cross correlation of the individual Fe I 6430 Doppler images. The dashed line represents the rotation rate corresponding to the orbital Period, the solid line is the average differential rotation law derived later in this section.

the rotation period) but with a incrementally increased starting date. From these 23 images, 18 cross-correlation images were produced. The mean time difference between two cross-correlated images is about half of the rotation period. All these cross-correlation images were then corrected for variations in time-difference (see also Kővári et al. (2004)). The resulting images were averaged with three different high & low rejection values, namely 0 (all images were averaged), 15% (the three highest and lowest values were rejected), and 30% (the five highest and lowest values were rejected). All further analysis is done on all three versions of the average cross-correlation image. This allows a rough error estimate by calculating average and standard deviation values.

To determine the differential rotation value, Gaussian profiles have been fit to the peaks in the average cross-correlation image for each latitude. A solar-like differential rotation law was then derived, restricting the values for latitudes from $-15°$ to $55°$ since the features on the Doppler images are concentrated in that area. The resulting parameters Ω_0 ($= 360/P_{\mathrm{equ}}$), Ω_1, and α ($= \Omega_1/\Omega_0$) are listed in table 4.3. The error values listed are three standard deviations from the three different methods computing the average maps.

The resulting cross-correlation images are shown in figure 4.13. The solid line shown in all three images is the fit of the data measured off the average cross correlation map (row *average* in table 4.3).

Differential rotation measurement using TEMPMAP

As shown in appendix A.2, differential rotation can also be detected using the TEMPMAP code directly. A static parameter is introduced to allow latitude de-

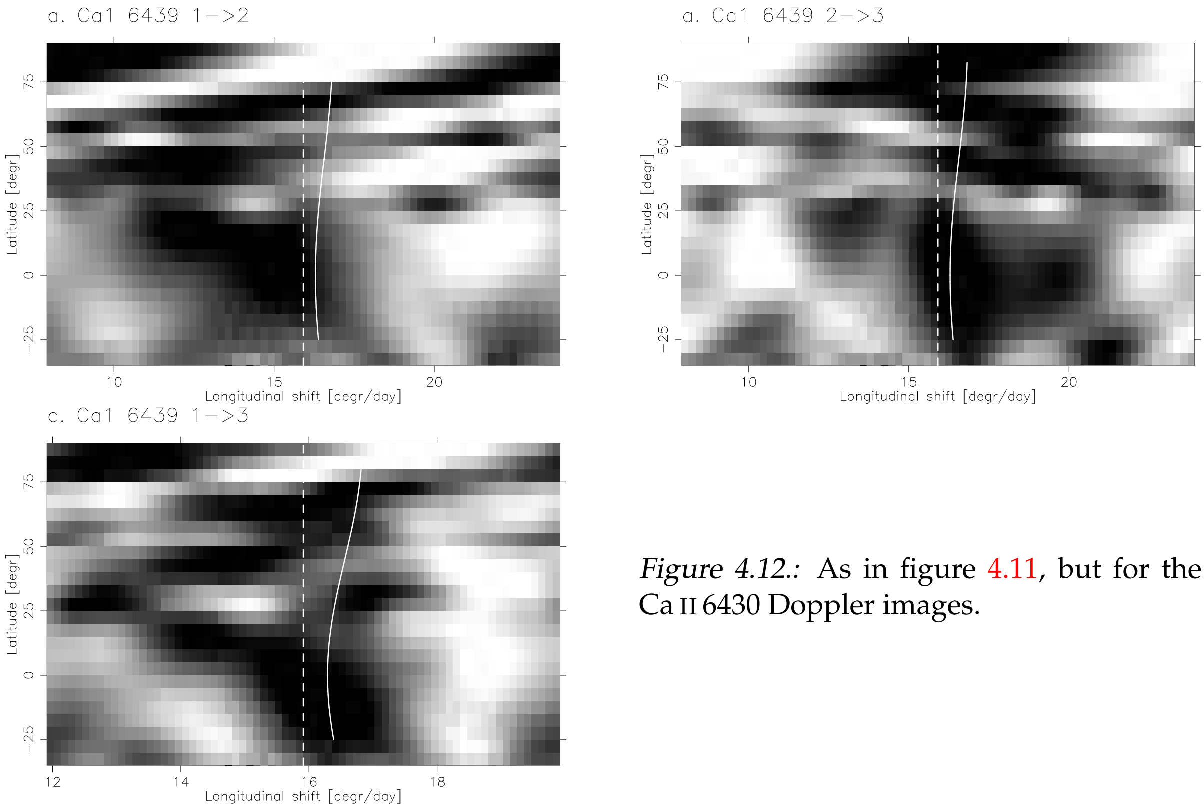

Figure 4.12.: As in figure 4.11, but for the Ca II 6430 Doppler images.

pendent rotational velocity. This parameter along with the rotation period (which represents the equatorial rotation rate now) can be varied. The goodness of the fits to the data is plotted in a 2-D diagram in respect to the equatorial rotation rate and the differential rotation parameter α (which denotes the strength and direction of the differential rotation).

Unfortunately, the quality of the spectra used here is not quite sufficient do do a reliable analysis. As shown in figure A.8 the differential-rotation signal of a star with $\alpha \approx$0.1 (half of the solar rate) is in average about 1% of the line profile signal. For spectra with a signal-noise ratio of slightly above 100 (as the data used here) the amplitude of the noise is comparable to the differential-rotation signal.

The analysis was nevertheless done since an estimate of the magnitude of the differential rotation from the previous section can be used as a starting point. The data spanning all three stellar rotations was combined to increase the information content. The downside of combining all data is that it is probable that significant spot reconfigurations take place during that times pan. Figure 4.14 shows the resulting χ^2 map for both spectral regions: The Fe I 6430 map shows a smooth slope towards higher α with a rather shallow minimum at α=0.1–0.2, while the Ca I 6439 map shows a remarkably pronounced minimum at α=−0.04. The latter value being in agreement with the cross-correlation analysis which suggests a small negative α parameter (meaning the rotation at the pole is a few percent faster than at the equator).

To investigate the region around the suspected α/period region closer, figure 4.15 shows the χ^2 distribution for a constant value for the rotation period of 22.6 days. The slope of the Fe I 6430 can be easily seen, which suggests that a systematic mis-

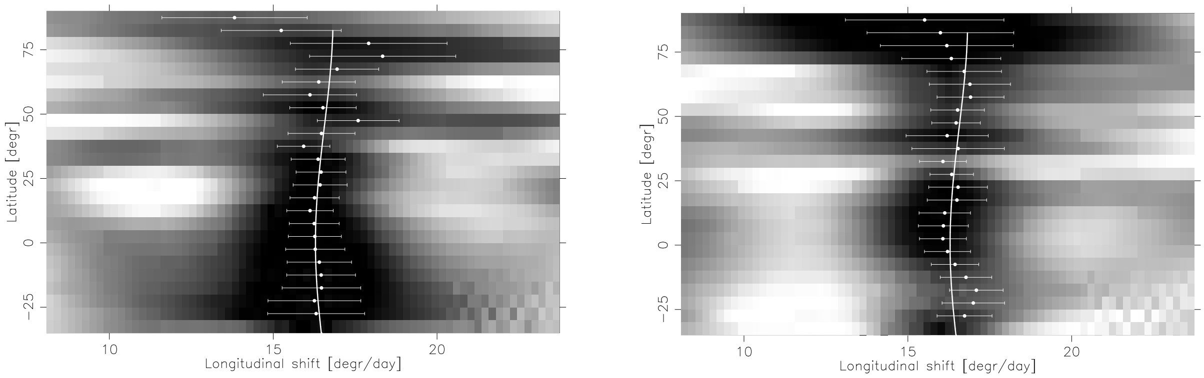
a. Fe I 6430

b.,Ca I 6439

c. Average

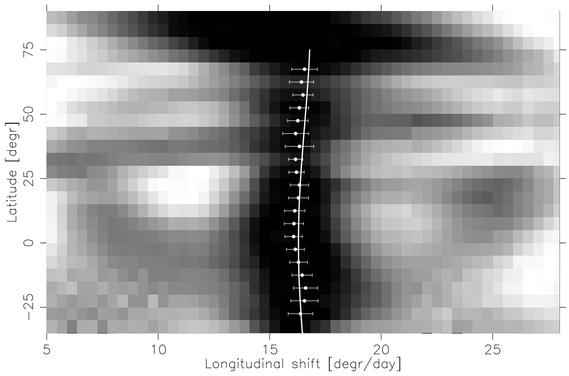

Figure 4.13.: Average cross correlations for Fe I 6430 (a), Ca I 6439 (b), and all of them (c). The dots are measured positions using a Gaussian fit, the error estimates come from the FWHM of the Gaussians. The solid line represents the differential rotation value from table 4.3, which is a fit to the data shown (c). Each map is an average of 18 different cross-correlation maps (36 in total for panel c), during averaging the 15% highest and lowest values for each pixel have been discarded.

fit of the line profiles is being compensated with a more pointed line profile (which corresponds to a positive differential rotation coefficient). This shows that the model parameters are less accurate for the Fe I 6430 line, which is also reflected in the higher χ^2 values of that line.

Summary

Table 4.3.: Differential rotation derived from cross-correlation and from the sheared-image method. The values for each spectral line an average from three images with 0, 15%, and 30% high/low rejection value.

	Ω_0	Ω_1	α
Ca I 6439	16.30±0.03	0.33±0.3	−0.02±0.02
Fe I 6430	16.28±0.12	0.74±0.3	−0.05±0.02
Sheared image	16.07±0.14	0.64±0.32	−0.04±0.02
Average	16.29±0.08	0.54±0.72	−0.03±0.04

As seen in many active binary systems, the photometric period is close to the orbital period, but not exactly the same. Since the photometric period reflects the rotation rate at the spot latitude, variations in the photometric periods can be viewed as changing spot latitudes (due to either newly forming or moving spots) combined with differential rotation. If one assumes that the stellar equator is really in synchronization, one can estimate the sign and the magnitude of the

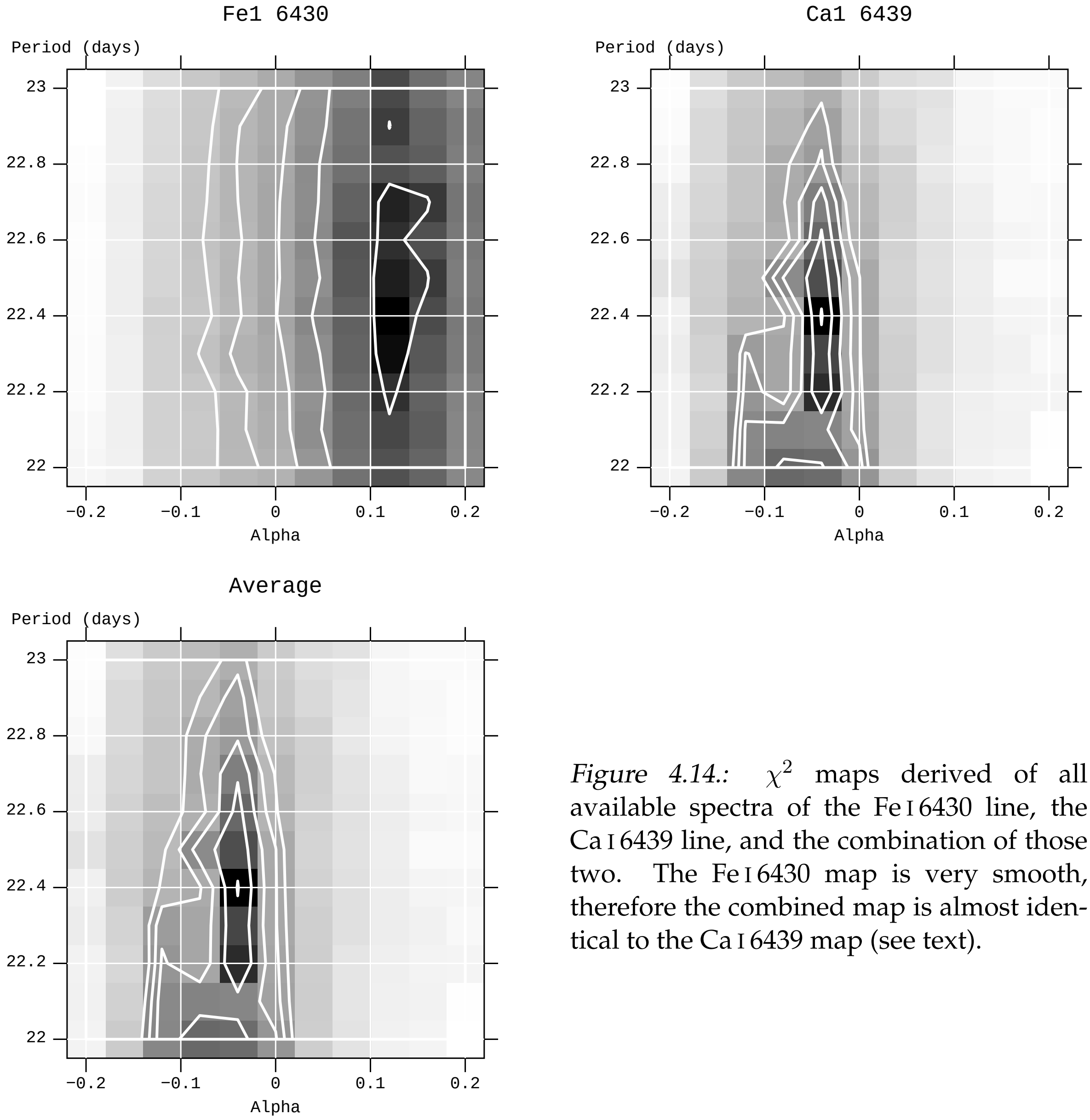

Figure 4.14.: χ^2 maps derived of all available spectra of the Fe I 6430 line, the Ca I 6439 line, and the combination of those two. The Fe I 6430 map is very smooth, therefore the combined map is almost identical to the Ca I 6439 map (see text).

differential rotation. In this case,

$$\alpha = \frac{P_{\text{phot}} - P_{\text{orb}}}{P_{\text{phot}}} \times 3 = -0.027. \tag{4.1}$$

The numerical factor corrects the results for the main spot longitude, in this case 35° was used. This is only a rough estimate since it is based on the assumption that the equator rotates with the orbital rotation period. A better method for the determination is the “sheared image” method described in section 4.2.3. There we find an anti-solar differential rotation with a differential rotation parameter α=-0.04 ± 0.02 and an equatorial rotation period of 22.4 days. Unfortunately, the second spectral line, which has higher uncertainties and a smaller equivalent with, does not confirm the result.

The other method applicable here, because of the coverage of at least two succes-

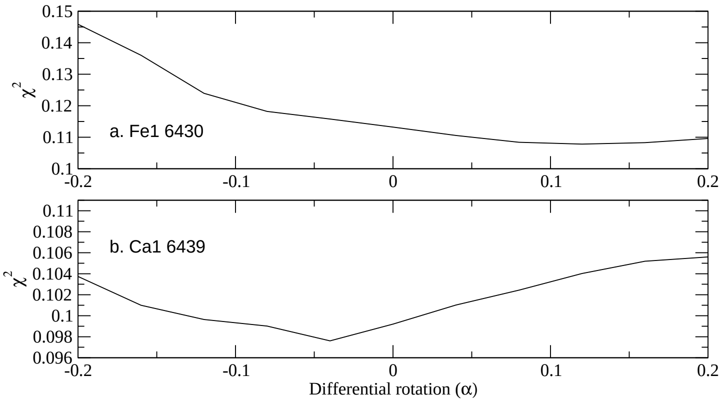

Figure 4.15.: A cut through figure 4.14 for an equatorial rotation period of 22.6 days. The Fe I 6430 line displays a very shallow minimum (**a**), while the Ca I 6439 line exhibits a pronounced minimum at $\alpha \approx -0.04$.

sive stellar rotations, is the cross-correlation technique. As shown in section 4.2.3, simple cross correlations of two successive maps did not show any systematic changes either. But when many cross-correlation images were computed from subdividing the data set into as many one rotation period long sub-blocks as possible, the average image of those does reveal some systematic changes, but the uncertainties are higher than the detected differential rotation. The results are summarized in table 4.3, and even though the value found for the differential rotation parameter is consistent with the values derived above, it is formally not significant and needs to be confirmed, preferably with data of better signal-to-noise ratio and higher spectral resolution.

4.3. IM Peg

4.3.1. Introduction

IM Peg (= HD 216489 = HR 8703 = HIP 112997) has been long known to be a spectroscopic binary star (Harper 1920), and is one of the best studied RS CVn systems (Hall 1976). Recently, the orbit has been re-determined by Fekel et al. (1999) and Berdyugina et al. (1999b). The latter performed a detailed spectrum synthesis and parameter determination, most of which are listed in table 4.5. First Doppler images for IM Peg have been obtained by Berdyugina et al. (2000), who found re-distribution of spot surface between two active longitudes and suspected a cyclic behavior with a period of 6.5 years.

The photometric history of IM Peg is as well studied as the spectroscopic one. The long-term photometric period has been found by Strassmeier et al. (1999) to be 24.45 days, while the lightcurve amplitude decreased from $0^{\mathrm{m}}.4$ in 1996 (the time the data presented here was observed) to $0^{\mathrm{m}}.22$ by mid 1997. A more detailed study of the lightcurve behavior has been conducted by Ribarik et al. (2003). They find two possible cycle periods (29.8 and 10.4 years) using photometric spot modeling.

Physical parameters

Many of the stellar parameters are taken from Berdyugina et al. (1999b). They did a very detailed spectral line analysis to derive T_{eff} , $\log g$ and the abundances of IM Peg. They also re-determined the orbital parameters, which are listed in in table 4.4 along with the values from Fekel et al. (1999). We use the latter for calculating the rotational phases of our observations since the values for the orbital period agrees very well between the two studies. The discrepancy in γ is probably due to the different treatment of zero-point shifts: While Berdyugina et al. (1999b) optimizes γ for the individual observers, Fekel et al. (1999) notices an evolution of γ over time which could be due to another companion star. For this result to be significant, data more evenly distributed of over a longer range of time would be needed.

The inclination of the rotational axis (i) and the projected rotational velocity ($v \sin i$) can be determined by Doppler imaging. The parameter $v \sin i$ or i is varied in a given range while all other parameters are kept fixes. The goodness of the fit of the spectral line-profiles (χ^2) can then be used to determine the correct value of the parameter (see appendix A). The values derived here (see figure 4.16) agree well with the results from Berdyugina et al. (1999b). We therefore adopt $v \sin i$=26.5km s^{-1} and i=70°.

With the unspotted brightness of V=$5^{\mathrm{m}}.55$ and the unspotted color $V-I$=$1^{\mathrm{m}}.14$ (Ribarik et al. 2003), one gets an effective temperature of 4500±100 K using the tables from Bell & Gustafsson (1989). This agrees well with the value of 4450±50 given in Berdyugina et al. (1999b). The latter authors also determine the abundances to be of solar value. The Doppler images presented here are calculated with the abundances listed in table 4.5, which are considerably below the solar value. Due to the small number of spectral lines available here, distinguishing between the influences of the abundance and the $\log gf$ values is not possible. The code used here does also not include molecules, which could also contribute considerable to the discrepancy.

Table 4.4.: Orbital parameters of IM Peg.

Orbital element	Fekel et al. (1999)	Berdyugina et al. (1999b)
P (days)	24.648944 ±0.000075	24.64880±0.00005
T_0 (HJD)	2449227.690 ±0.022^a	2450342.883±0.007
γ ($\mathrm{km\,s^{-1}}$)	-15.47 ±0.13	-14.09±0.04
K_1 ($\mathrm{km\,s^{-1}}$)	34.30 ±0.17	34.42±0.06
e	0.0	0.006±0.007
$a_1 \sin i$ (10^6 km)	11.625 ±0.058	11.665±0.028
$f(M)$ ($\mathrm{M_\odot}$)	0.1033 ±0.0015	0.1042±0.0006

Table 4.5.: Stellar parameters of IM Peg.

Parameter	Value
Spectral type	K2 III
log g	2.5 ± 0.1
T_{eff}	4500 ± 100 K
V	5.55 mag
$(B-V)$	1.15 ± 0.006 mag
$(V-I)$	1.14 ± 0.01 mag
$v \sin i$	26.5±0.5 $\mathrm{km\,s^{-1}}$
Inclination i	70°±15°
Distance d	96.8±6.6 pc
Radius R	17^{13}_{28} $\mathrm{R_\odot}$
Rotation period P_{orb}	24.648944±0.000075 days
Equatorial velocity v_{equ}	28.2^{26}_{33} $\mathrm{km\,s^{-1}}$
Microturbulence ξ	1.5 $\mathrm{km\,s^{-1}}$
Macroturbulence $\zeta_{\mathrm{R}} = \zeta_{\mathrm{T}}$	4.0 $\mathrm{km\,s^{-1}}$
log$[Ca]$ abundance	0.8 dex below solar
log$[Fe]$ abundance	0.5 dex below solar

4.3.2. Observations

All spectroscopic observations of IM Peg were made during the 1996 NSO observing run. The spectroscopic log along with the radial velocities, and the signal-to-noise ratio is listed in table 4.6. The phases are calculated using the orbital solution from Fekel et al. (1999), and the *Rotational cycle* column shows which of the two Doppler imaging blocks the respective spectrum is assigned to. A dash in that column means either a bad-quality spectrum or that the spectrum was taken after the second block, where the time sampling was not good enough to construct a third image block. This is illustrated in figure 4.17, where rotational phase versus date is plotted.

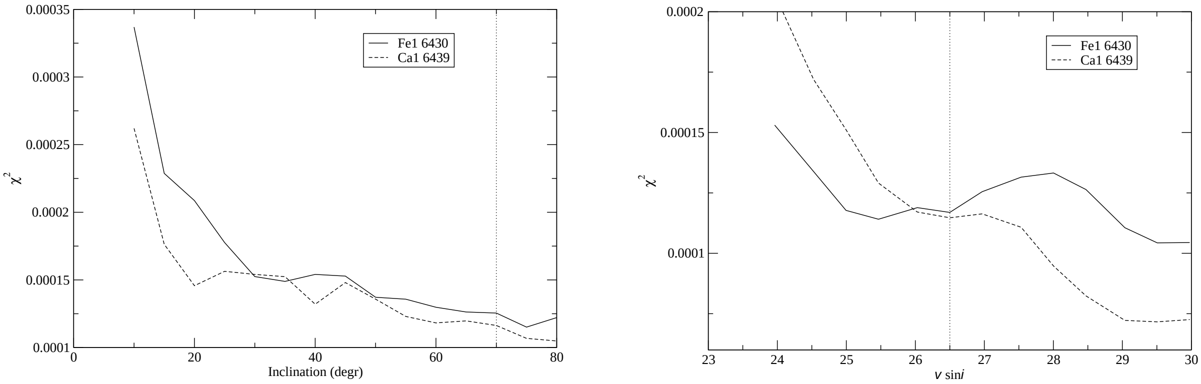

Figure 4.16.: Parameter variation to determine the correct inclination of the rotational axis (left) and the projected rotational velocity (right). Doppler images for a range of possible values in $v \sin i$ and i have been calculated, and the error in the line-profile fits (χ^2) is recorded. The region with the lowest χ^2 correspond to the correct parameter. The adapted values in both graphs are marked with a dotted line.

Table 4.6.: Spectroscopic log and radial velocity data.

HJD (24+)	Phase (°)	$v_{\rm rad}$ (km s^{-1})	$\sigma_{\rm rad}$	S/N	Rotational cycle	Telescope
2450391.631	79.5	-6.5	1.6	110	map 1	NSO
2450392.618	93.9	-29.5	1.4	125	-	NSO
2450393.622	108.5	-25.9	1.7	110	map 1	NSO
2450394.624	123.2	-34.1	1.2	125	map 1	NSO
2450395.614	137.6	-40.5	1.4	125	map 1	NSO
2450396.628	152.4	-43.9	2.0	110	map 1	NSO
2450398.683	182.5	-51.6	2.2	100	-	NSO
2450399.711	197.5	-49.3	1.9	110	map 1	NSO
2450400.608	210.6	-45.2	1.6	100	map 1	NSO
2450401.607	225.2	-39.8	2.1	110	map 1	NSO
2450404.621	269.2	-17.6	1.5	100	map 1	NSO
2450405.600	283.5	-8.0	2.2	90	map 1	NSO
2450406.603	298.1	1.5	1.8	110	map 1	NSO
2450407.605	312.8	6.3	2.0	100	map 1	NSO
2450408.607	327.4	16.1	1.9	110	map 1	NSO
2450409.595	341.8	15.9	1.8	100	map 1	NSO
2450411.598	11.1	18.4	1.6	100	map 1	NSO
2450412.592	25.6	14.4	1.4	100	map 1	NSO
2450413.590	40.2	11.1	1.9	100	map 1	NSO
2450414.594	54.8	4.2	1.5	100	map 1	NSO
2450415.591	69.4	-3.3	1.6	100	map 2	NSO
2450416.603	84.2	-12.8	2.0	110	map 2	NSO
2450417.679	99.9	-20.2	1.4	100	map 2	NSO
2450418.649	114.1	-29.7	2.3	100	map 2	NSO
2450419.581	127.7	-36.7	1.7	100	map 2	NSO
2450421.594	157.1	-45.7	2.6	100	map 2	NSO

Table 4.6.: Spectroscopic log of IM Peg (continued)

HJD (24+)	Phase (°)	v_{rad} (km s^{-1})	σ_{rad}	S/N	Rotational cycle	Telescope
2450422.585	171.5	-48.6	1.9	100	map 2	NSO
2450423.591	186.2	-50.6	2.2	100	map 2	NSO
2450424.598	200.9	-47.4	2.1	100	map 2	NSO
2450425.585	215.4	-44.0	2.0	100	map 2	NSO
2450426.608	230.3	-37.0	2.0	100	map 2	NSO
2450427.586	244.6	-29.2	1.5	100	map 2	NSO
2450429.586	273.8	-11.7	1.2	100	map 2	NSO
2450430.589	288.4	-2.5	2.1	100	map 2	NSO
2450432.588	317.6	10.6	1.8	100	map 2	NSO
2450433.571	332.0	14.9	1.8	100	map 2	NSO
2450434.583	346.8	17.6	1.5	100	map 2	NSO
2450435.591	1.5	17.8	1.2	100	map 2	NSO
2450436.618	16.5	17.0	1.7	100	map 2	NSO
2450437.567	30.4	13.4	1.5	100	map 2	NSO
2450438.572	45.0	16.4	2.1	110	map 2	NSO
2450440.598	74.6	-5.7	1.7	100	-	NSO
2450441.584	89.0	-14.9	2.6	100	-	NSO
2450446.577	162.0	-47.6	2.8	100	-	NSO
2450450.590	220.6	-41.6	1.6	100	-	NSO
2450451.581	235.0	-35.2	1.5	100	-	NSO
2450453.621	264.8	-15.3	2.6	75	-	NSO
2450457.607	323.0	12.4	2.1	100	-	NSO

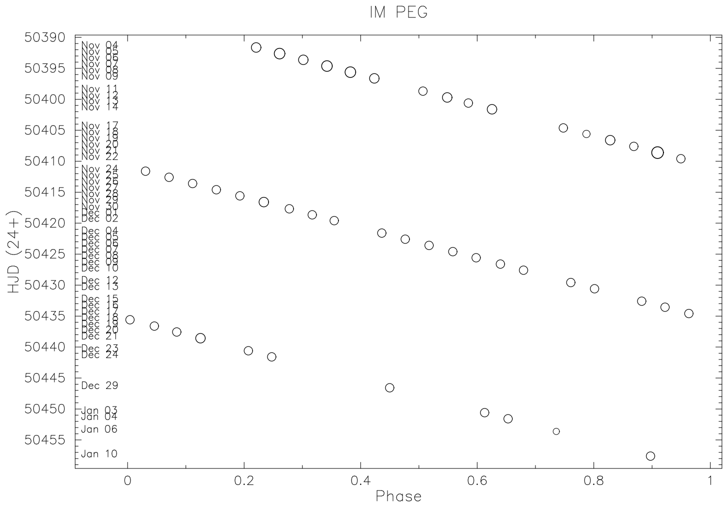

Figure 4.17.: Distribution of the rotational phases of IM Peg versus date. The sizes of the circles are proportional to the S/N ratio of the spectra, where the average value is about 100:1.

4.3.3. Time-series Doppler imaging

The Doppler images for the two different sets defined in table 4.6 have, together with the combined map, a very similar appearance (see figure 4.18). The agree-

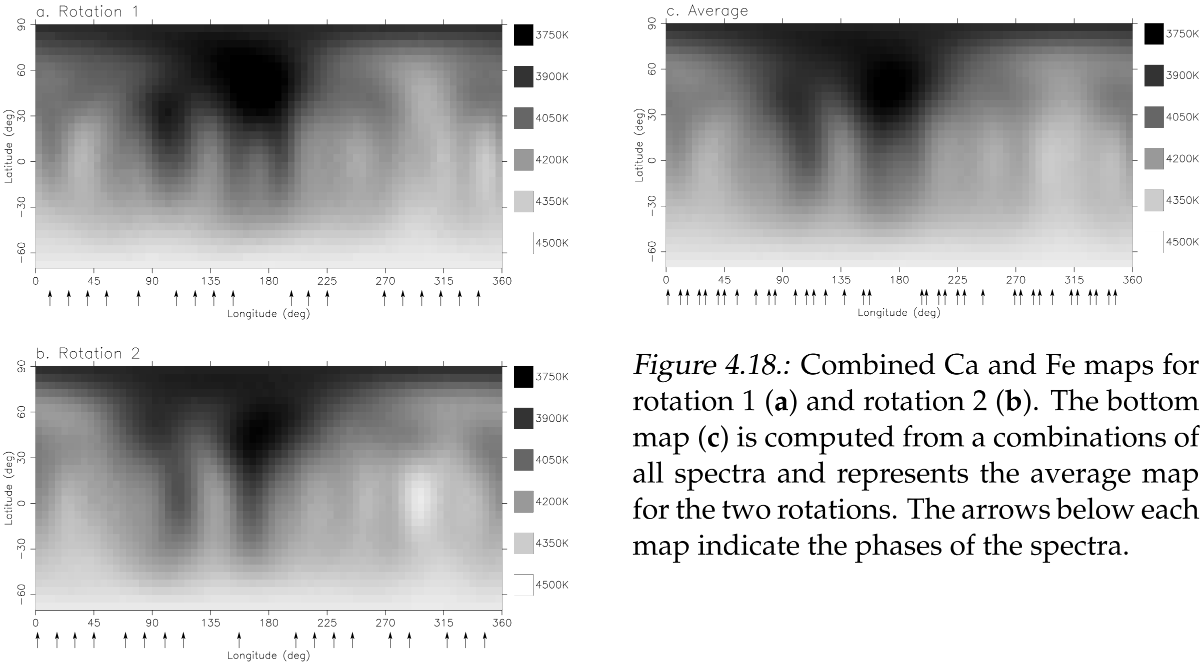

Figure 4.18.: Combined Ca and Fe maps for rotation 1 (**a**) and rotation 2 (**b**). The bottom map (**c**) is computed from a combinations of all spectra and represents the average map for the two rotations. The arrows below each map indicate the phases of the spectra.

ment with the images computed by Berdyugina et al. (2000) for the second half of 1996 is very good. All images are dominated by one huge spot at a longitude of ≈180° and a latitude of ≈50°. There is another smaller spot at $\ell \approx 100°$, and one at the opposite side from the first one at 0°, which is difficult to see in the pseudo-Mercator view used here. The individual maps, including line-profile an light-curve fits, are show in figure 4.19 and 4.20 for the first and second rotation, respectively.

The lightcurve shown in the bottom of the figures with the individual Doppler images, reveal a large amplitude of approximately $0\overset{m}{.}4$ with a very symmetrical sinusoidal shape. This is because the dominant feature on the surface is one single big spot. Looking at the photometric history of the star in Ribarik et al. (2003) one notices that about five years earlier or later, the lightcurve was very flat with an amplitude of less than $0\overset{m}{.}1$. This is a sign that the spots were distributed stochastically over the stellar surface. This behavior is similar to the star HD 208472 (discussed in the previous chapter), with the noteworthy difference that IM Peg was caught in the opposite state than HD 208472. This is already a sign for an activity cycle, which redistributes the spots on the stellar surface, but leaves the fraction of surface covered roughly constant. This is in contrast to the solar case, where the activity cycle goes hand in hand with a variation of the total spot area.

Cross-correlation analysis

Average images for each of the two stellar rotations were constructed using the individual images from the respective spectral line region. These two resulting images were then cross-correlated with each other. The resulting image is shown in figure 4.21 (left). It is obvious that a fit to this cross-correlation could not produce a significant result. Therefore the number of spectral phases making up the original Doppler imaging was decreased randomly by at most five. For each of the

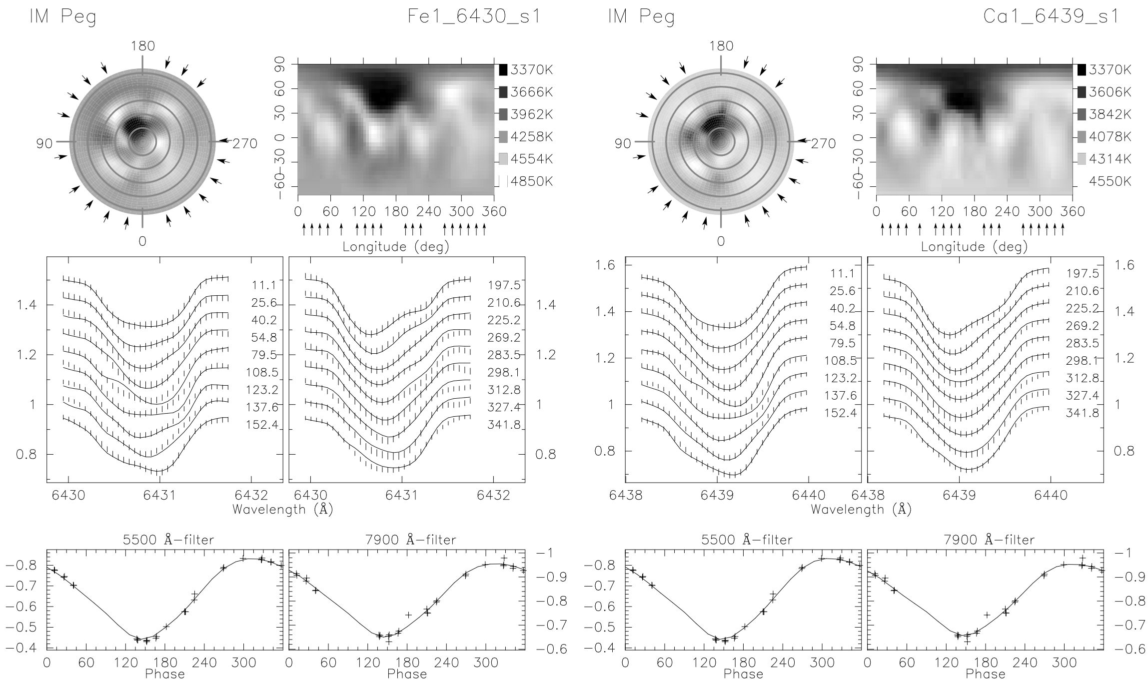

Figure 4.19.: Individual Doppler images for rotation 1. **a** Fe I 6430, and **b** Ca I 6439. Temperature maps from the individual lines are plotted in a pole-on view and a pseudo-Mercator (top row) projection where the arrows indicate the spectroscopic phase coverage. The observed and computed line profiles are shown in the middle row, and observed and computed V and I_C-lightcurves in the bottom row. The pluses and the bars are the observations and the full lines are the fits. The size of the bars correspond to a $\pm 1\,\sigma$ error per data point.

four original data sets (two rotations, two spectral regions) 50 permutations were randomly picked. Again, 100 average images were formed from the resulting 200 Doppler maps, which in turn lead to 50 cross-correlation images.

In a first attempt to measure the differential rotation more accurately, to each latitudinal bin in these images a Gaussian was fit. The average of the resulting 50 differential rotation functions is plotted on top of the left image in figure 4.21. The coefficients for the corresponding solar-like differential rotation law are listed in the first row (labeled *Average*) of table 4.7. The standard deviation of Ω_1 is very close to the actual value, marking this measurement not very reliable.

The second attempt to measure the differential rotation function was done by averaging the 50 cross-correlation images derived through the Monte-Carlo technique described above. The averaging was performed three times, once for high/low rejection values of 0, 15%, and 30%, respectively. To each of these three images a differential rotation function was fitted, the average result of these three measurements and its standard deviation is listed in the second row (marked “Single”) of table 4.7. Since this measurement is by far more accurate than the others, it is used throughout this section as a comparison.

And finally as done with the other stars in this study, the available spectra were split up into subgroups, each 24.65 days (one stellar rotation period) of length and 3 days separated fro each other. For each of these subgroups, a Doppler image for both spectral regions was computed. From this time-series of images, pairs being

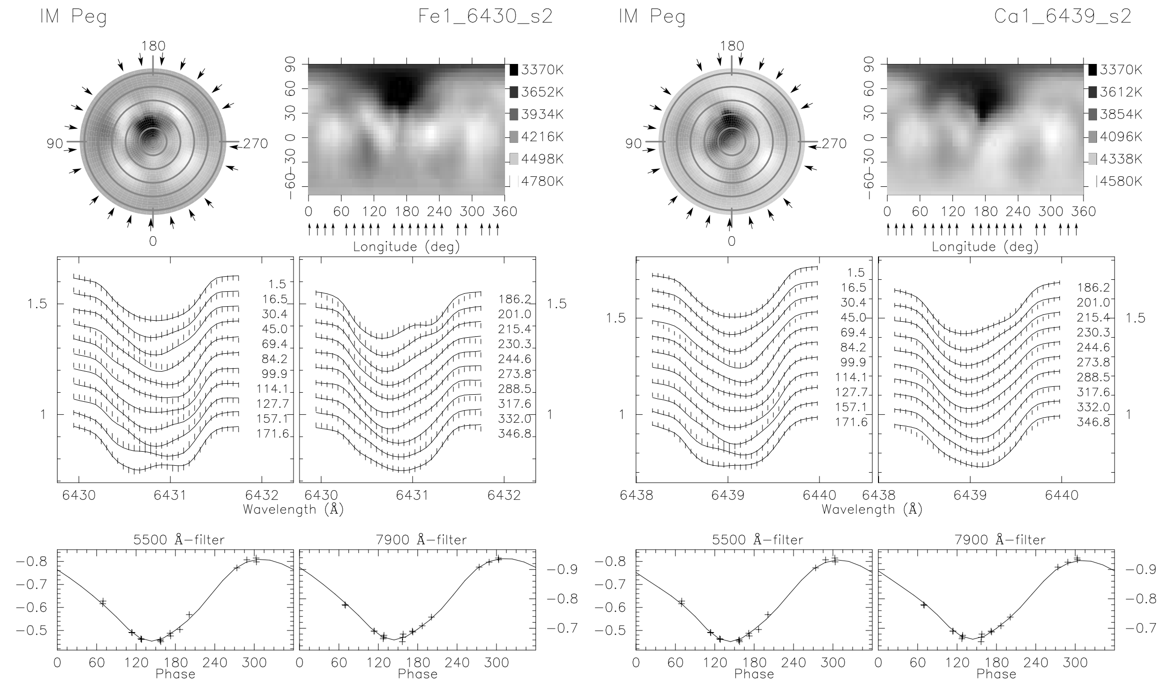

Figure 4.20.: As Fig. 4.19 but for the second rotation.

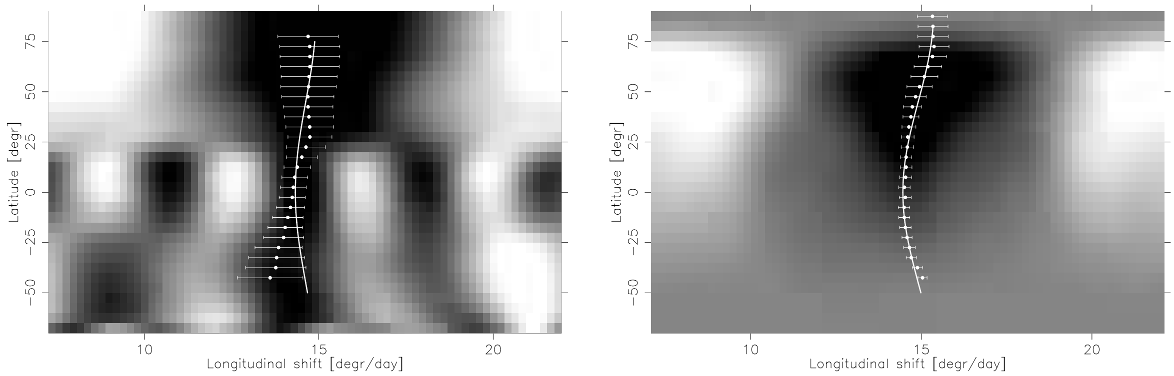

Figure 4.21.: Differential rotation of IM Peg. **left**. The cross-correlation image of the two average images is shown along with the average measurement of every latitudinal bin with its corresponding errors. The dashed line shows a anti-solar differential rotation law fitted to theses data points (see text). **right**. The average of 50 cross-correlation images derived through Monte-Carlo variations of the number of spectral data points used in the computation of the Doppler images. Again, the points are Gaussian fits for each latitude bin, the solid line a fit using a solar-like differential rotation law.

separated by about one half of a stellar rotation (18 days = 6 time intervals) were cross correlated with each other. The average cross-correlation images are shown in figure 4.22, the average fit to the measured cross-correlation function (again average from 0, 15%, and 30% rejection values) is listed in the third row (marked “Time-series”) of table 4.7

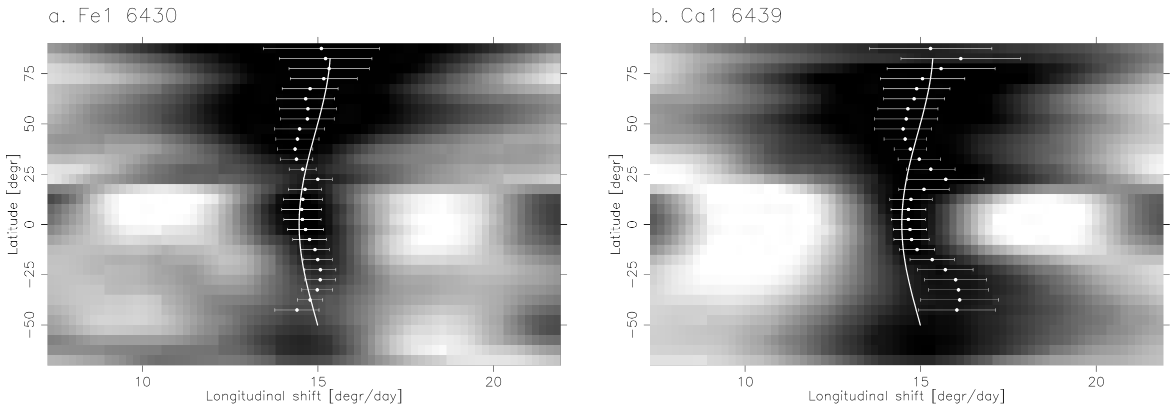

Figure 4.22.: Differential rotation of IM Peg. The average of 15 cross-correlations derived by making a time-series of Doppler images and cross correlation all pairs with a time separation of about $1/2P_{\mathrm{rot}}$. Fe I 6430 is shown left, Ca I 6439 right. The points are measured fitting Gaussians to the image shown, the solid line the fit derived from the "Monte-Carlo"–technique (see text).

Differential rotation measurement using TempMap

As in other stars in this work, the signal-to-noise ratio of the spectra are approximately 100 to 120. This is the lower limit for using the Doppler-imaging technique and certainly a bit too low to detect signals as small as the differential rotation. This is said as a caution to not over-interpret the following results.

A two dimensional parameter search in α and P_{equ} was performed on the combined data set. For each combination of α and P_{equ} one Doppler image was obtained and the quality of the line-profile fits (χ^2) computed. A minimum in the resulting χ^2-landscape would then correspond to the most probable parameter combination.

Figure 4.23 shows the two χ^2-landscapes for the respective line profile region plus their average. Both images show weak minima around α=-0.02 and -0.1 and P_{equ}=24.2 and 24.6 days. This agrees roughly with the results obtained with the cross-correlation technique. Looking at the individual results from the cross-correlation technique, one finds that for Fe I 6430 P_{equ} is 24.5 days and for Ca I 6439 P_{equ} is 24.0 days, while the α values are approximately -0.02 in both cases. In the average χ^2-landscapes the two local minima in the individual maps merge to one larger area. The tilt in the contour lines (from bottom-left to top-right) is accordance with the expected slope produced by a single spot at high latitudes (see sect A.2.2). Estimating the location for the smallest χ^2 from this map one gets P_{equ}=24.25±0.25 days, and α=-0.05±0.05.

Results for the second subset

Since later during the NSO 1996 observing run the quality of the data increased, the same analysis was done using only the data set from the second rotation. The result should be about the same, since the increase in signal of the spectra should be at least outweighed (if not over-weighted) by the loss of half of the data. Also, since the rotation period is as long as the length of this data set, varying the rotation period should not have a large impact on the result. This adds a larger

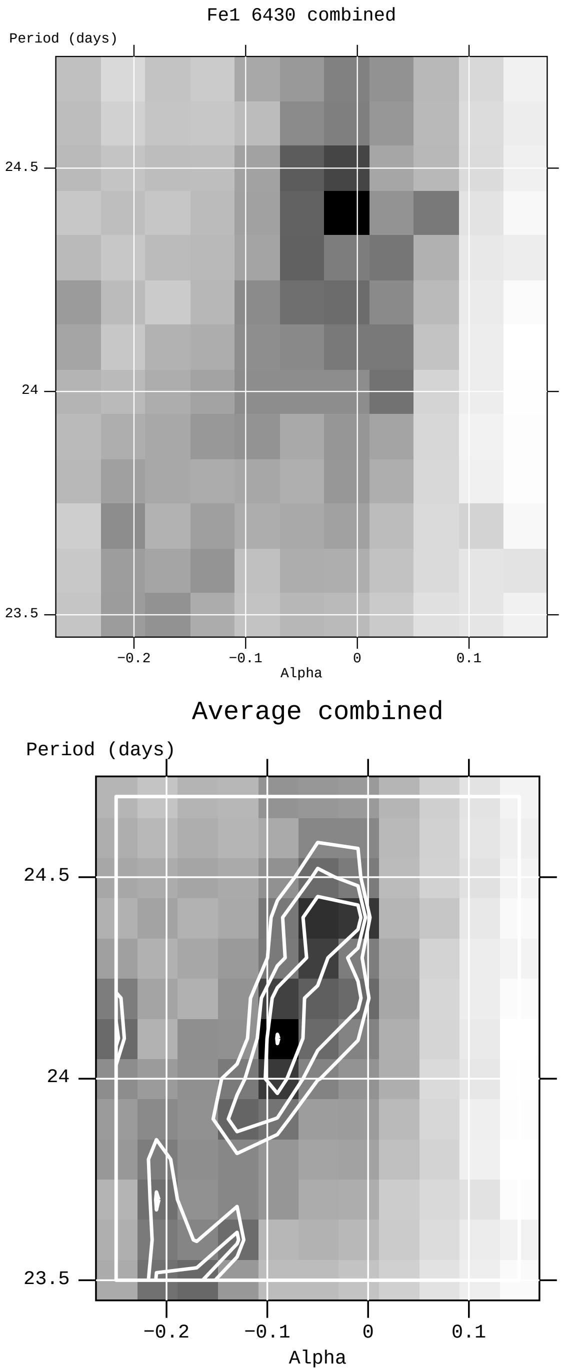

Figure 4.23.: χ^2 maps using the combined data set. Fe I 6430, Ca I 6439, and the combination of those two.

ambiguity to the equatorial rotation period (see section A.2.2 for an illustration). Figure 4.24 shows the result for the two spectral line regions and their average. Besides the fact that the χ^2-valleys are now more elongated in direction of the period, the results are similar, but as expected no improvement can be seen. Again, the best fit in P_{equ} tends to be at bigger periods for Fe I 6430, and α is smaller for Ca I 6439 (in this case practically zero).

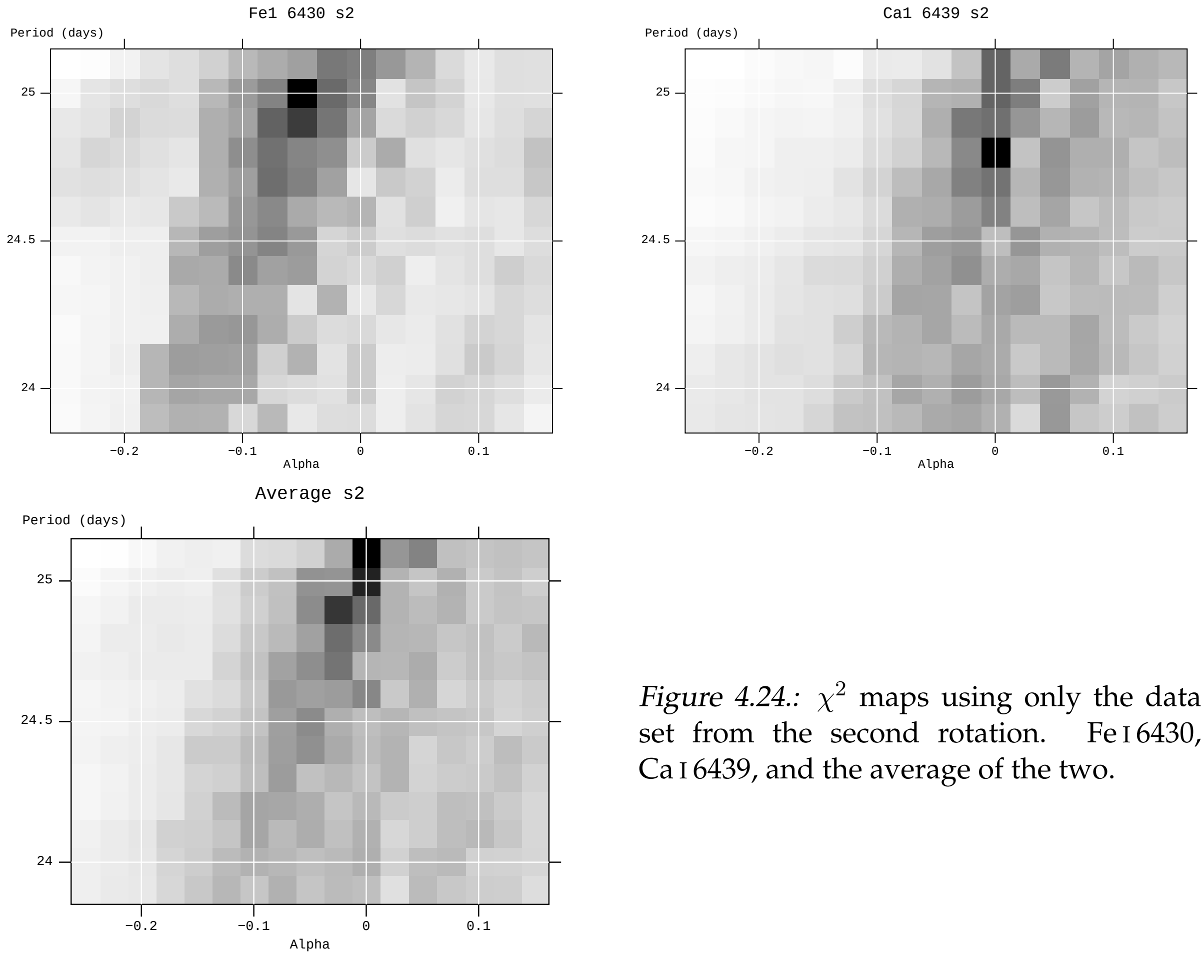

Figure 4.24.: χ^2 maps using only the data set from the second rotation. Fe I 6430, Ca I 6439, and the average of the two.

Summary

The results for the different techniques to derive the differential rotation value are summarized in table 4.7. The values agree to a large extent, but the uncertainties are too large to draw firm conclusions. There is good evidence that this star rotates differentially in the sense that the pole rotates faster than the equator. The hardest evidence being the cross-correlation results based on averaging many images. We therefore use this value (labeled *Average* in table 4.7) for further analysis, since it is the only significant result.

Table 4.7.: Differential rotation parameters derived from cross-correlation.

	Ω_0	Ω_1	α
Average	14.40±0.19	0.58±0.42	−0.04±0.03
Single	14.33±0.33	0.60±0.73	−0.04±0.05
Time-series	14.83±0.55	0.33±0.35	−0.02±0.02
χ^2	14.85±0.15	0.74±0.74	−0.05±0.05

But even the χ^2-landscape technique applied here is in good agreement with the former results, although by itself it would not be significant. It can also be noted, that the results from the χ^2-landscape technique benefit from datasets which overlap, since the information concerning the rotation period and the extent of shear lies mainly in these overlaps. Cross-correlation of just two consecutive images appears to be the worst method to reconstruct differential rotation. If this is due to small changes on the stellar surface that are mixed up with the large scale evolution, or if it is merely a question of higher signal to noise for the averaged images, or a combination of both cannot be safely concluded here.

4.4. IL Hya

IL Hydrae (= HD 81410, $\alpha = 9^h24^m49^s$, $\delta = -23°49'33"$, 2000.0, V = 7.25-7.9 mag) is an evolved double-lined spectroscopic binary with very strong Ca II H & K emission. This and the fact that the photometric period (Eggen 1973) is very close to the orbital period of 12.9 days makes IL Hydrae a typical RS CVn star (Fekel et al. 1986). Randich et al. (1993) performed a spectrum synthesis in the 6700-Å region and found an iron abundance of 0.5 dex below solar and a moderate Lithium abundance of $\log n(\mathrm{Li}) = 1.35$. The secondary star can not be seen in near-ultraviolet spectra (La Dous & Giménez 1994) but from the difference of the measured $UBV(RI)_C$ colors of IL Hya to standard values Cutispoto (1995) estimated the secondary to be a G8V star. Shortly thereafter, the secondary component was detected by Donati et al. (1997) in two spectra at optical wavelengths. Fekel et al. (1999) calculated a SB2 orbit with a larger number of radial velocities from the secondary star (most of them based on observations used here). IL Hydrae is also represented in the long-term photometric studies by Oláh et al. (2000), who find a photometric cycle period of 13 years, and by Strassmeier et al. (1999), who find the average photometric period to be 12.674 days.

4.4.1. Observations

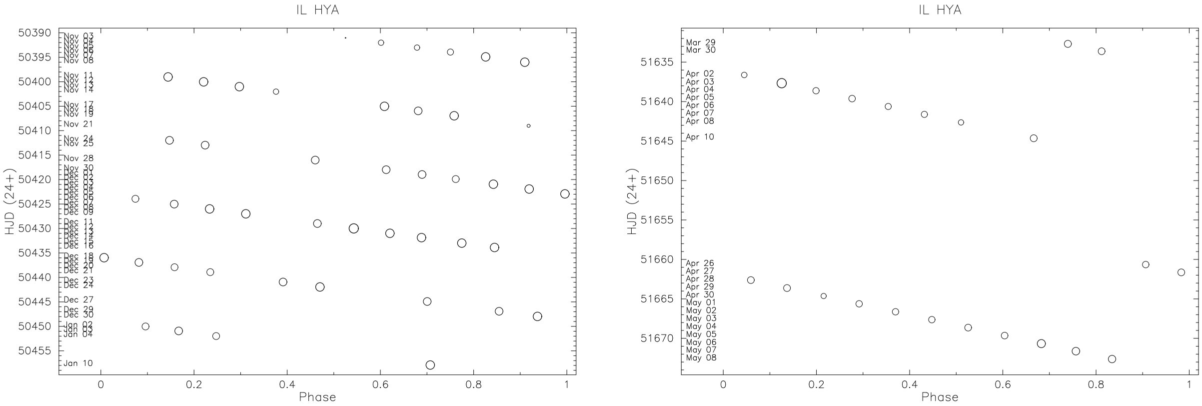

Figure 4.25.: Distribution of the rotational phases of IL Hya versus date for the 1996/97 NSO run (**left**) and for the 2000 KPNO run (**right**). The sizes of the circles are proportional to the S/N ratio of the spectra, where the average value is about 150:1.

The spectroscopic observations marked with *NSO* in column *Telescope* of Table 4.8 were obtained at the National Solar Observatory (NSO) with the McMath–Pierce main telescope between October 31, 1996 and January 8, 1997. The record of the rotational phases (period=12.904982 days and ephemeris= 2447093.4936 from Fekel et al. (1999)) versus the day of observation is shown in Fig. 4.25. Additional spectra in the 6430-Å region along with corresponding reference spectra, were obtained at Kitt Peak National Observatory (KPNO) with the coudé feed telescope and the TI-5 CCD in December 1997/January 1998 (marked *KP5* in Table 4.8). Furthermore, 23 spectra in the 6500-Å region including Hα were obtained with the same instrumental set-up but using the F3KB CCD at the coudé feed telescope in March, April, and May 2000 (marked *KPKB* in Table 4.8). Detailed instrument setup and the respective spectral resolution is discussed in section 4.1.1. The radial velocity measurements (see column $v_{\rm rad}$ in Table 4.8) were obtained using the following velocity standards: β Gem (K0III, $v_{\rm r} = 3.3$ km s^{-1}) of the KPNO spectrum from JD 2 450 821, 16 Vir (K0.5III, $v_{\rm r} = 35.7$ km s^{-1}) for the KPNO spectra from JD 2 450 918, and JD 2 450 921, and α Ari (K2III, $v_{\rm r} = -14.3$ km s^{-1}) for the KPNO spectra from JD 2 450 826 and JD 2 450 828 and all NSO spectra.

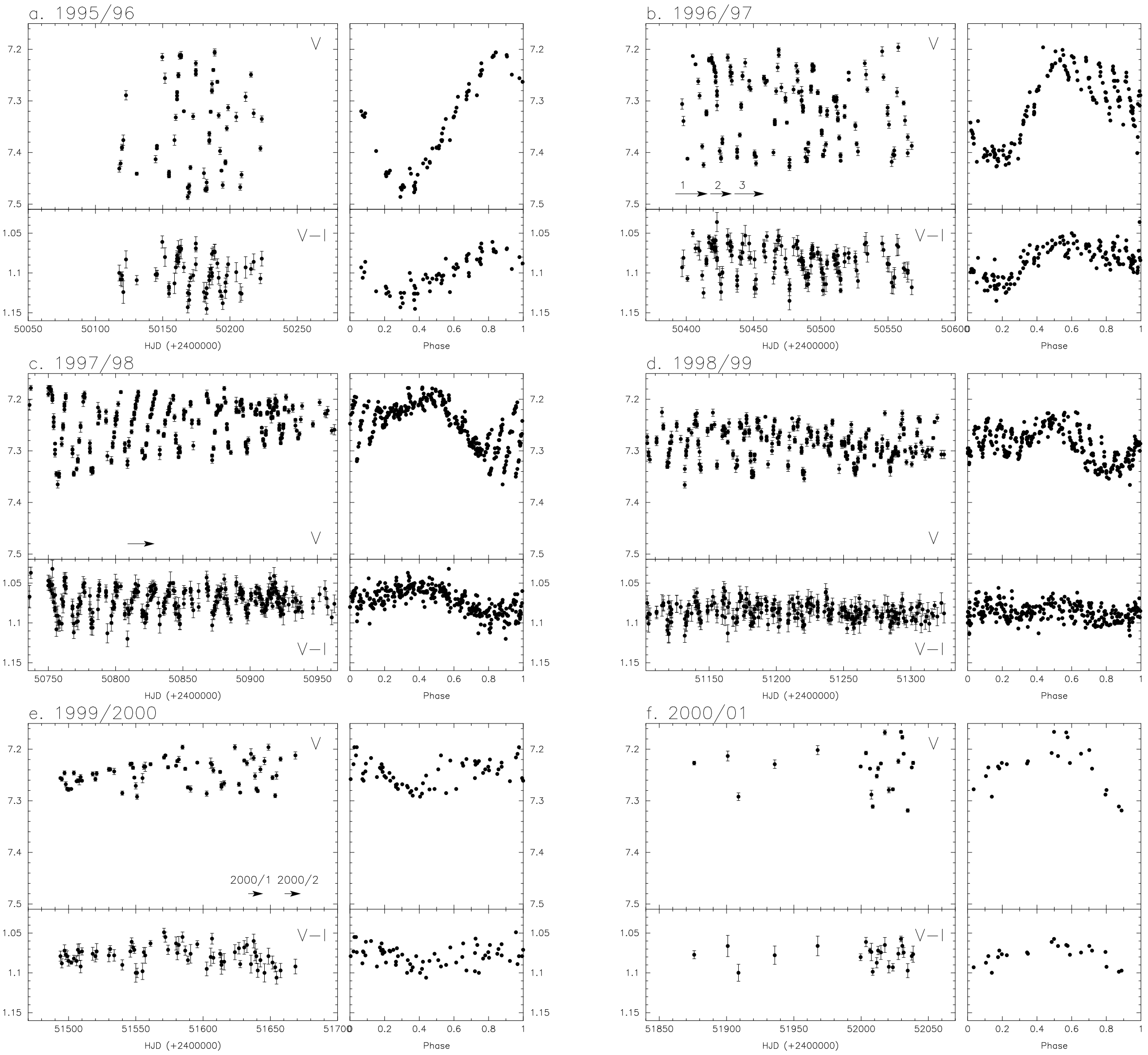

Figure 4.26.: Six years of photometry of IL Hya. **a.** The 1995/96 APT data versus Julian date and versus phase calculated with the orbital period (12.904982 days) and ephemeris (2447093.4936) from Fekel et al. (1999), **b**, **c.**, **d.**, **e.** and **f.** like panel **a** but for the 1996/97, 1997/98, 1998/99, 1999/2000 and 2000/01 seasons, respectively.

The photometric data were obtained with the Amadeus 0.75-m automatic photoelectric telescope (APT), part of the University of Vienna twin APT at Washington Camp in southern Arizona (Strassmeier et al. 1997). The observations were made differentially with respect to HD 218610 as the comparison star ($V = 7\overset{\rm m}{.}64$, $V - R_C = 0\overset{\rm m}{.}69$, $V - I_C = 1\overset{\rm m}{.}30$) and SAO 91066 as the check star. The data cover the time interval JD 2,450,395–568 (163 data points, season 1996/97), JD 2,450,736–

963 (316 data points, season 1997/98), JD 2,451,100–325 (291 data points, season 1998/99), JD 2,451,494–669 (67 data points, season 1999/2000), and JD 2,451,875–2,039 (23 data points, season 2000/01). All photometry was transformed to match the Johnson-Cousins $V(RI)_C$ system.

Details about the observing runs, the telescopes used, the instrument setup, the data reduction software used and the reduction procedure applied can be found in section 4.1.1 and 4.1.2 for the spectroscopic and photometric observations, respectively.

Table 4.8.: Spectroscopic log and radial velocity data ($v_{\rm rad}$).

HJD	Phase	$v_{\rm rad}$	$\sigma_{\rm rad}$	$v_{\rm rad}$	$\sigma_{\rm rad}$	S/N	Rotational	Telescope
(24+)	(°)	prim. (km s^{-1})		sec. (km s^{-1})			cycle	
50391.041	189.0	-54.9	4.2			10	-	NSO
50392.024	216.5	-44.7	2.4			70	map 1	NSO
50393.020	244.3	-33.0	2.9			70	-	NSO
50393.946	270.1	-4.7	1.8			80	map 1	NSO
50394.921	297.3	8.8	1.5			110	map 1	NSO
50396.006	327.5	27.5	1.8			110	map 1	NSO
50399.032	52.0	16.5	1.4			110	map 1	NSO
50400.016	79.4	-2.1	1.6			110	map 1	NSO
50401.006	107.0	-20.1	1.9			110	map 1	NSO
50402.021	135.4	-36.6	2.5			70	-	NSO
50405.024	219.1	-42.0	2.0			110	map 1	NSO
50405.959	245.2	-26.6	1.9			100	map 1	NSO
50406.953	272.9	-6.9	1.5			110	-	NSO
50409.016	330.5	32.5	1.3			100	map 1	NSO
50411.975	53.0	18.9	1.7			100	map 1	NSO
50412.963	80.6	-2.6	1.6			100	-	NSO
50416.012	165.6	-49.4	1.8			100	map 1	NSO
50417.976	220.4	-39.8	1.5			100	map 2	NSO
50418.970	248.2	-24.4	1.8			100	map 2	NSO
50419.904	274.2	-6.0	2.2			90	-	NSO
50420.944	303.2	14.1	1.4			110	map 2	NSO
50421.938	331.0	28.0	1.2			110	map 2	NSO
50422.926	358.5	34.5	1.5			110	map 2	NSO
50423.937	26.7	28.9	1.5			90	map 2	NSO
50425.010	56.7	13.7	1.8			100	-	NSO
50425.991	84.0	-3.8	1.7			110	map 2	NSO
50426.995	112.0	-24.3	2.2			110	map 2	NSO
50428.978	167.3	-50.7	2.5			100	map 2	NSO
50429.984	195.4	-49.2	1.9			120	map 2	NSO
50430.986	223.4	-37.7	1.8			110	map 2	NSO
50431.859	247.7	-26.6	1.7			110	map 2	NSO
50432.975	278.9	-3.8	1.4			110	map 2	NSO
50433.882	304.2	15.4	1.8			110	map 2	NSO

Table 4.8.: Spectroscopic log of IL Hya (continued)

HJD (24+)	Phase (°)	$v_{\rm rad}$ prim.	$\sigma_{\rm rad}$ (km s^{-1})	$v_{\rm rad}$ sec.	$\sigma_{\rm rad}$ (km s^{-1})	S/N	Rotational cycle	Telescope
50435.973	2.5	34.9	1.3			110	map 3	NSO
50436.938	29.4	27.3	1.6			100	map 3	NSO
50437.925	56.9	15.8	1.9			90	map 3	NSO
50438.915	84.6	-3.2	1.8			90	-	NSO
50440.931	140.8	-42.3	1.9			100	map 3	NSO
50441.954	169.3	-49.2	2.1			110	map 3	NSO
50444.923	252.2	-22.7	1.8			100	-	NSO
50446.913	307.7	16.8	1.9			100	map 3	NSO
50447.976	337.3	29.9	1.5			110	map 3	NSO
50450.026	34.5	25.8	1.7			90	map 3	NSO
50450.946	60.2	12.7	1.7			100	-	NSO
50451.983	89.1	-8.3	2.0			90	-	NSO
50457.914	254.6	-18.9	2.0			110	map 3	NSO
50809.815	351.3	34.6	0.6	-77.7	4.9	130	map 6	KP5
50811.863	48.4	20.4	0.5	-49.7	15.2	130	map 6	KP5
50812.974	79.4	-0.4	0.6			130	map 6	KP5
50813.936	106.2	-17.5	0.9			140	map 6	KP5
50814.856	131.9	-37.8	0.9	33.8	20.1	140	map 6	KP5
50819.922	273.2	-7.2	0.8			140	map 6	KP5
50820.922	301.1	13.2	0.5	-42.4	12.5	130	map 6	KP5
50821.931	329.2	27.9	0.6	-67.5	11.9	130	map 6	KP5
50822.914	356.7	34.4	0.8	-79.2	6.8	140	map 6	KP5
50825.972	82.0	-3.5	0.8			140	map 6	KP5
50826.921	108.4	-20.9	0.8			130	map 6	KP5
50828.018	139.1	-41.7	0.9	42.1	18.6	130	map 6	KP5
50828.914	164.0	-50.3	0.9	52.9	6.3	140	map 6	KP5
51632.686	266.2	-10.7	0.3			190	map 7	KPKB
51633.622	292.3	7.4	0.3			184	map 7	KPKB
51636.628	16.2	33.4	0.3			150	map 7	KPKB
51637.667	45.2	22.6	0.2			250	map 7	KPKB
51638.616	71.7	5.0	0.4			171	map 7	KPKB
51639.615	99.5	-13.8	0.4			177	map 7	KPKB
51640.616	127.4	-33.1	0.4			166	map 7	KPKB
51641.617	155.4	-46.7	0.4			167	map 7	KPKB
51642.631	183.7	-50.6	0.3			146	map 7	KPKB
51644.646	239.9	-29.1	0.4			187	map 7	KPKB
51660.653	326.4	26.8	0.3			176	map 8	KPKB
51661.638	353.9	34.2	0.3			185	map 8	KPKB
51662.621	21.3	32.4	0.4			184	map 8	KPKB
51663.624	49.3	20.4	0.3			185	map 8	KPKB
51664.637	77.5	1.4	0.4			142	map 8	KPKB
51665.622	105.0	-17.1	0.5			174	map 8	KPKB
51666.630	133.1	-37.2	0.4			173	map 8	KPKB

Table 4.8.: Spectroscopic log of IL Hya (continued)

HJD (24+)	Phase (°)	$v_{\rm rad}$ prim.	$\sigma_{\rm rad}$ (km s^{-1})	$v_{\rm rad}$ sec.	$\sigma_{\rm rad}$ (km s^{-1})	S/N	Rotational cycle	Telescope
51667.634	161.2	-49.0	0.4			174	map 8	KPKB
51668.639	189.2	-51.0	0.7			183	map 8	KPKB
51669.650	217.4	-42.6	0.5			180	map 8	KPKB
51670.668	245.8	-25.6	0.4			218	map 8	KPKB
51671.624	272.4	-7.0	0.3			205	map 8	KPKB
51672.625	300.4	12.4	0.3			200	map 8	KPKB

4.4.2. Time-series Doppler imaging

As indicated in table 4.8, the observations from the NSO run are divided into three blocks. Although five stellar roatations are covered, decent phase-coverage is only obtained by decreasing the number of blocks. This can be seen in the phase-diagram in figure 4.25. The observations from the KPNO run 1997/98 span exactly one rotation and are the set with the best signal/noise ratio and with the best spectral resolution. The observations from spring 2000 cover two stellar rotations exactly with one stellar rotation separation, and are thus subdivided into two sets. This results in six independent data sets spanning almost four years. Together with the previously published images (Weber & Strassmeier 1998), the Doppler imaging history of IL Hya spans six years.

Due to contaminations from the secondary star's Fe I 6409 line, the Fe I 6411 line could not be used here. The usable spectral lines are therefore the Fe I 6393 line (KPNO only) and the usual Fe I 6430 and Ca I 6439 lines.

Cross-correlations

Analogous to the other stars observed at NSO in Fall 1996, the long data set was subdivided into independent subsets, each approximately one stellar rotation period long. Here a time window of fifteen days was used instead of the rotation period to improve the phase coverage, and the median time-difference between to adjacent subdivisions is three days. This results in 17 different Doppler images for each of the two mapping lines. Each Doppler image is computed using seven to twelve observations, depending on the weather-dependent density of the observations. Doppler-images with a time separation of about one stellar rotation period (12.9 days) were cross-correlated, producing fourteen cross-correlation maps for each spectral line region. These cross-correlation maps were corrected to match exactly the 12.9 days, since the exact time difference between to maps is slightly random due to varying phase coverage.

For each mapping line, three versions of the average cross-correlation image was produced. One using all values, one rejecting the highest and lowest two values (15%) for each pixel, and one rejecting the highest and lowest four values (30%). The cross-correlation was measured for all three maps fitting a Gaussian profile to the cross-correlation peak for each longitudinal strip. The difference between the three measurements represents the errors contained in single line-profiles (3σ).

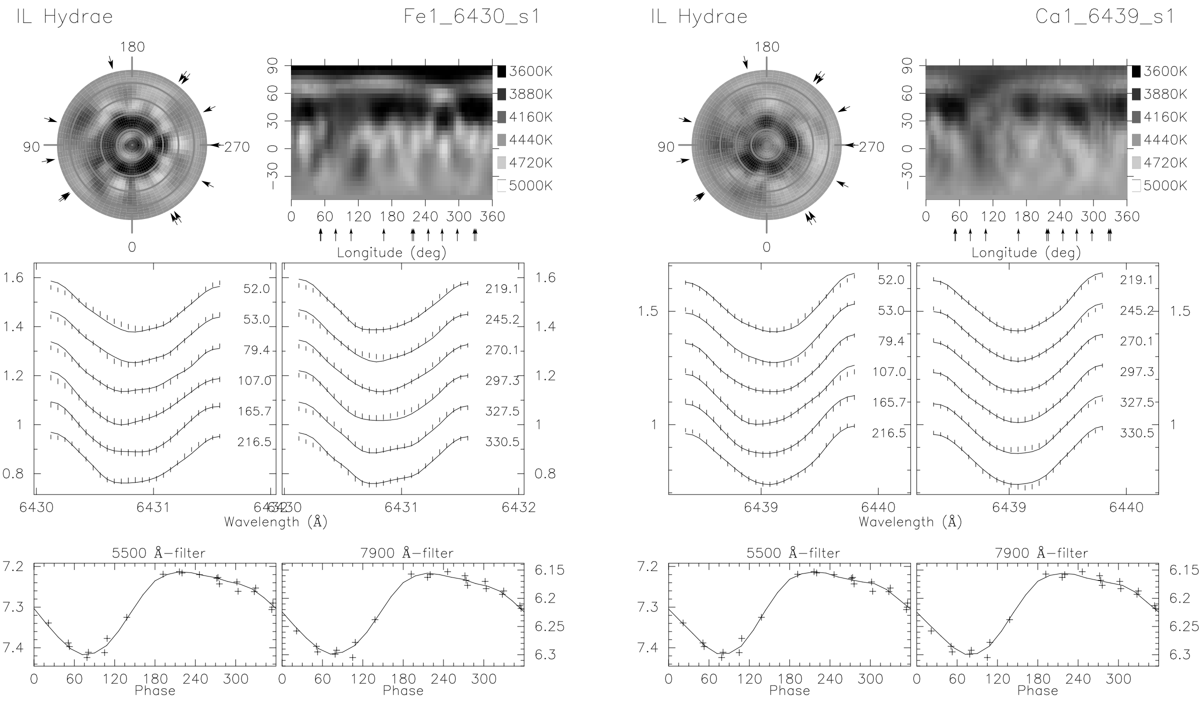

Figure 4.27.: Individual Doppler images for the first subset of the NSO 1996 data. The map from the Fe I 6430 line is shown at the left, the map from Ca I 6439 at the right. Temperature maps from the individual lines are plotted in a pole-on view and a pseudo-Mercator (top row) projection where the arrows indicate the spectroscopic phase coverage. The observed and computed line profiles are shown in the middle row, and observed and computed V and I_C-lightcurves in the bottom row. The pluses and the bars are the observations and the full lines are the fits. The size of the bars correspond to a $\pm 1\,\sigma$ error per data point.

The results are listed in row *Average cc 1996* of table 4.9. For comparison, all cross-correlation maps from both spectral line regions are averaged (rejecting the highest and lowest 15%), the peaks of the cross-correlation functions measured, and a differential rotation law was fitted to this data (figure 4.34). This result is listed in row *Combined cc 1996* of table 4.9 along with the formal error from fitting the differential rotation law to the cross-correlation peaks.

We also cross-correlated the images from the KPNO 2000 observing run. The results for the three usable spectral line regions is shown in figure 4.35. The three images do not agree well with each other, so it is not a big surprise that the differential rotation function derived in the next section does not fit the average cross-correlation image from that data. One reason for this disagreement could be the far from perfect phase coverage, especially in the first observing block (dubbed “s7” in section 4.4.2). Another problem arises due to the light from the secondary star. Most of the time the lines are not influenced by the light from the secondary, but in time of conjunction the signal size of the secondary is comparable to a spot signature. This dataset is probably more susceptible to this effect than the 1996 data, since the surface contrast was obviously smaller in 2000 than it was in 1996 (as seen by the decrease of the lightcurve amplitude by a factor of two). Also, the averaging performed with the 1996 data minimizes this effect. This could be verified by including a model of the secondary in the Doppler imaging procedure,

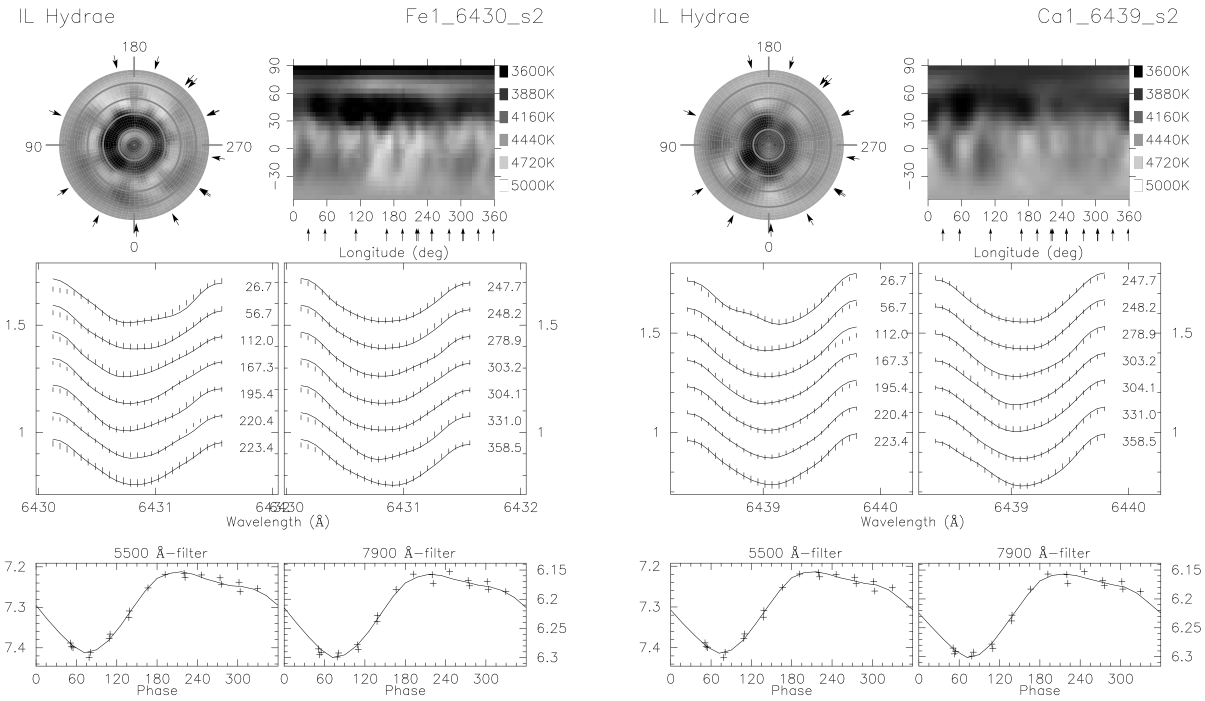

Figure 4.28.: As in figure 4.27 but for the second (middle) subset of the NSO 1996 data.

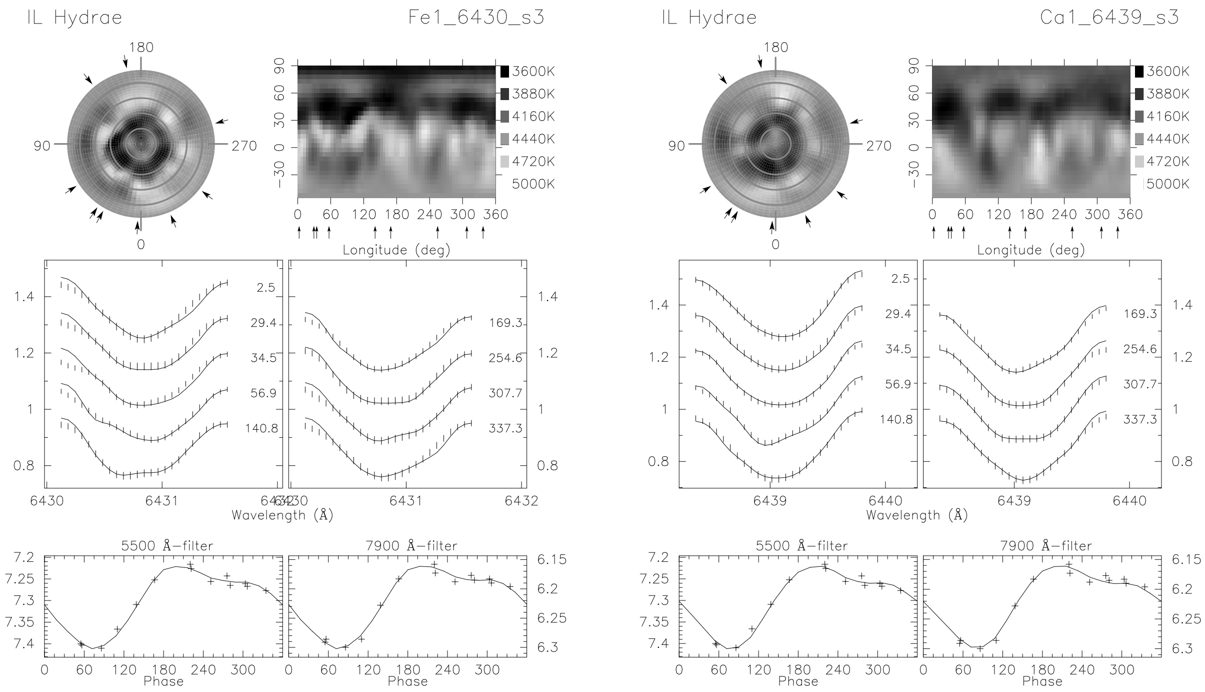

Figure 4.29.: As in figure 4.27 but for the third (and last) subset of the NSO 1996 data.

but this task is outside of the scope of this work.

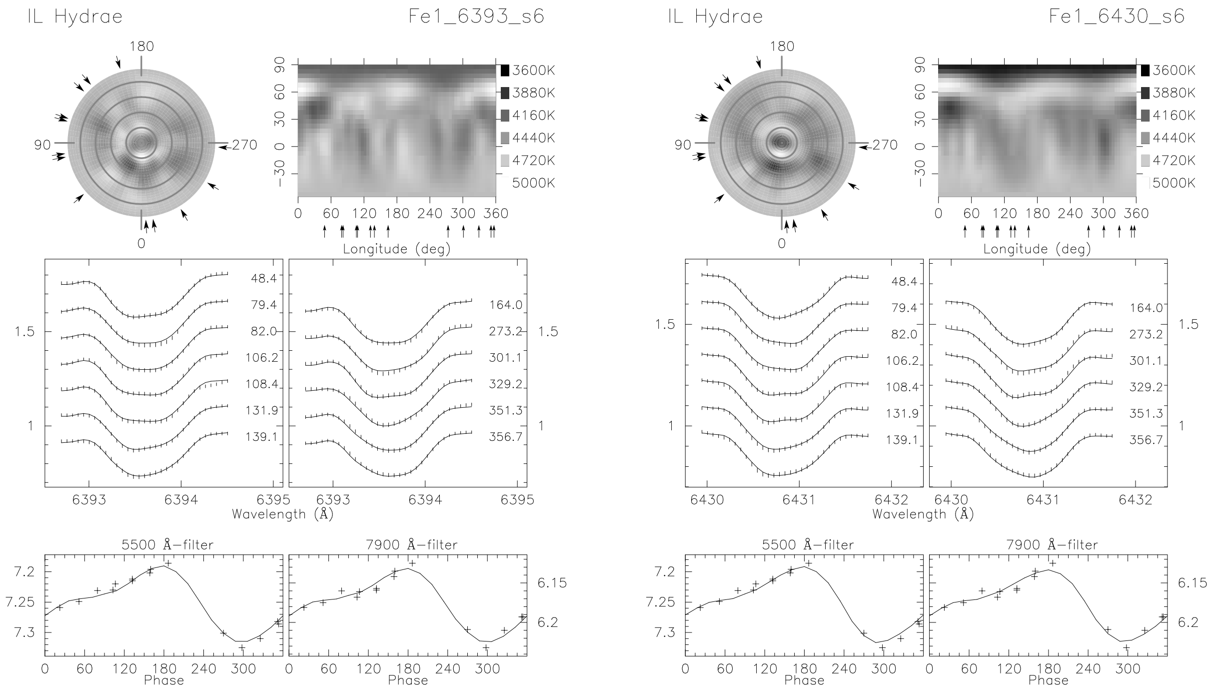

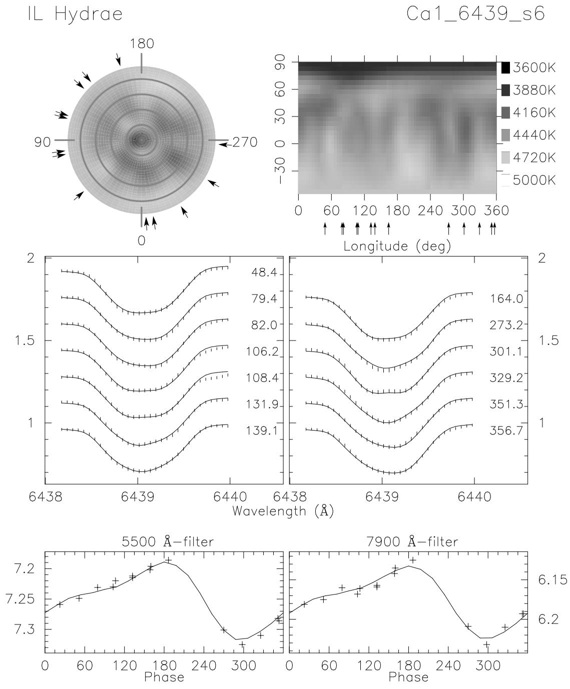

Figure 4.30.: As in figure 4.27 but for the KPNO 1997/98 data.

Differential rotation measurement using TEMPMAP

Since evidence for differential rotation was found in Weber & Strassmeier (1998) and in the section above using the NSO 1996 data, an attempt to recover the differential rotation using the “sheared-image” technique was done. Due to the availability of a data set with good signal/noise ratio (about 200) and good spectral resolution (38 000), this star is the only one in this sample except HK Lac where the differential rotation measurement for the time-series Doppler imaging using the NSO 1996 data can be confirmed by a second independent data set.

The data set, marked *KP5* in table 4.8, was taken during an observing run

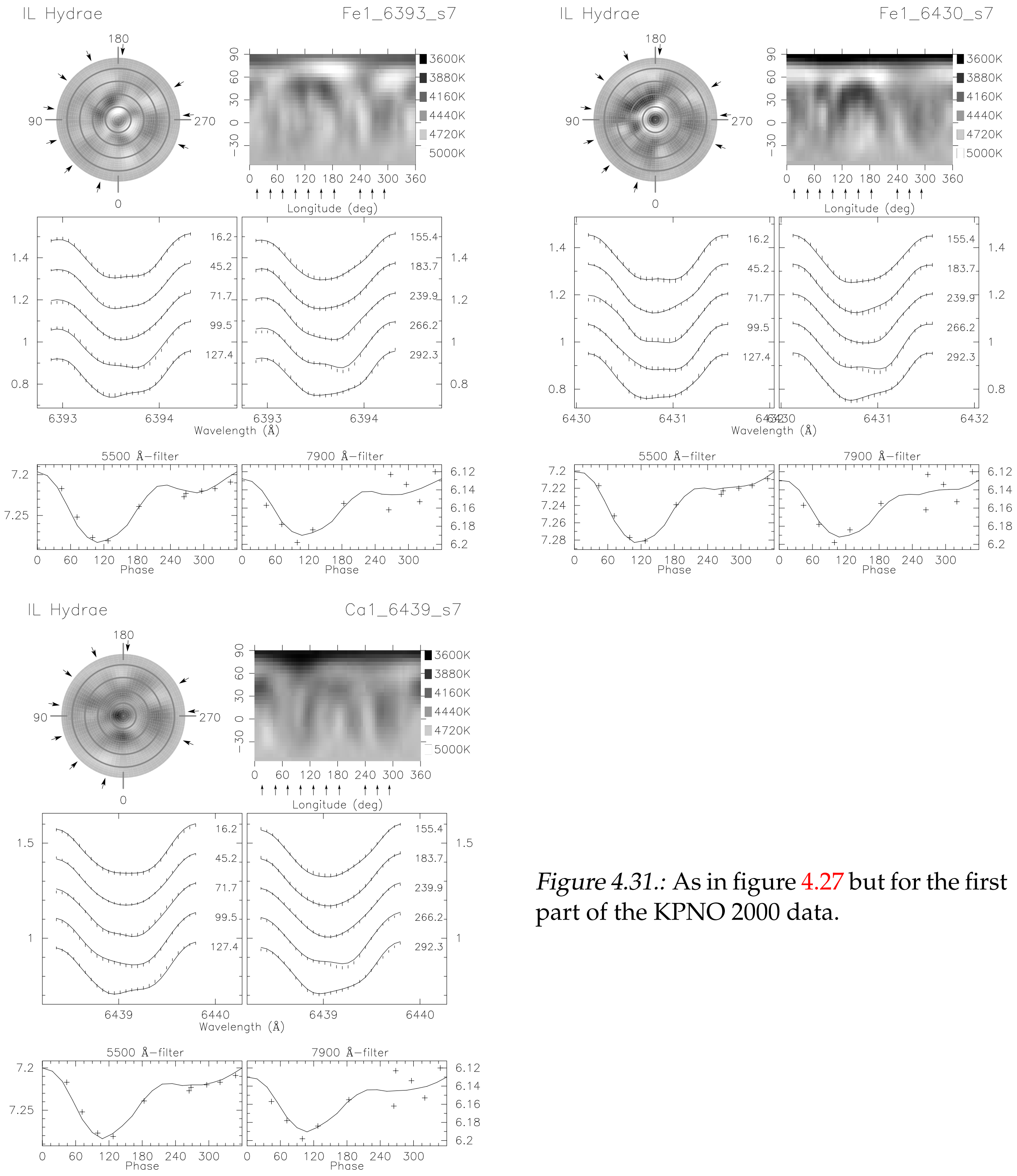

Figure 4.31.: As in figure 4.27 but for the first part of the KPNO 2000 data.

around New Years day 1998 (Washuettl 1998) and spans 20 days. The phase coverage is good besides a gap between 180° and 250° (due to a four day long bad weather period). Since this data is taken with the old camera at the Coude-feed telescope, no vignetting is present and therefore the Fe I 6393 line can also be used. As mentioned earlier, the Fe I 6411 suffers from pollution from the secondary's Fe I 6409 line additionally to the secondary's Fe I 6411 line, since the half-amplitude of the secondary's orbit corresponds to approximately the wavelength separation of these two lines. Thus only the Fe I 6393 line was taken in addition to the two mapping lines from the NSO run (Fe I 6430 & Ca I 6439).

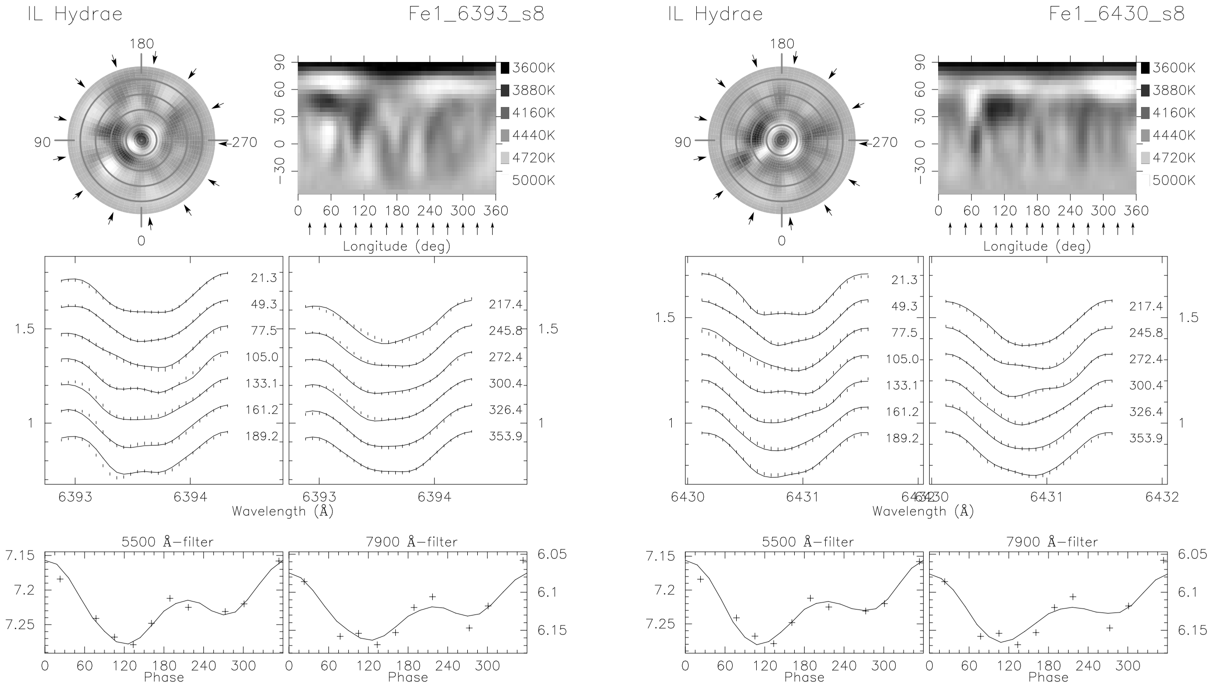

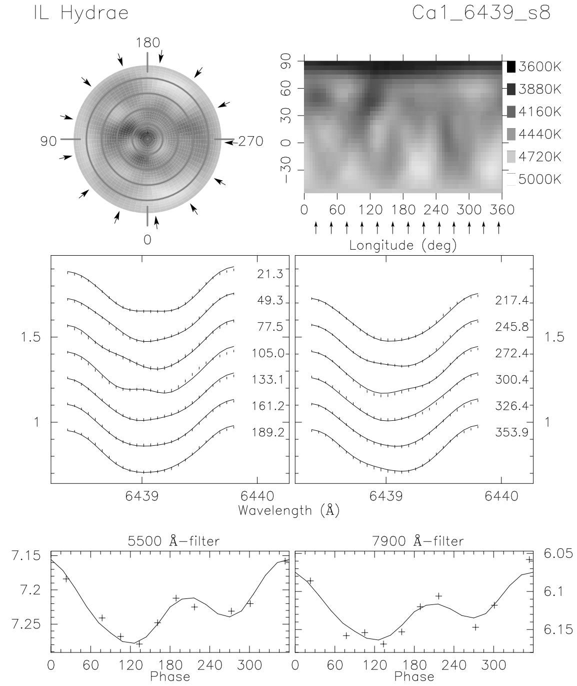

Figure 4.32.: As in figure 4.27 but for the second part of the KPNO 2000 data.

As described in appendix A.2, we calculated the χ^2 of Doppler images for a number of combinations of Ω_0 and Ω_1. The χ^2-maps resulting from these calculations are plotted in figure 4.36 for the three different spectral line regions and their average. Along with the maps, contour lines are shown to make it easier to identify the structure in the plots. The numerical values, which were measured off these χ^2-maps, are listed in the lower part of table 4.9.

We also reexamined the old data from 1994 (Weber & Strassmeier 1998) to confirm the original findings using the techniques presented here. It should be noted however, that the differential rotation measurement in Weber & Strass-

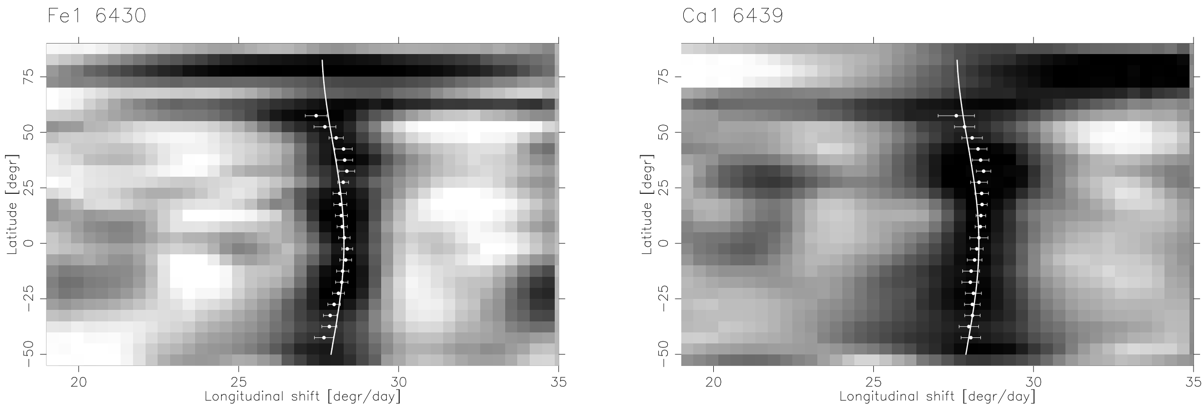

Figure 4.33.: Cross correlation images of IL Hya using the 1996 NSO data. The data were splitted into subsections with a length of about ten days and a time separation of three days. All pairs of images with 12 days (approximately one rotation period) time separation were cross correlated and averaged. Show at the **left** is the average cross correlation image for the Fe I 6430 line, at the **right** the average cross correlation image for the 6439 (right) line. The points are the measured cross-correlation peaks with their corresponding error, the solid line is an average fit. See text for details.

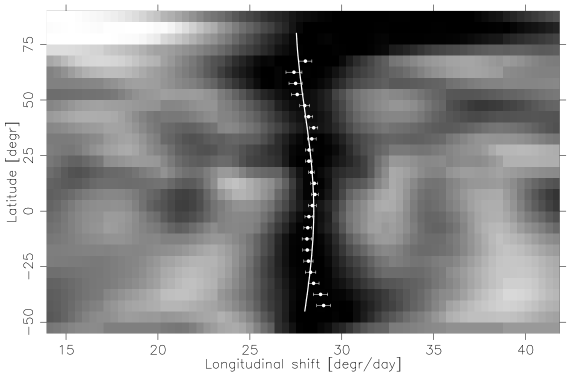

Figure 4.34.: Average cross correlation image of IL Hya. As in figure 4.33, but the correlation images from both spectral line regions. Again, the highest and lowest 15% pixels were rejected.

meier (1998) was based on two images with about one year time separation, while here we try to recover it during almost exactly one rotation period (the data span 14 days). This is also in contrast to the previous section about the KPNO 1997 data, which covers an about 50% longer timespan. Remarkably, as seen in figure 4.37, the results appears to be similar to the one for the 1997 data, but the signal is weaker. Since the instrument setup was the same and the signal of the data is comparable, the difference in time-coverage of the data set and therefore in image shear could have contributed to the degradation of this result. Summarizing, there is some evidence for solar-like differential rotation of the order of α=0.05. The center of gravity in the average image in figure 4.37 lies approximately at P_{equ}=12.8 and α=0.05, although the uncertainties are too high for a conclusive result.

Application of this technique to the combined NSO 1996 data set (figure 4.38) proved not to be successful. But since this dataset combines the low-resolution and the low-signal-to-noise handicap, this had to be expected.

The last available dataset for this technique is from the KPNO 2000 observing run. That consisted of two blocks with each 14 days, separated by another 14 days.

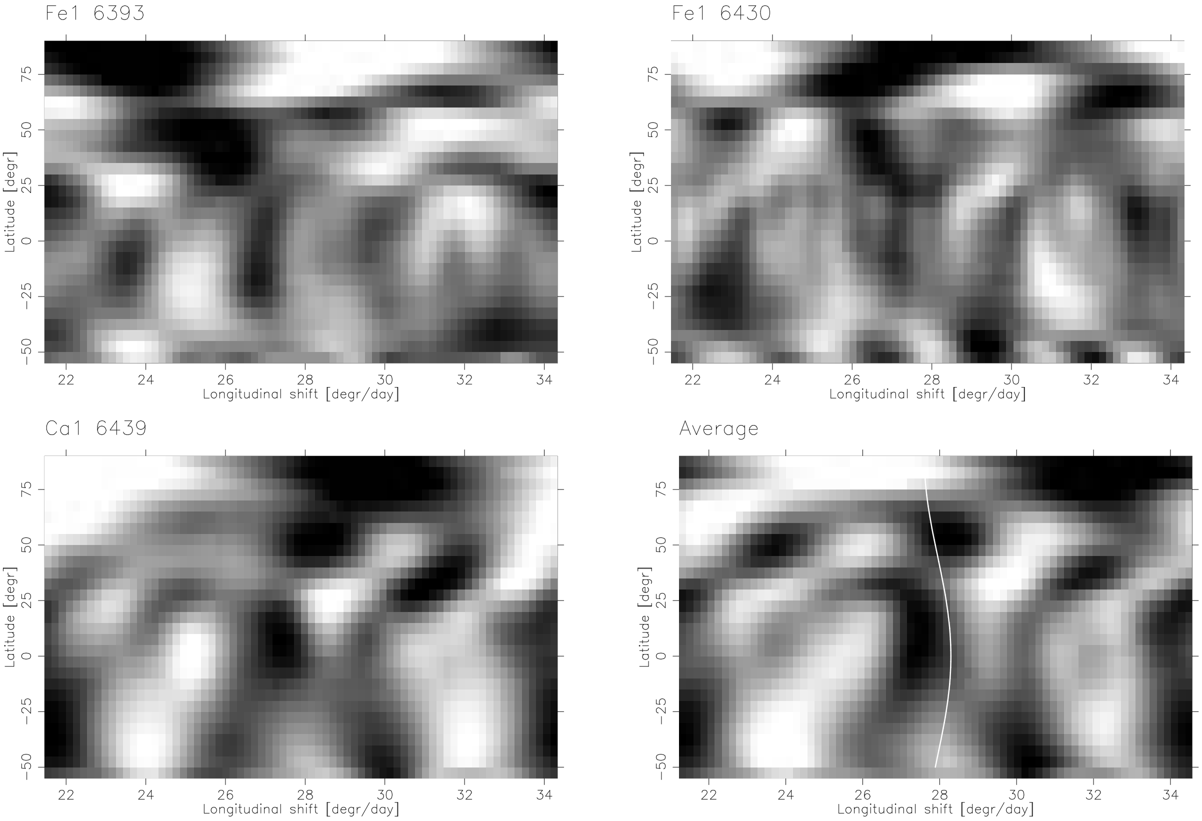

Figure 4.35.: Cross correlation images of IL Hya using the KPNO 2000 data. From left to right: the cross correlation image for the Fe I 6393, Fe I 6430 line, Ca I 6439 and the average of those three maps. The solid line in the average image is the differential rotation function derived in section 4.4.2. See text for details.

The main motivation for scheduling the observing run like this, was the ability to perform differential rotation measurement with the cross-correlation technique. The gap in the data increases the chance that some of the spots on the stellar surface are rearranged, but spot lifetimes of three stellar rotations are realistic, since the differential rotation signal in Weber & Strassmeier (1998) was derived from cross correlating two images about 30 rotations apart. The result is shown in figure 4.39, and as in the previous paragraphs, there is evidence for a peak in the χ^2 landscape at similar values as found in the 1997/98 data. However, the uncertainties are much higher, and the main conclusion to be drawn from this data is that α appears to be roughly between 0 and 0.1. Again, the reasons for the weakness of the detection can be either the difference in data quality (this data has a considerably lower spectral resolution) or real changes on the stellar surface during the observations.

Summary

The results of the differential rotation measurements derived in sections 4.4.2, section 4.4.2, and Weber & Strassmeier (1998) are listed in table 4.9. All measurements agree in a differential rotation in a solar-type direction (the pole lags behind the equator). The magnitude of the differential rotation parameter α in-

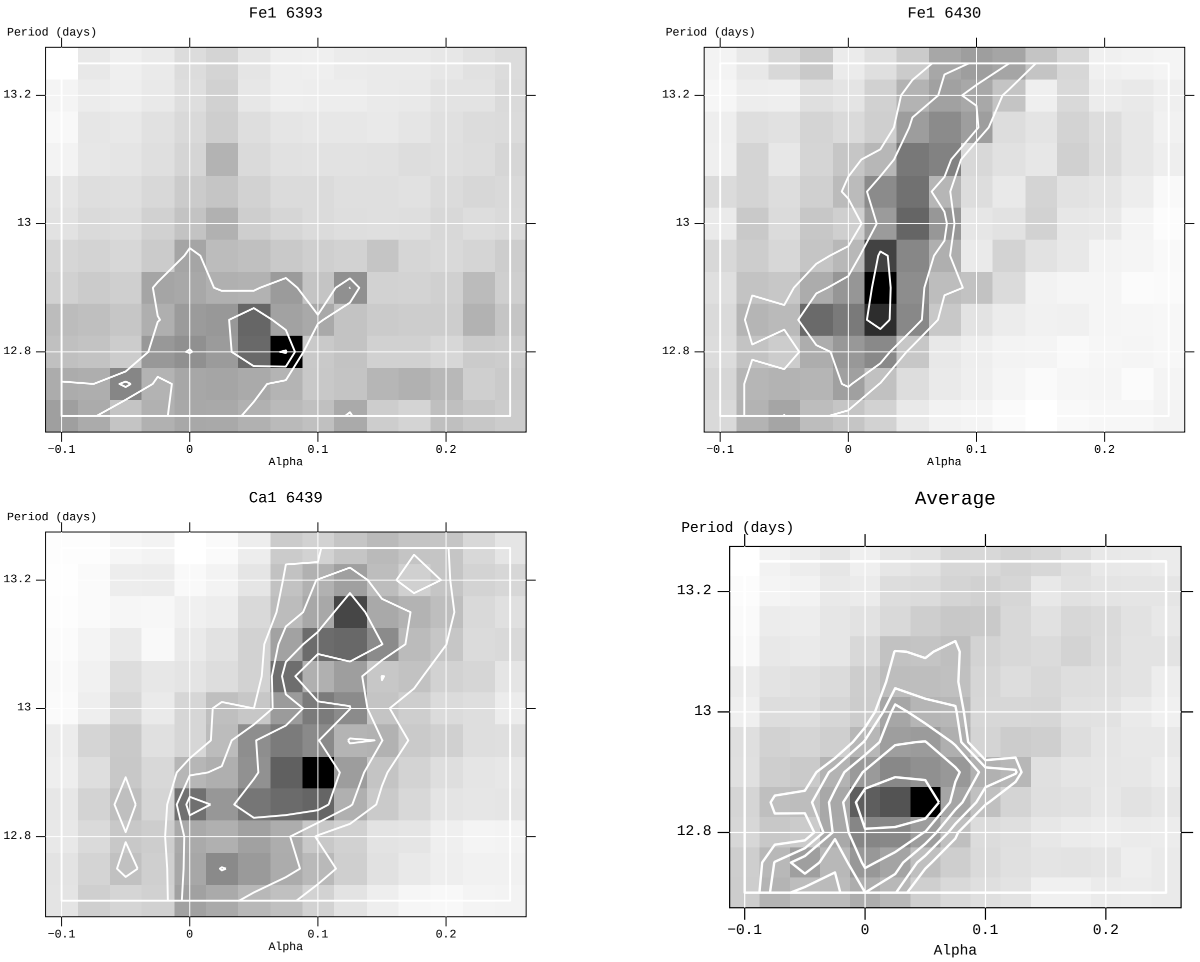

Figure 4.36.: χ^2 maps for IL Hya using the KPNO 1997 data set and the spectral lines Fe I 6393, Fe I 6430, Ca I 6439, and the average of those three. Darker values stand for better correlation, the solid white lines are contours of constant χ^2.

Table 4.9.: Differential rotation parameters for IL Hya: Values listed are for the cross-correlation (cc) analysis done by Weber & Strassmeier (1998), the average for the time series cross-correlations and for the combined data (see sect 4.4.2) and the result from the sheared-image analysis (see sect 4.4.2).

	Ω_0	Ω_1	α
cc 1994	28.149	−0.103	0.004
Average cc 1996	28.30±0.11	−0.70±0.77	0.025±0.027
Combined cc 1996	28.43±0.32	−0.69±0.80	0.024±0.028
Sheared 1997/98	28.02±0.11	−0.84±0.84	0.03±0.03

creases gradually from 1994 to 1998. But since all new detections are technically insignificant (just outside the 3σ limit), and the 1994 measurement is based on the comparison of two maps with a time separation of 30 stellar rotations, this can be seen as at most weak evidence towards variable differential rotation.

Concluding, the average differential rotation measurement from the various data sets and techniques presented here is

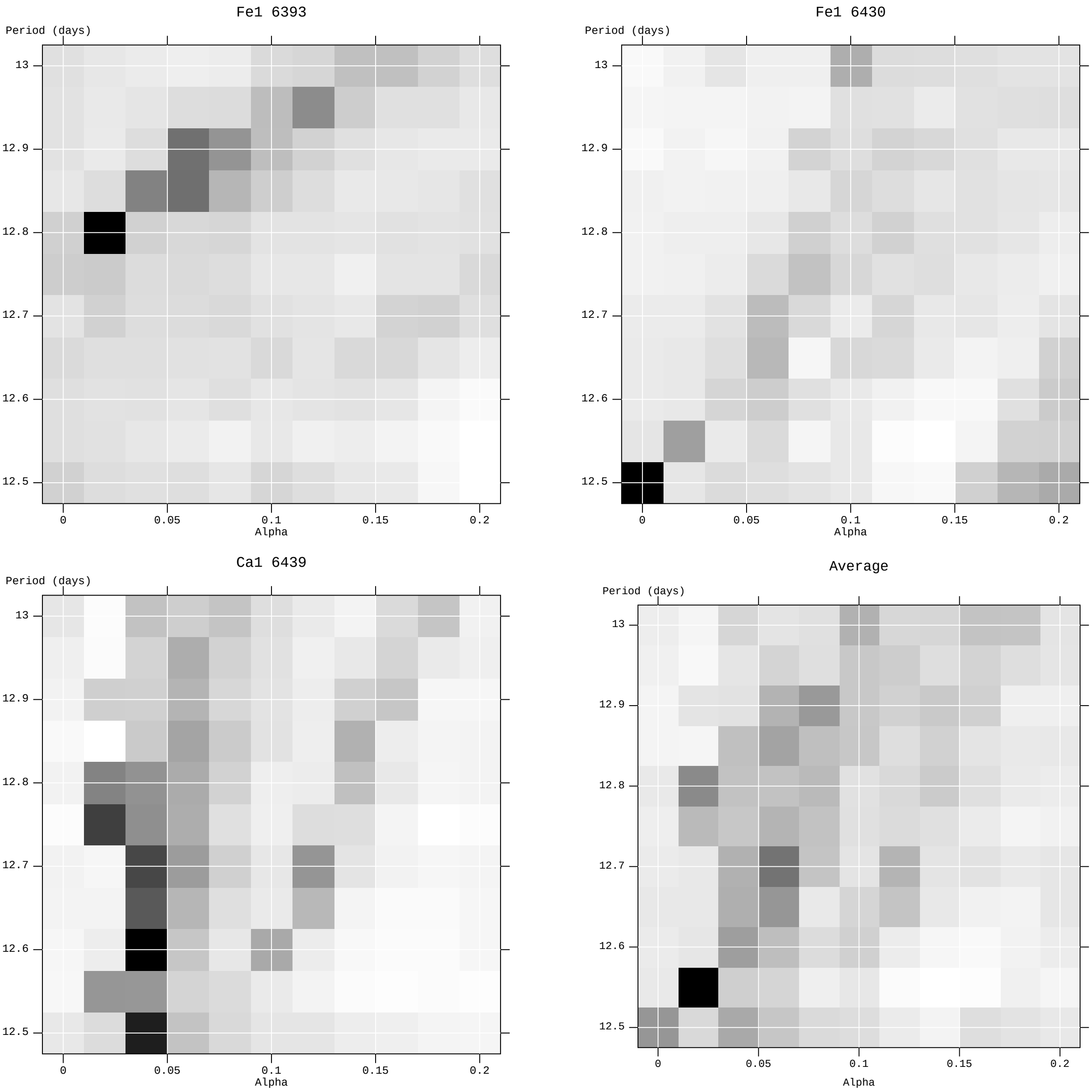

Figure 4.37.: As in figure 4.36, but using the KPNO 1994 data set.

$$\begin{aligned} \Omega(b) &= 28.2 \pm 0.12 - 0.74 \pm 0.46 \sin^2 b \\ \alpha &= 0.026 \pm 0.016. \end{aligned} \tag{4.2}$$

This about a factor of seven less than the sun in terms of α, or a factor of four in terms of laptime, since $1/\Omega_1 = P_{\text{equ}}/\alpha$.

Comparing the data quality of the various data sets with the quality of the results, it is becomes clear that for detection of differential rotation both, a high spectral resolution and a good signal to noise ratio are needed, along with a phase coverage that either spans two stellar rotations, or at least includes a phase overlap of approximately 50%.

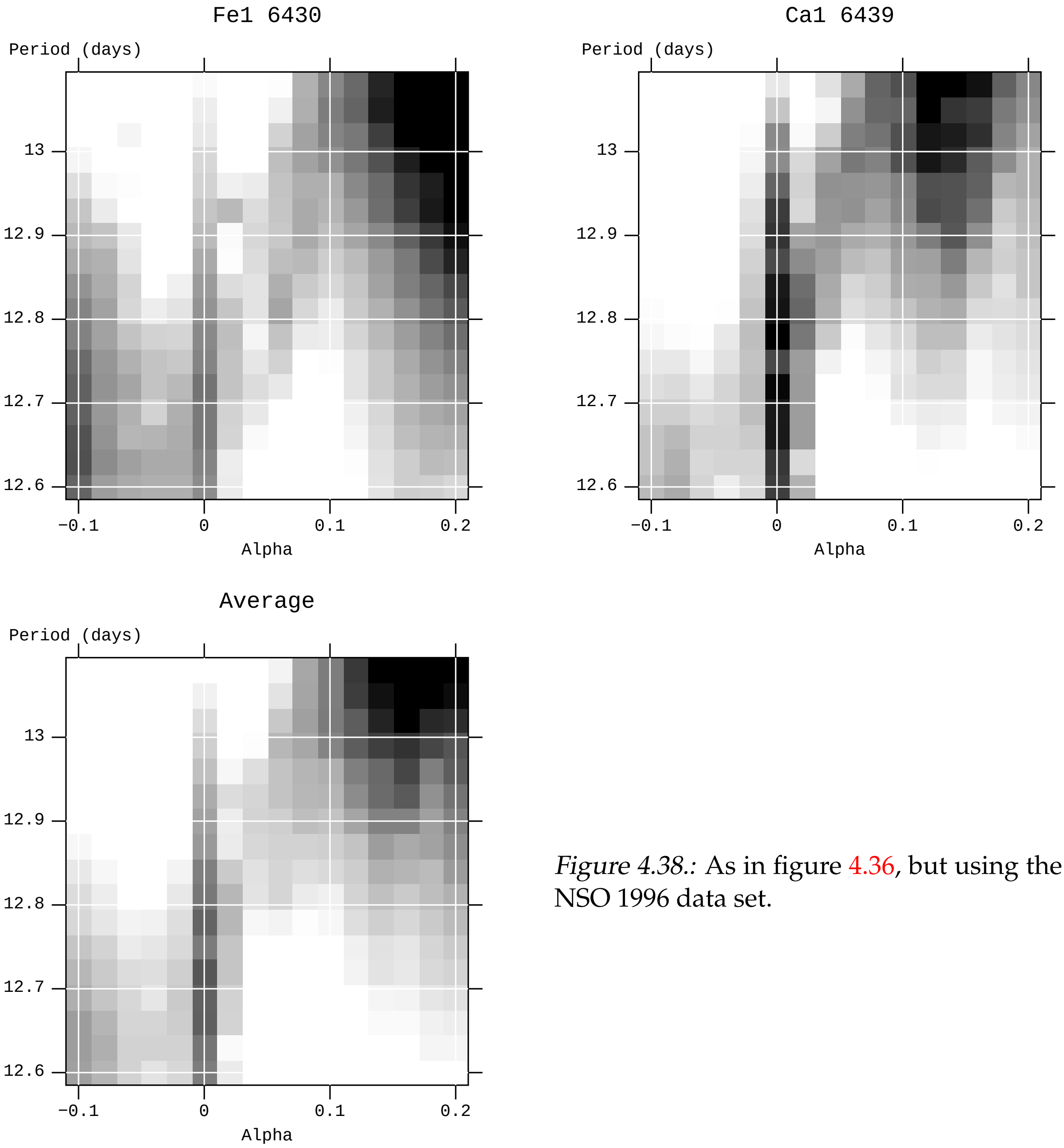

Figure 4.38.: As in figure 4.36, but using the NSO 1996 data set.

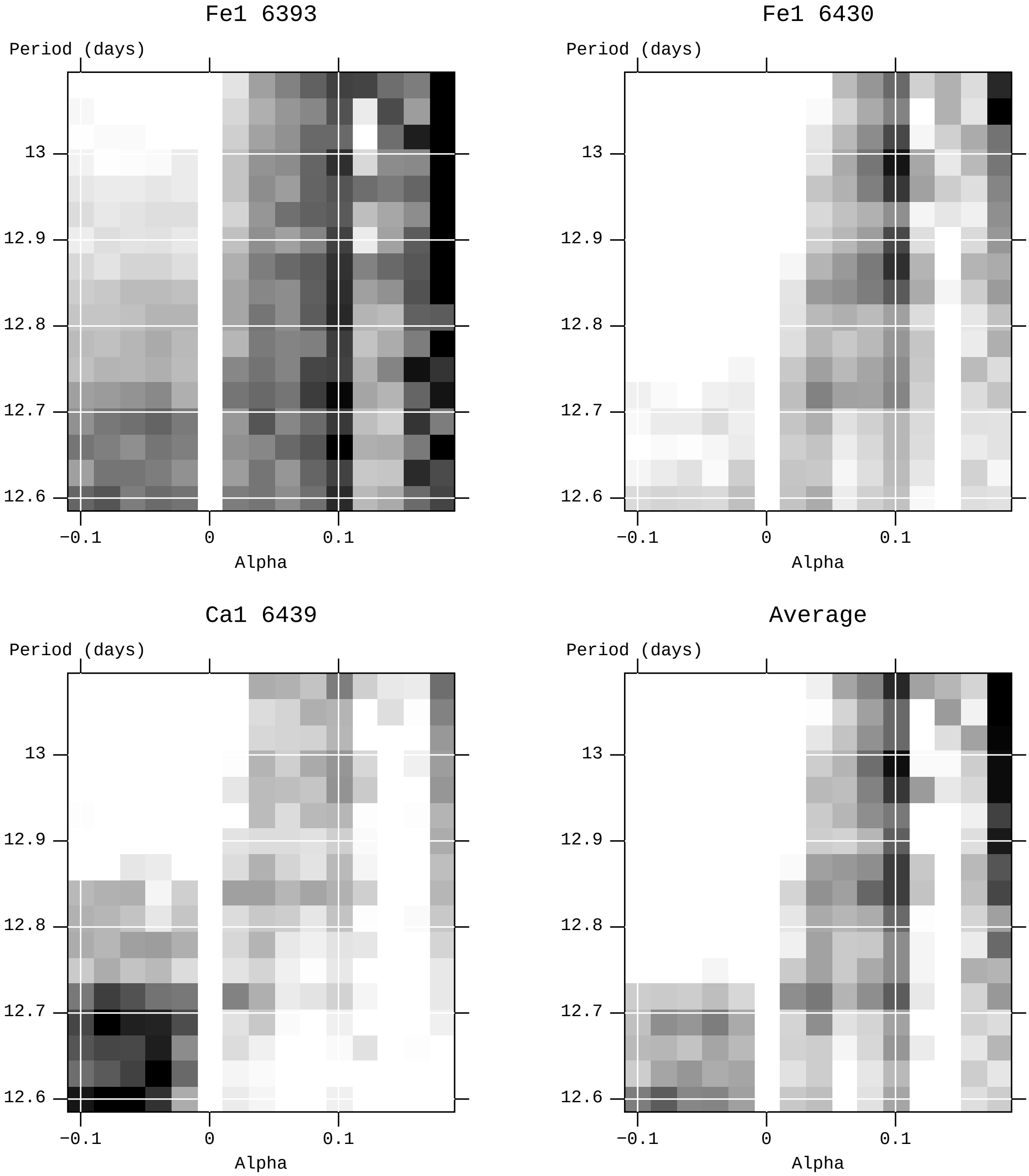

Figure 4.39.: As in figure 4.36, but using the KPNO 2000 data set.

4.5. II Peg

4.5.1. Introduction

II Peg (HD 224085, BD+27 4642), like most stars in the sample presented before, is a very active RS CVn binary star. It shows periodic lightcurve and color variations which are almost synchronized with the orbital rotation. These variations are interpreted as starspots rotating in and out of view. An extensive study about the photometric variability and its history is given in Rodonò et al. (2000).

Owing to its brightness (V=$5\overset{m}{.}5$, see table 4.10) and its fairly convenient rotation period, the star has been Doppler imaged several times already. Hatzes (1993) presented the first image, while Berdyugina et al. (1998a) presented nine Doppler images from 1992 to 1996. Six more images were presented in a later publication (Berdyugina et al. 1999a), where a period of switches between two active longitudes of about 9 years is derived from spot areas and positions measured from the Doppler images.

Huenemoerder et al. (1989) and Vogt (1981) made quantitative studies of TiO absorption bands and found that a large fraction of the surface (35-40%) must be covered with spots. O'Neal et al. (1998), also from TiO studies, conclude, that the spot filling factor on the surface is almost constant during 3/4 of a stellar rotation in late 1996, but that the spot temperature changes by about 200 K. A similar study, but using the OH 1.563μ line by O'Neal et al. (2001) comes to similar results, deriving starspot filling factors of 0.35 to 0.5 during part of one stellar rotation in 1998.

Table 4.10.: Stellar parameters of II Peg.

Parameter	Value
Spectral type	K2-3 IV
$\log g$	3.0 ± 0.2
T_{eff}	4600 ± 100 K
V	7.51 mag
$(B-V)$	1.007 mag
$(V-I)$	0.98 mag
$v \sin i$	23.5 ± 1 km s^{-1}
Inclination i	$60^\circ \pm 15^\circ$
Distance d	42.3 ± 1.6 pc
Radius R	$3.6^{3.23}_{4.41}$ R$_\odot$
Rotation period P_{orb}	6.724333 ± 0.000010 days
Equatorial velocity v_{equ}	27.1 ± 4.3 km s^{-1}
Microturbulence ξ	2.0 km s^{-1}
Macroturbulence $\zeta_{\text{R}} = \zeta_{\text{T}}$	3.5 km s^{-1}
$\log[Ca]$ abundance	0.9 dex below solar
$\log[Fe]$ abundance	0.8 dex below solar

4.5.2. Observations

All observations presented her are from the NSO 1996 observing run. The observations cover about 10 stellar rotations. To achieve a minimum amount of phase coverage per Doppler image, the observations were subdivided into 5 blocks (see table 4.11) with 8–10 observations per block. Due to vignetting and CCD characteristics, only two spectral lines were usable, namely Fe I 6430 and Ca I 6439, as is the case for most of the stars observed at that observing run. The average signal to noise ratio achieved was 100, which is barely enough for Doppler imaging at these low resolutions. The observations were phased with the orbital period $P_{\rm orb} = 6.724333 \pm 0.00001$ and $T_{\rm conj} = 2449582.9268 \pm 0.0055$ (Berdyugina et al. 1998b). The distribution of observed phases with the date observed is plotted in figure 4.40.

Table 4.11.: Spectroscopic log and radial velocity data ($v_{\rm rad}$).

HJD (24+)	Phase (°)	$v_{\rm rad}$ (km s^{-1})	$\sigma_{\rm rad}$	S/N	Rotational cycle	Telescope
2450391.806	104.9	-56.9	1.9	80	map 1	NSO
2450392.700	152.7	-38.7	2.7	100	map 1	NSO
2450393.772	210.1	1.3	2.1	110	map 1	NSO
2450394.799	265.1	16.9	1.8	120	map 1	NSO
2450395.585	307.2	5.5	2.1	120	map 1	NSO
2450396.671	5.4	-25.4	1.9	110	map 1	NSO
2450398.613	109.3	-62.5	1.8	100	-	NSO
2450399.816	173.7	-26.5	1.8	120	map 1	NSO
2450400.654	218.6	1.4	1.8	110	map 1	NSO
2450401.655	272.2	17.8	4.7	40	-	NSO
2450404.668	73.5	-60.5	2.0	120	map 1	NSO
2450405.641	125.6	-52.8	2.0	120	map 2	NSO
2450406.648	179.5	-21.6	1.9	110	map 2	NSO
2450408.647	286.5	16.4	1.8	110	map 2	NSO
2450409.640	339.7	-11.5	1.7	110	map 2	NSO
2450410.635	32.9	-42.9	2.1	110	map 2	NSO
2450411.643	86.9	-59.9	1.7	110	map 2	NSO
2450412.635	140.0	-46.1	1.6	120	map 2	NSO
2450413.633	193.4	-13.0	1.8	110	map 2	NSO
2450414.614	246.0	12.1	1.5	120	map 3	NSO
2450415.638	300.8	10.8	1.6	110	map 3	NSO
2450416.647	354.8	-20.7	1.6	110	map 3	NSO
2450417.747	53.7	-51.4	1.7	110	map 3	NSO
2450418.792	109.7	-58.8	1.9	110	map 3	NSO
2450419.621	154.0	-37.1	1.8	110	map 3	NSO
2450421.718	266.3	17.3	1.6	110	map 3	NSO
2450422.629	315.0	5.0	1.8	110	map 3	NSO
2450423.636	9.0	-29.2	2.2	100	map 3	NSO
2450424.727	67.4	-58.5	2.0	120	map 3	NSO

Table 4.11.: Spectroscopic log of II Peg (continued)

HJD (24+)	Phase (°)	$v_{\rm rad}$ (km s^{-1})	$\sigma_{\rm rad}$	S/N	Rotational cycle	Telescope
2450425.696	119.2	-53.9	2.1	130	map 4	NSO
2450426.714	173.7	-24.4	2.2	120	map 4	NSO
2450429.685	332.8	-4.9	1.8	110	map 4	NSO
2450430.705	27.4	-38.8	1.9	120	map 4	NSO
2450431.590	74.8	-59.7	2.0	110	map 4	NSO
2450432.625	130.2	-50.7	1.9	110	map 4	NSO
2450433.618	183.4	-19.4	2.0	100	map 4	NSO
2450434.626	237.3	8.9	1.6	80	-	NSO
2450435.616	290.3	13.1	1.9	100	map 4	NSO
2450436.675	347.1	-15.6	2.0	110	map 5	NSO
2450437.583	35.6	-44.1	1.9	100	map 5	NSO
2450438.683	94.5	-59.2	2.0	110	map 5	NSO
2450439.722	150.2	-44.2	2.1	100	map 5	NSO
2450441.692	255.7	15.0	1.8	120	map 5	NSO
2450445.621	106.0	-58.0	2.0	110	map 5	NSO
2450446.619	159.4	-33.3	2.0	110	map 5	NSO
2450450.708	18.3	-34.8	2.0	110	map 5	NSO
2450451.651	68.8	-57.1	2.4	110	map 5	NSO
2450457.725	34.0	-44.8	1.9	100	map 5	NSO

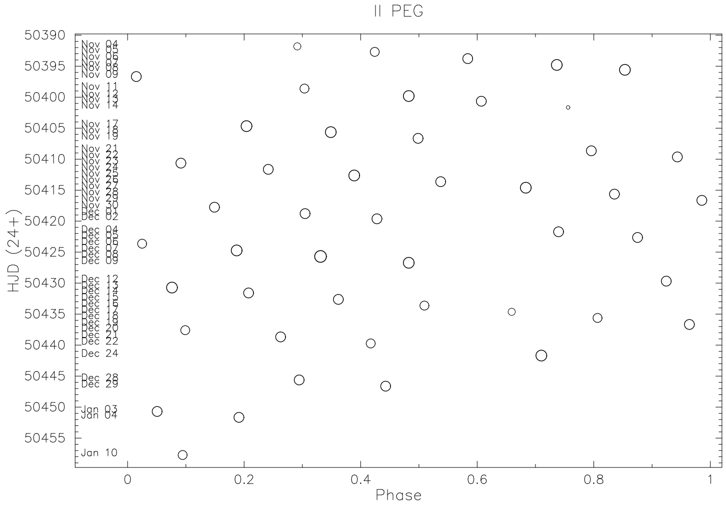

Figure 4.40.: Distribution of the rotational phases of II Peg versus date. The sizes of the circles are proportional to the S/N ratio of the spectra, where the average value is about 100:1.

4.5.3. Time-series Doppler imaging

The most important input parameters used for Doppler imaging are listed in table 4.10. Most of them are taken from the very detailed analysis of the physical parameters by Berdyugina et al. (1998b). The individual Doppler images for each of the two spectral line regions Fe I 6430 and Ca I 6439 are displayed in figures 4.41 to 4.45. Since the number of phases used for each individual Doppler image is very

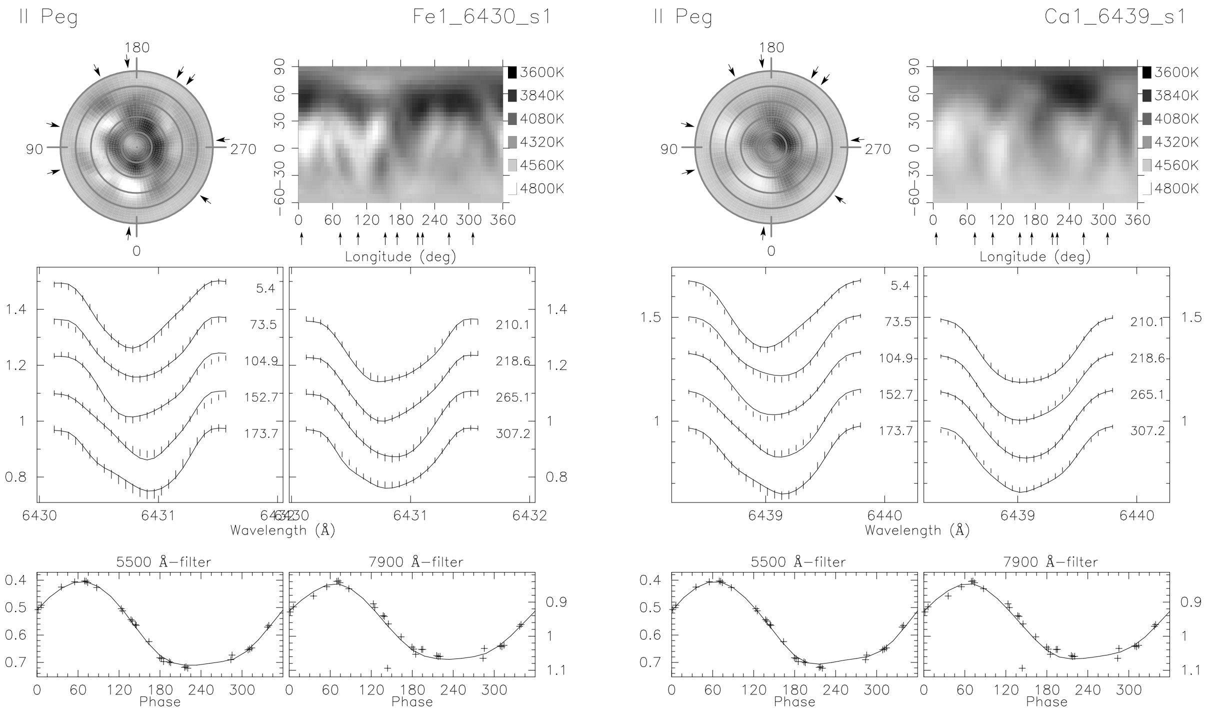

Figure 4.41.: Individual Doppler images from the first data subset of II Peg. The map from the Fe I 6430 line is shown at the left, the map from Ca I 6439 at the right. Temperature maps from the individual lines are plotted in a pole-on view and a pseudo-Mercator (top row) projection where the arrows indicate the spectroscopic phase coverage. The observed and computed line profiles are shown in the middle row, and observed and computed V and I_C-lightcurves in the bottom row. The pluses and the bars are the observations and the full lines are the fits. The size of the bars correspond to a $\pm 1\,\sigma$ error per data point.

low, many features of the resulting maps are dominated by deformations visible in one single spectrum only. We nevertheless used this subdivision to take advantage of the time resolution of our observations. The shortcomings of this approach are overcome by averaging many subsets in section 4.5.3.

Comparing these images with the results from Berdyugina et al. (1998a) show a high degree of agreement. The maps are dominated by two high latitude active regions at a latitude of approximately 55° and longitudes of 20° and 250°, respectively. Comparing the five average maps for the respective data blocks (figure 4.46) with the total average map (figure 4.47) one finds a lot of similarities. The dominating feature is always a big spot at about $\ell \approx 250°$, one spot is at lower latitudes a little right of that ($\ell \approx 320°$, $b \approx 30°$), and a series of weaker feature (sometimes merged to one) extends from 0° to $\ell \approx 120°$. But it is obvious that the small differences between these maps are dominated by noise and not by real changes on the stellar surface. In the following chapter, the spot evolution is described in more detail. It becomes clear that there is good evidence for systematic changes on the stellar surface, but that the comparison of two consecutive images does not reveal its true nature.

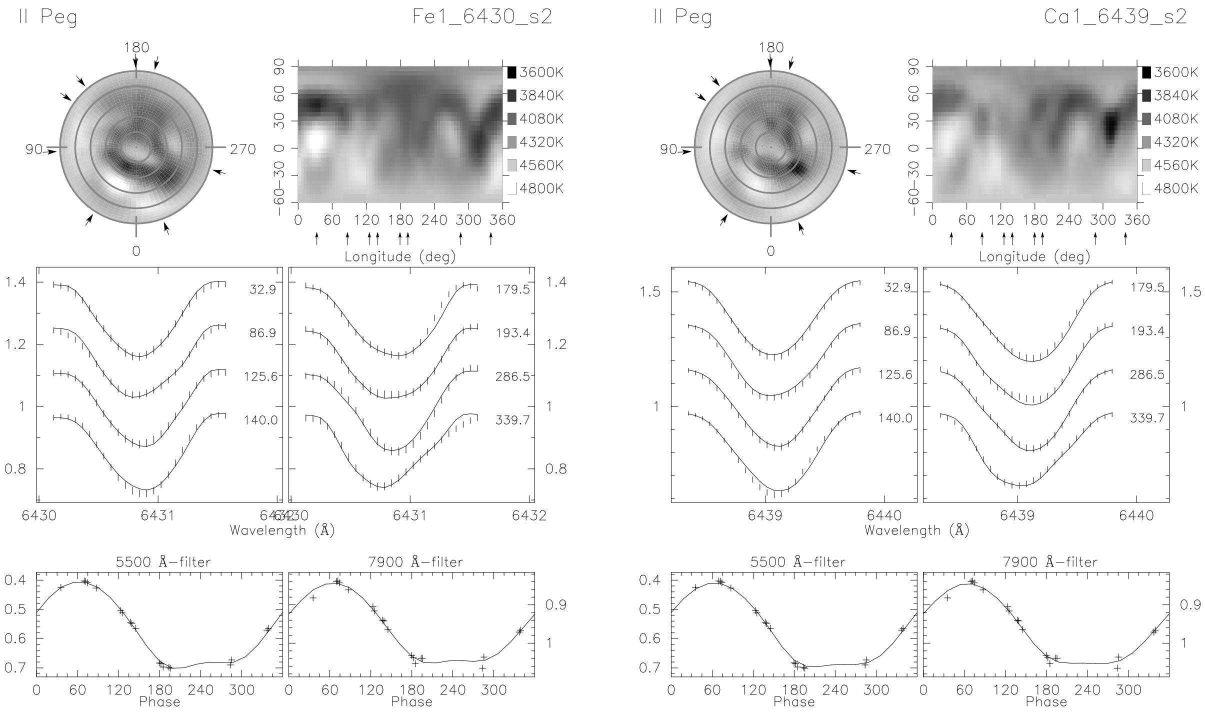

Figure 4.42.: As in figure 4.41 but for the second subset.

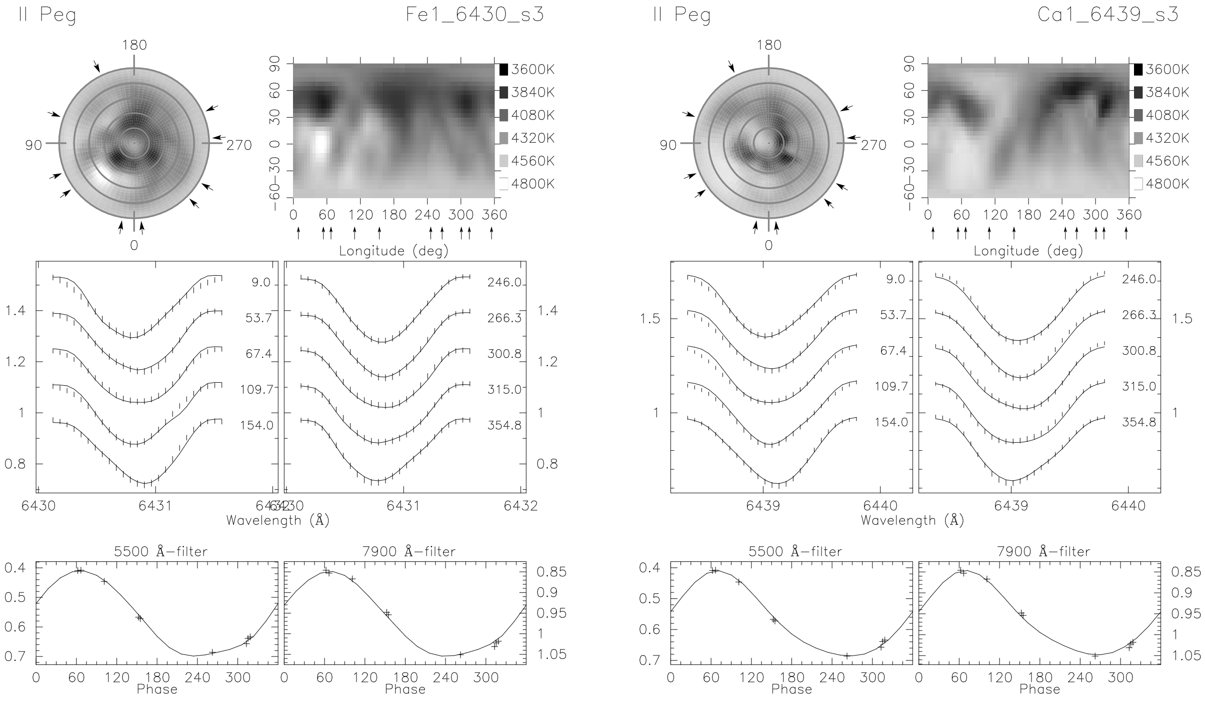

Figure 4.43.: As in figure 4.41 but for the third subset.

Cross-correlation analysis

Variation of the stellar surface that happen on timescale of approximately one stellar rotation (i.e. differential rotation, see appendix A.2) can be analyzed using the cross-correlation technique. Two Doppler images are compared by cross-

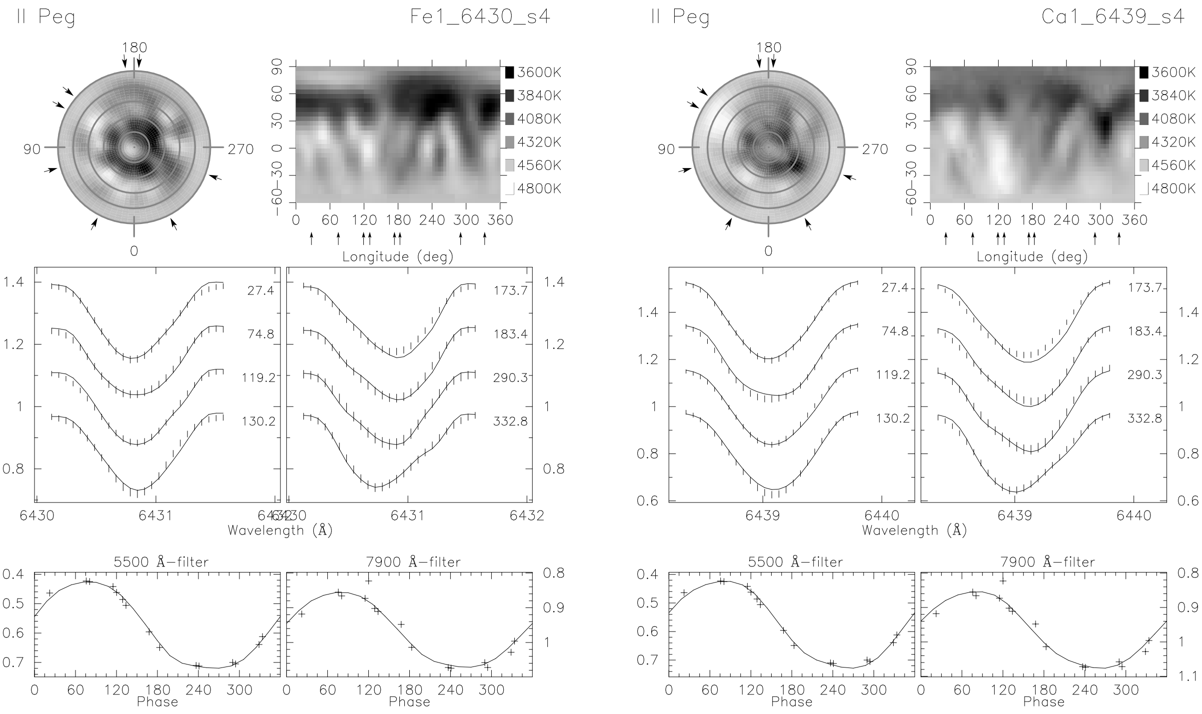

Figure 4.44.: As in figure 4.41 but for the fourth subset.

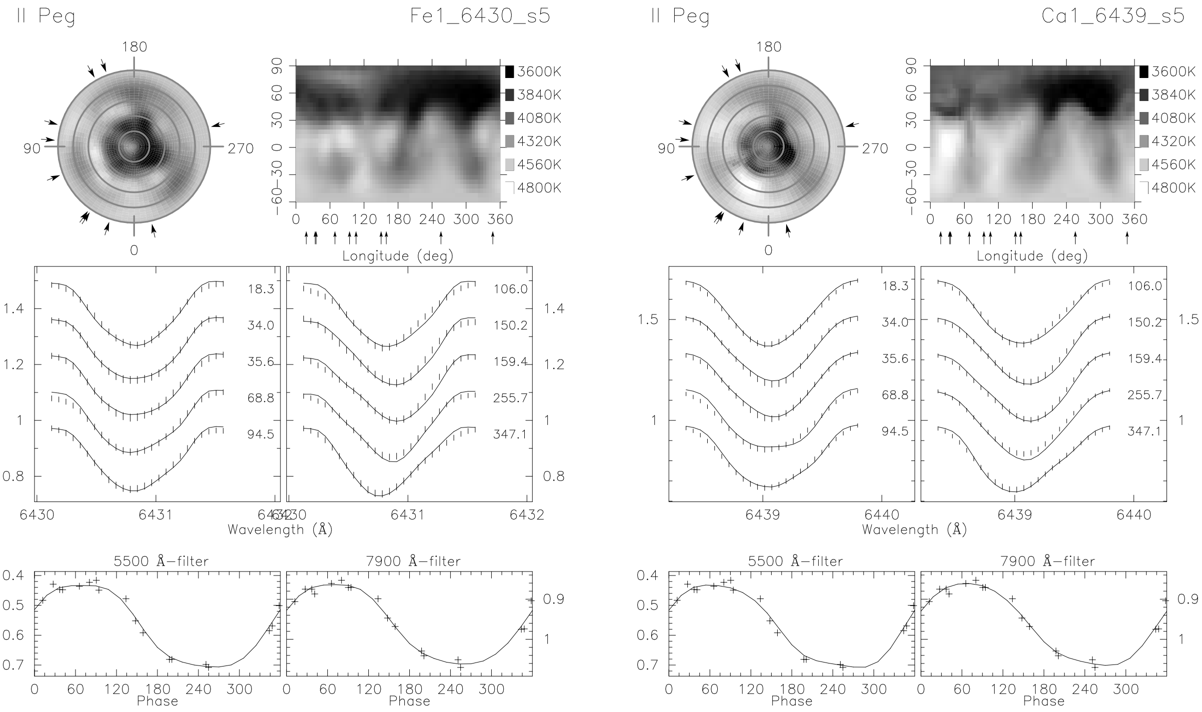

Figure 4.45.: As in figure 4.41 but for the fifth subset.

correlating the longitudinal temperature distribution for each latitude strip (5° in our case). The result is one cross correlation function for each latitude, which is usually displayed as a two-dimensional map. Figure 4.48 shows two example cross correlation images for II Peg. The cross-correlation derived from two consec-

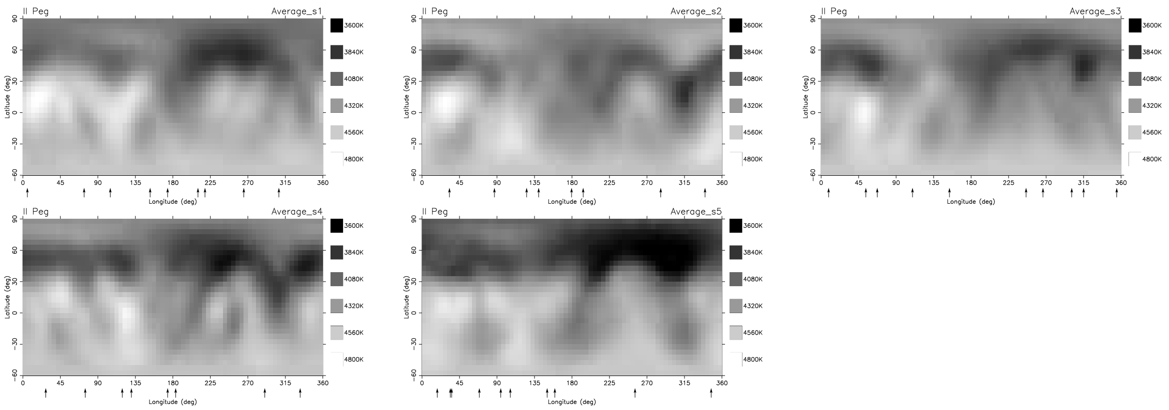

Figure 4.46.: Average Doppler images from both spectral lines for each of the five subsets.

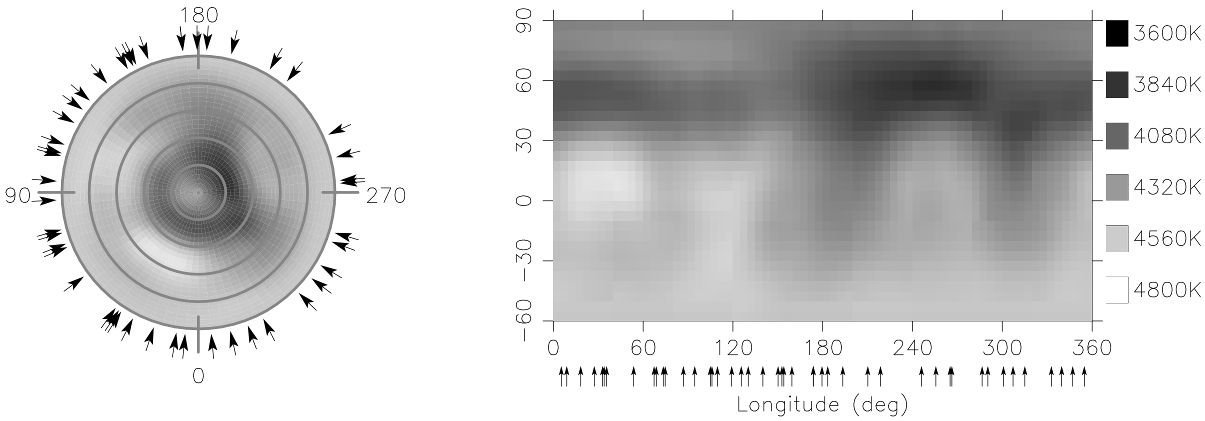

Figure 4.47.: Average Doppler image of II Peg. This is the average from both spectral regions for all of the five subsets.

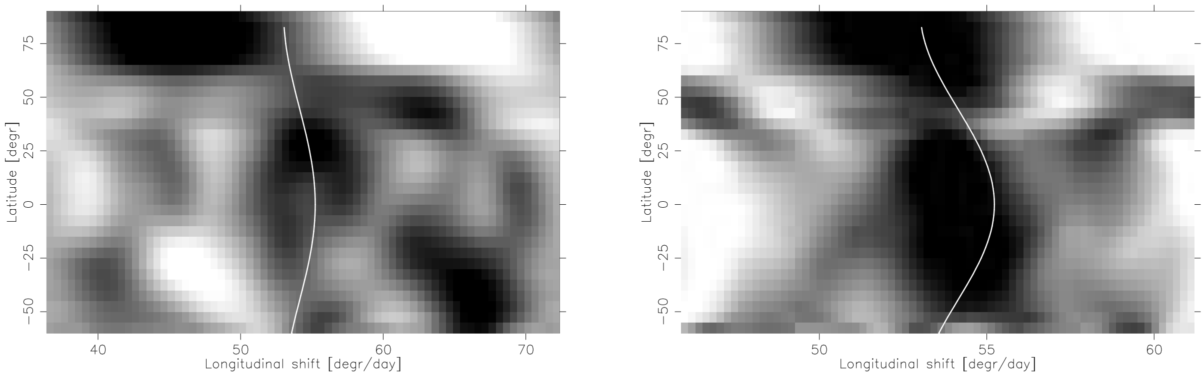

Figure 4.48.: Example cross correlation images of II Peg: **Left.** Cross-correlation of the average Doppler images for the first two sets. **Right.** Cross-correlation of the combination of the first two sets with a combination of sets three and four. The solid line marks the differential rotation curve derived from the average cross-correlation images.

utive Doppler images (figure 4.48, left) shows very little systematic changes. The solid line plotted on top of the cross-correlation maps corresponds to a differential rotation law derived later. The other plot (figure 4.48, right) is derived by merging the first and second two data blocks to again consecutive, but now larger datasets with a larger average time separation. Here, systematic effects start to appear in the cross-correlation image. The overplotted line seems to be in agreement with the image now. But it is clear from these to examples, that it is difficult to derive a reliable differential rotation law by cross-correlating the available Doppler images.

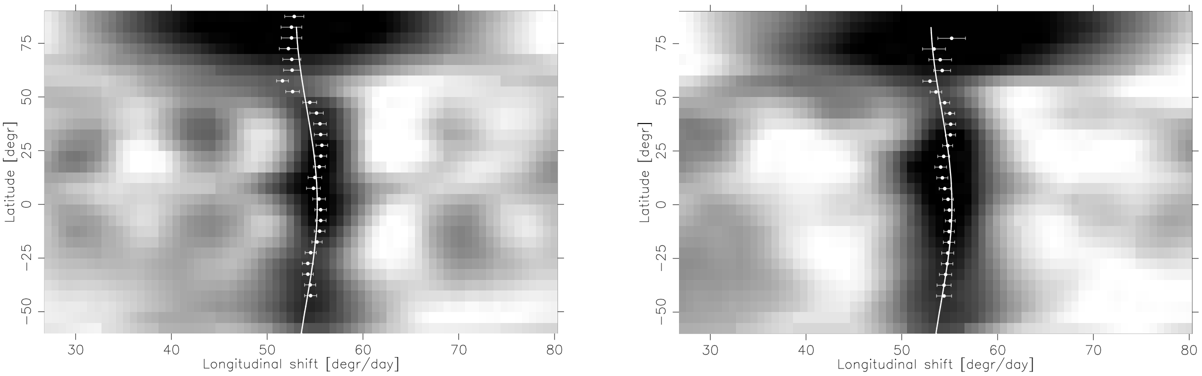
a. Fe I 6430

b. Ca I 6439

c. Average

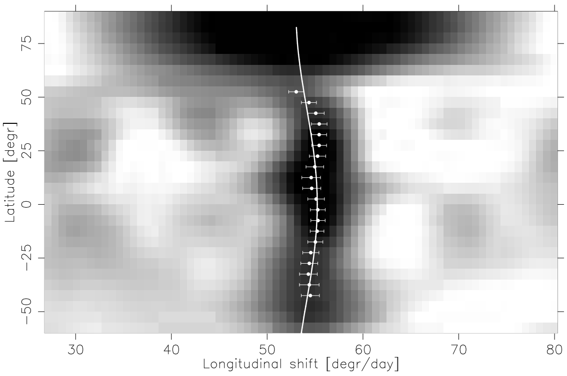

Figure 4.49.: Average cross correlation images for Fe I 6430 (**left**), and Ca I 6439 (**right**) spectral line regions. All data was divided up into ten days long sections, each in average two days apart from the last. Each pair of these 27 images that has a time difference of about one period was cross correlated, and the 25 cross-correlations obtained that way averaged (see text).

To overcome these problems, the data are subdivided into 26 subsets which span ten days each and are separated from each other by two days. We then select those subsets which are separated from each other by approximately one stellar rotation (namely subset one & subset four, subset two & subset five, etc.) and compute their cross-correlation image. Each of these images is corrected for small differences in time separation. Finally all resulting cross-correlation images are averaged using a routine that reject the highest and lowest three values (≈15%) for each pixel. The resulting average cross-correlation images for each of the two spectral regions and for the combination of both are shown in figure 4.49.

The results for the two individual lines and for the combination these are encouragingly similar. The numerical results of the fit of a solar like differential rotation law to the cross-correlation images from figure 4.49 are summarized in table 4.12. In all cross-correlation plots the average cross-correlation fit from that table is shown along with the measurements of the cross-correlation peaks per latitude bin. Although the fit matches the measurements well, it seems to oversimplify the spot evolution scheme. If the cross-correlation images have this horizontal-“W”-shaped form because of the crosstalk between the neighboring latitudes (a shortcoming of the Doppler imaging technique which results in root-of-the-tooth shaped spots), or because there really are two different surface shear mechanism at work is not clear. But it could be possible that a surface differential rotation is superimposed by migrating active longitudes.

Differential rotation measurement using TEMPMAP

As demonstrated in the previous chapters, it is also possible to use differential rotation inside of TEMPMAP instead of the standard rigid rotation model. This influences both, the shape of the integrated line profiles and the positions of the spots with time. Since all the data available for II Peg is the NSO 1996 data, no significant results are expected here due to the shortcomings of the data. A good reference for the influence of data quality is IL Hya (chapter 4.4), because of the wealth of different instruments used for collecting its spectroscopic observations.

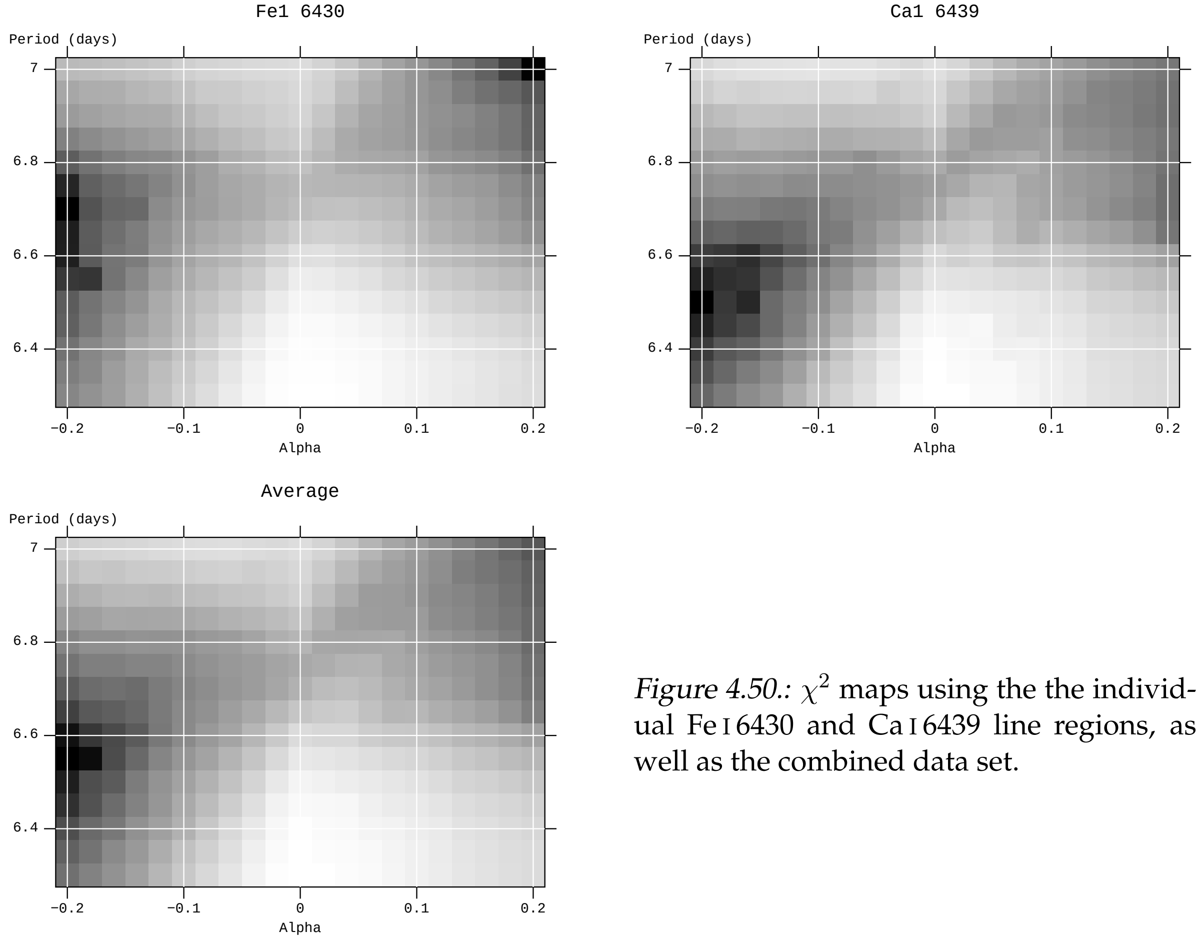

Figure 4.50.: χ^2 maps using the the individual Fe I 6430 and Ca I 6439 line regions, as well as the combined data set.

All spectra were combined into one dataset and a global parameter search was done for each of the two spectral line regions. The results together with the combined image are shown in figure 4.50. Due to the limited spectral resolution and signal to noise ratio, no minimum could be detected. The image just reveals the fact, that there is a linear relation between α and P_{equ} in case of a pronounced spot-latitude. Surprisingly, the slope of that relation is very small, compatible to a single spot at about 30° which is a lot smaller than the actual latitude at which most spots are visible.

As outlined in the previous section, it is possible that the pattern of the surface shear is more complicated than a simple $\sin^2$-law. Unfortunately, the quality of the data does not really allow us to rule out the simple solar-like differential rotation law.

Summary

Table 4.12.: Differential rotation parameters derived from cross-correlation. Rows Fe I 6430 and Ca I 6439 list the average results for the respective spectral line regions with 3σ errors, *Average* values are the average results from both of these regions, and *Combination* is a fit to the combination of all cross-correlation images with the formal error of the fit.

	Ω_0	Ω_1	α
Fe I 6430	55.65±0.11	−3.40±0.62	0.061±0.011
Ca I 6439	54.81±0.13	−1.02±1.64	0.019±0.030
Average	55.23±1.37	−2.21±4.06	0.040±0.074
Combination	54.86±0.32	−1.14±0.80	0.021±0.015

Even though the exact quantity of the differential rotation determined here is not very accurate, the direction and the order of magnitude is well established. The direction is in the same as in the solar case, everything else would have been a big surprise, since no anti-solar differential rotation has been found yet for a star with a roughly similar evolutionary stage as the sun. Rodonò et al. (2000) finds a (relative) differential rotation of α=0.015 compatible with their photometric results. Just using the information from the active longitudes however, the differential rotation would decrease to 0.00023. The value α=0.0045 derived by Henry et al. (1995b), again using photometric data to track long-lived features, lies in the middle between the former two measurements. All of these measurements are compatible with the value of α=0.020 to 0.06 we derive from applying the cross-correlation technique to our NSO 1996 data.

4.6. HK Lac

4.6.1. Introduction

HK Lac (HD 209813, BD+46 3572) is a well observed star that has been photometrically monitored since the detection of its lightcurve variability. It's long term photometric variability is examined in (Oláh et al. 2000), were two possible cycle periods (6.8 and 13 years) are detected. A more thorough description of the photometric history of HK Lac can be found in (Oláh et al. 1997) and (Olah et al. 1985).

Physical parameters

Table 4.13.: Stellar parameters of HK Lac.

Parameter	Value
Spectral type	K0 III
$\log g$	2.5 ± 0.5
T_{eff}	4800 ± 100 K
V_{max}	6.65 mag
$(B - V)$	0.936 ± 0.03 mag
$(V - I)_C$	1.006 ± 0.03 mag
$v \sin i$	24 ± 1km s^{-1}
Inclination i	75° $10\pm$ $^\circ$
Distance d	151 ± 14 pc
Radius R	12 ± 1 R$_\odot$
Rotation period P_{orb}	24.42868 ± 0.00023 days
Microturbulence ξ	2.0 km s^{-1}
Macroturbulence $\zeta_{\mathrm{R}} = \zeta_{\mathrm{T}}$	4.0 km s^{-1}
$\log[Ca]$ abundance	1.1 dex below solar
$\log[Fe]$ abundance	1.0 dex below solar

Differential photometric properties are taken from (Oláh et al. 1997), absolute photometric magnitudes of the reference star HD 210731 from (Hauck & Mermilliod 1990). We adopted 4800 K Oláh et al. (1997) as effective temperature of the unspotted photosphere. An inclination of 75°, somewhat larger than the value estimated by (Stawikowski 1994), is chosen. Comparing the minimal radius derived from the rotation period and the equatorial rotational velocity with the radius derived from the Hipparcos distance and the photometric data, one gets disagreeing results. To keep the disagreement as small as possible, we chose to use an inclination of 75°, which is just small enough not to be form an eclipsing binary. Also, the results from Doppler imaging (see section 4.6.3) suggest a value above 70° for the inclination angle. The stellar parameters are collected in table 4.13.

4.6.2. Observations

Most of the spectroscopic observations (marked *NSO* in column *Telescope* of table 4.14) were obtained at the National Solar Observatory (NSO) with the McMath-Pierce main telescope between October 31, 1996 and January 8, 1997. The

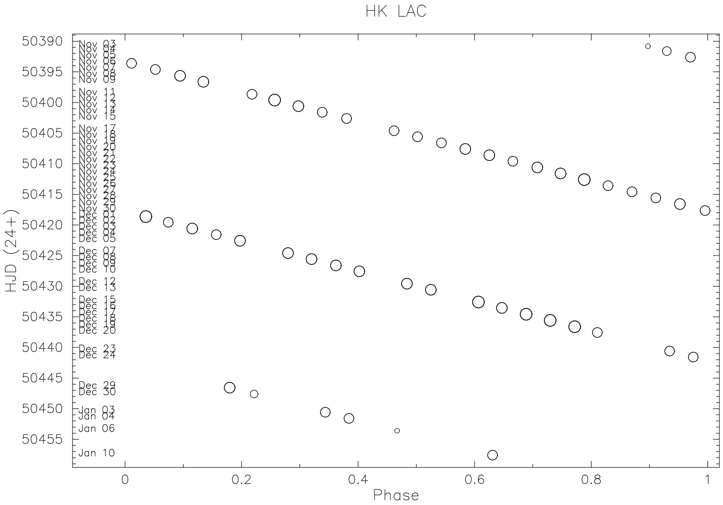

Figure 4.51.: Distribution of the rotational phases of HK Lac versus date. The sizes of the circles are proportional to the S/N ratio of the spectra, where the average value is about 100:1.

record of the rotational phases (period= days and ephemeris= see sect...) versus the day of observation is shown in Fig. 4.51. Additional spectra in the 6430-Å region along with corresponding reference spectra, were obtained at Kitt Peak National Observatory (KPNO) with the coudé feed telescope and the TI-5 CCD in December 1997/January 1998 (marked *KPNO / TI-5* in table 4.8). The radial velocity measurements (see column $v_{\rm rad}$ in table 4.14) were obtained using the following velocity standards: β Gem (K0III, $v_{\rm r} = 3.3$ km s^{-1}) for the KPNO spectrum from JD 2450820 and 2450821, 16 Vir (K0.5III, $v_{\rm r} = 35.7$ km s^{-1}) for the KPNO spectra from JD 2 450 918, and α Ari (K2III, $v_{\rm r} = -14.3$ km s^{-1}) for all remaining KPNO and all NSO spectra.

Due to the low average radial velocity of this system, the Fe I 6411 is not vignetted on any of our observations. We therefore have three usable lines here for the NSO 1996 dataset. Unfortunately, the bad column in the Ca I 6439 region is inside the line on most exposures. Results from this regions are therefore to be taken with care, since the removal of the bad pixels (attempted only here due to the high number of affected exposures) produced small pseudo-absorption bumps similar to those of starspots.

Table 4.14.: Spectroscopic log and radial velocity data ($v_{\rm rad}$).

HJD (24+)	Phase (°)	$v_{\rm rad}$ (km s^{-1})	$\sigma_{\rm rad}$	S/N	Rotational cycle	Telescope
2450390.818	323.1	0.0	1.4	50	-	NSO
2450391.609	334.7	10.8	1.1	90	map 1	NSO
2450392.601	349.3	6.2	1.2	100	-	NSO
2450393.601	4.1	15.2	1.0	100	-	NSO
2450394.601	18.8	10.8	1.1	100	map 1	NSO
2450395.632	34.0	7.6	1.3	110	map 1	NSO
2450396.609	48.4	3.1	1.3	110	map 1	NSO
2450398.651	78.5	-14.9	1.2	100	map 1	NSO
2450399.599	92.5	-24.3	1.3	120	map 1	NSO
2450400.591	107.1	-32.1	0.9	110	map 1	NSO

Table 4.14.: Spectroscopic log of HK Lac (continued)

HJD (24+)	Phase (°)	$v_{\rm rad}$ (km s^{-1})	$\sigma_{\rm rad}$ (km s^{-1})	S/N	Rotational cycle	Telescope
2450401.591	121.8	-40.0	1.3	100	map 1	NSO
2450402.613	136.9	-47.1	1.4	100	map 1	NSO
2450404.602	166.2	-58.5	1.6	100	map 1	NSO
2450405.587	180.7	-58.6	1.6	100	-	NSO
2450406.592	195.5	-55.2	1.5	100	map 1	NSO
2450407.591	210.2	-53.7	1.4	110	map 1	NSO
2450408.597	225.1	-42.8	1.7	110	map 1	NSO
2450409.583	239.6	-40.3	1.1	100	map 1	NSO
2450410.609	254.7	-29.3	1.2	110	map 1	NSO
2450411.581	269.0	-22.9	1.0	110	map 1	NSO
2450412.577	283.7	-16.0	1.0	120	map 1	NSO
2450413.574	298.4	-7.0	0.7	100	map 1	NSO
2450414.579	313.2	0.1	0.8	100	map 1	NSO
2450415.576	327.9	6.5	0.9	100	map 2	NSO
2450416.587	342.8	9.2	1.0	110	map 2	NSO
2450417.644	358.4	13.0	1.0	100	map 2	NSO
2450418.626	12.9	11.3	1.0	120	map 2	NSO
2450419.568	26.7	8.2	1.2	100	map 2	NSO
2450420.571	41.5	3.5	1.1	110	map 2	NSO
2450421.579	56.4	-2.6	0.9	100	map 2	NSO
2450422.572	71.0	-10.6	1.1	110	map 2	NSO
2450424.585	100.7	-26.1	1.3	110	map 2	NSO
2450425.573	115.2	-35.6	1.2	110	map 2	NSO
2450426.596	130.3	-42.3	1.4	110	map 2	NSO
2450427.575	144.7	-48.7	1.4	110	map 2	NSO
2450429.574	174.2	-55.5	1.2	110	map 2	NSO
2450430.575	189.0	-55.0	1.1	110	map 2	NSO
2450432.572	218.4	-49.8	1.2	120	map 2	NSO
2450433.552	232.8	-43.1	1.1	110	map 2	NSO
2450434.571	247.8	-35.0	1.5	120	map 2	NSO
2450435.575	262.6	-26.9	1.1	120	map 2	NSO
2450436.604	277.8	-17.4	1.3	120	map 2	NSO
2450437.555	291.8	-9.5	1.0	100	-	NSO
2450440.584	336.4	9.6	1.1	100	-	NSO
2450441.573	351.0	11.6	1.3	100	-	NSO
2450446.567	64.6	-8.2	1.1	110	-	NSO
2450447.596	79.8	-19.6	1.6	80	-	NSO
2450450.579	123.7	-41.9	1.4	100	-	NSO
2450451.571	138.4	-47.4	1.5	100	-	NSO
2450453.588	168.1	-50.8	2.3	50	-	NSO
2450457.590	227.1	-46.7	1.4	100	-	NSO
2450809.663	15.5	8.6	1.7	140	map 4	KPNO/TI-5
2450810.626	29.7	7.3	1.3	140	map 4	KPNO/TI-5

Table 4.14.: Spectroscopic log of HK Lac (continued)

HJD (24+)	Phase (°)	$v_{\rm rad}$ (km s^{-1})	$\sigma_{\rm rad}$	S/N	Rotational cycle	Telescope
2450812.621	59.1	-4.9	1.9	80	map 4	KPNO/TI-5
2450813.621	73.8	-13.4	0.8	140	map 4	KPNO/TI-5
2450814.626	88.7	-20.8	0.5	140	map 4	KPNO/TI-5
2450816.617	118.0	-38.4	0.8	150	map 4	KPNO/TI-5
2450819.687	163.2	-56.1	1.2	100	map 4	KPNO/TI-5
2450820.638	177.3	-57.2	0.7	150	map 4	KPNO/TI-5
2450821.617	191.7	-56.5	0.6	140	map 4	KPNO/TI-5
2450825.668	251.4	-32.2	0.5	150	map 4	KPNO/TI-5
2450826.650	265.8	-24.4	0.8	140	map 4	KPNO/TI-5
2450829.620	309.6	-0.1	0.5	130	map 4	KPNO/TI-5
2450832.592	353.4	11.2	0.6	130	map 4	KPNO/TI-5
2450832.592	353.4	11.2	0.6	130	map 4	KPNO/TI-5
2450917.998	172.0	-57.4	0.5	-	-	KPNO/F3KB

4.6.3. Time-series Doppler imaging

Due to the long rotation period, only two independent Doppler images can be constructed with the NSO 1996 data set, see column *Rotational cycle* in table 4.14. A few observations with an acceptable quality are left out here, but will be used in section 4.6.3 to lengthen the baseline of the observations. Unfortunately, a cosmetic defect on the CCD-chip affects the Ca I 6439 region of most of the spectra. We therefore don't use this line for average Doppler images displayed in figures 4.56 and 4.57.

The distribution of the spots in the average maps of the two rotations covered by the NSO 1996 data is similar, but a phase shift is noticeable. We used the orbital period to compute this map, and it is obvious that the photosphere does not rotate with that exact period. From looking on those maps it appears to be impossible to extract differential rotation information, since the spots are located at a narrow latitude band around 50–60°. The image from the dataset taken one year later also has most of the spots at approximately 60°, but they are more concentrated longitudinally at $\ell \approx 150^\circ$. There are also some spots at the equator, something that is totally absent in the 1996 maps.

Comparing the average maps from the two seasons, it can be noted that the variation of the lightcurve amplitude form about $0\overset{\rm m}{.}1$ in 1996 to $0\overset{\rm m}{.}2$ in 1997/98 is due to a higher spot concentration in the latter case. The longitudinal separations of the spots are compatible with the approximately 120° reported by Oláh et al. (1997) using photometric two-spot modeling. But the picture seems to be more complicated, and there is no polar cap visible in our Doppler images. The majority of the observed spots is at higher latitudes than on the sun, but they are isolated and do not quite reach the pole.

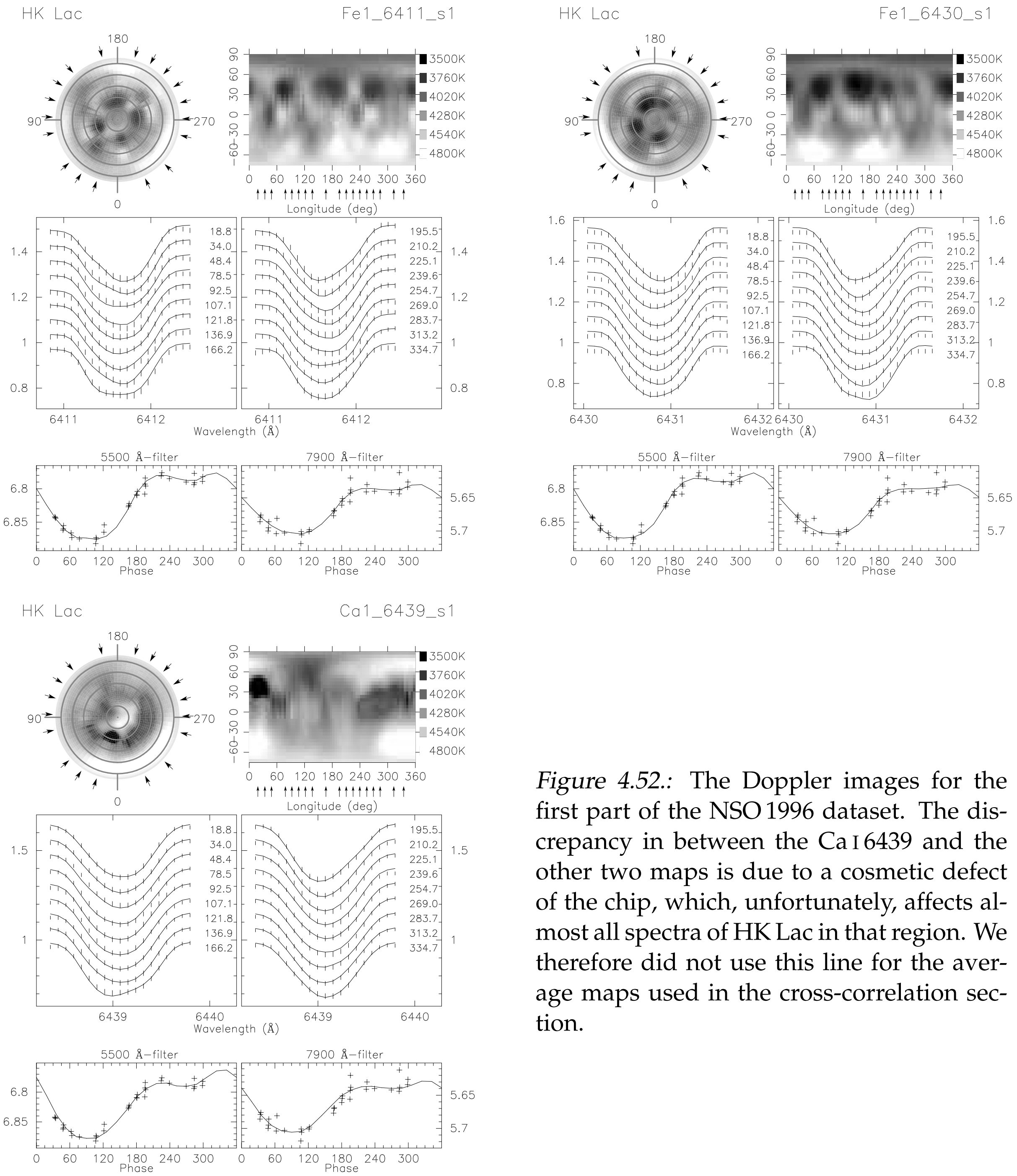

Figure 4.52.: The Doppler images for the first part of the NSO 1996 dataset. The discrepancy in between the Ca I 6439 and the other two maps is due to a cosmetic defect of the chip, which, unfortunately, affects almost all spectra of HK Lac in that region. We therefore did not use this line for the average maps used in the cross-correlation section.

Cross-correlations

The cross-correlation images of the individual Doppler images are not very conclusive, and are therefore omitted here. We try to use the recipe of adding cross-correlation images of subframes as described earlier. 21 subsets of the NSO 1996 data sets were formed, each spanning approximately one stellar rotation period. A total of 15 cross-correlation images were derived from these subsets for each of the three spectral regions by correlating the first with the seventh subset-image, the second with the eighth subset-image and so on. The (all together 45) images

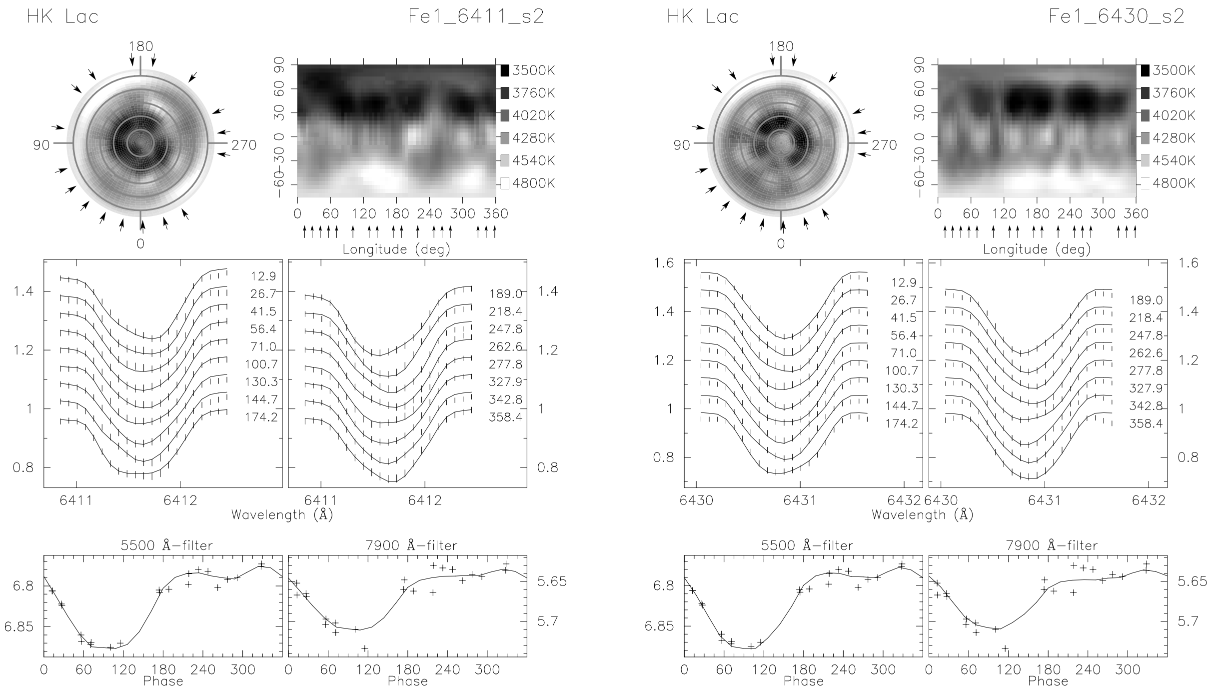

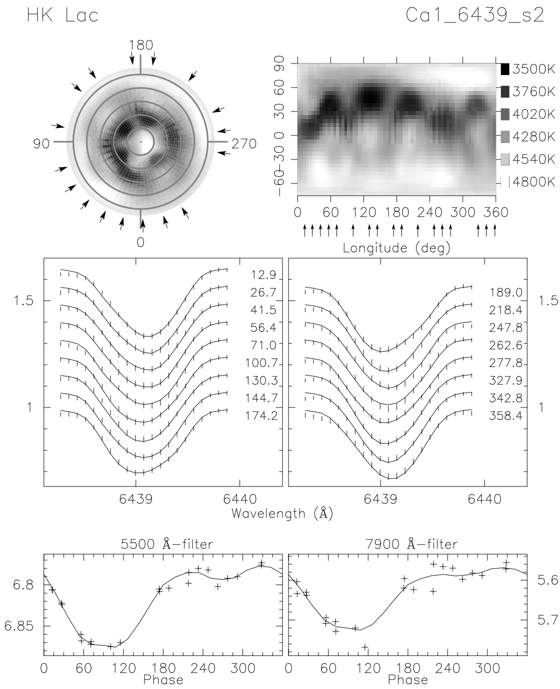

Figure 4.53.: Same as figure 4.52, but for the second part of the NSO 1996 dataset.

we obtained this way were then averaged, where the lowest and highest 15% (=2) of the pixels were rejected.

Figure 4.58 shows the average cross-correlation images for each spectral region and for the grand-average of those three. The positions of the peaks of the cross-correlation functions are marked with a dot and an error bar proportional to the FWHM of the Gaussian fit used to obtain that value. The thick solid line also shown in these graphs is the differential rotation function for α=−0.05, a value that is derived as plausible in the next section.

All four cross-correlation images show a trend for anti-solar differential rota-

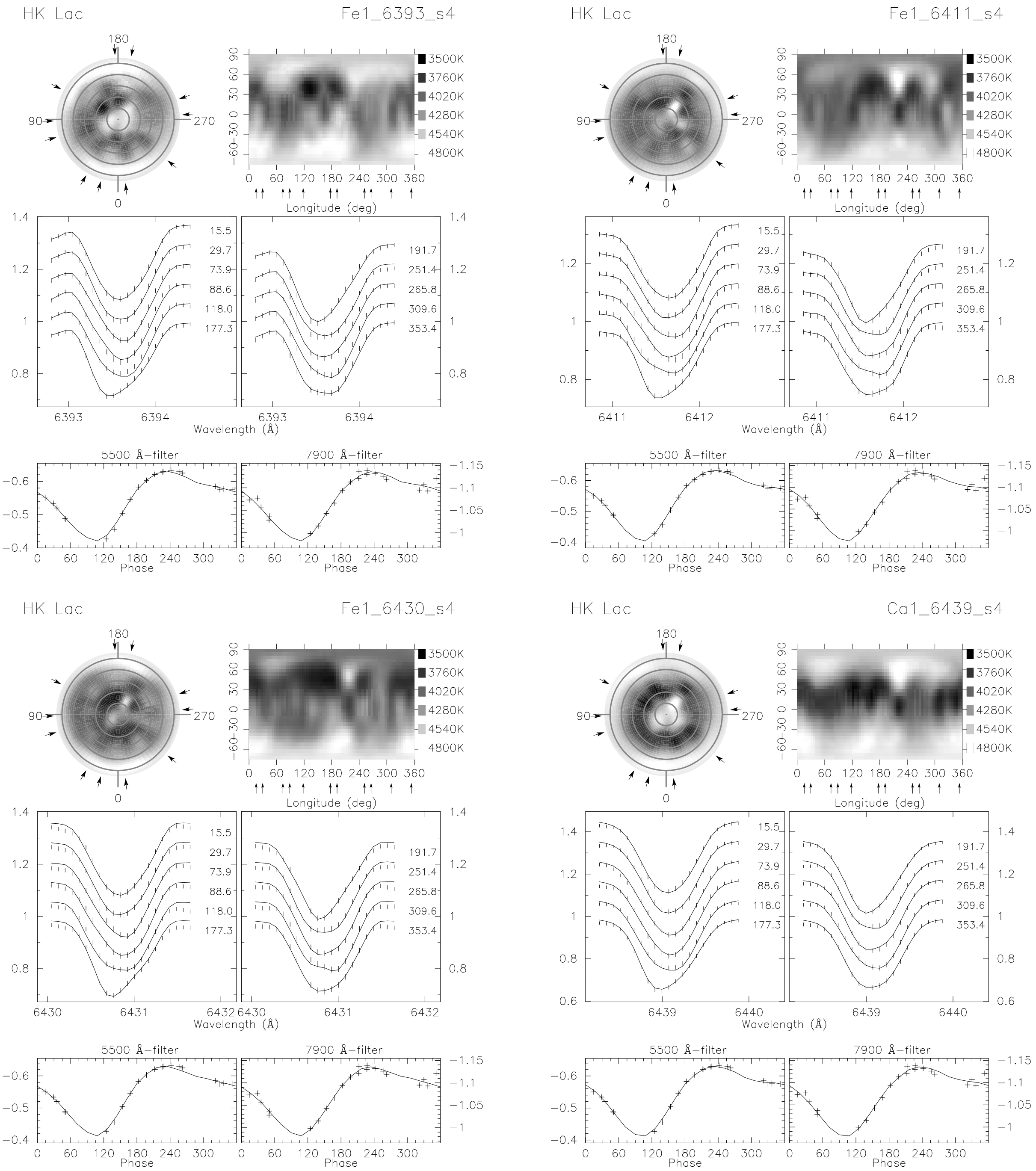

HK Lac Fe1_6393_s4

HK Lac Fe1_6411_s4

HK Lac Fe1_6430_s4

HK Lac Ca1_6439_s4

Figure 4.54.: The Doppler images for the KPNO 1996/97 dataset.

tion, but no simple $\sin^2$ function can be seen in the images. The smoothest trend is seen in the average image, which suggests that the signal is either buried in the noise of the data or masked by spot variations happening at timescales below two rotations. The Ca I 6439 image should not be taken too seriously, since it suffers from a CCD-chip defect that produces spurious spots in some cases. Along with the Gaussian-fits to the cross-correlation functions, a differential rotation law corresponding to α=−0.05 is plotted in figure 4.58 to demonstrate that it would fit the data. The only conclusions that can be drawn from these images are, that there

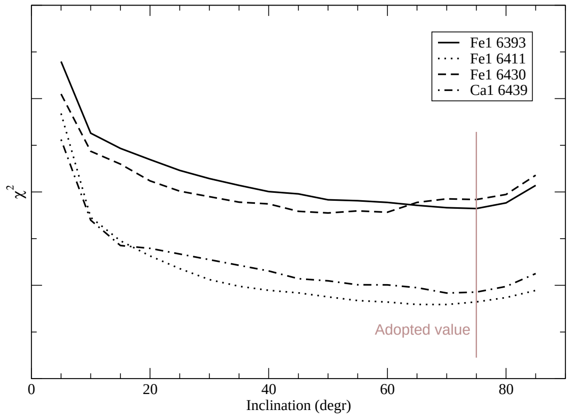

Figure 4.55.: Parameter variation of the inclination angle using the KPNO 1997/98 data set. The minimum appears to be somewhat bigger than 70°, we adopted 75° (see text).

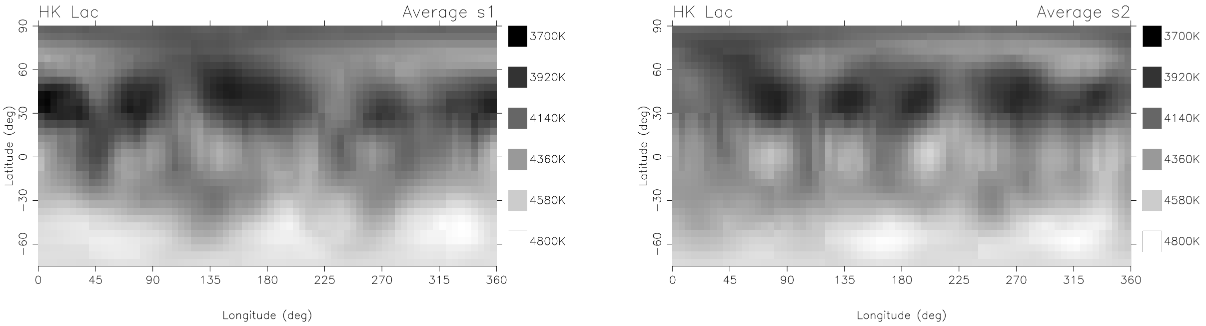

Figure 4.56.: The average Doppler images for the NSO 1996 data set. Each of the two images is the average of two Doppler images from the Fe I 6411 and Fe I 6430 spectral regions, respectively. The images from the Ca I 6439 regions were not used due to the CCD-chip defect that influences almost all of the spectra in that region.

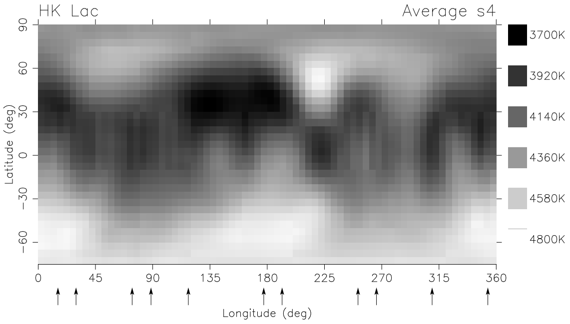

Figure 4.57.: The average Doppler image for the KPNO 97/98 data set. The image was averaged from the Fe I 6393, Fe I 6411, Fe I 6430, and the Ca I 6439 line regions.

seems to be spot-variations on very short time scales, since the technique used here recovered differential rotation on other stars with comparable data quality. But the fact that the average cross-correlation image appears to be more systematic than the individual ones suggests that besides these short-term spot variations there is latitude-dependent differential rotation in a anti-solar sense.

Differential rotation measurement using TempMap

In order to detect surface evolution or differential rotation with the cross correlation method, one needs two consecutive images. In the case of HK Lac this means almost two months of daily observations. The dataset of HK Lac collected in 1997/98 spans exactly one rotation period, thus it can not be used this way. Since

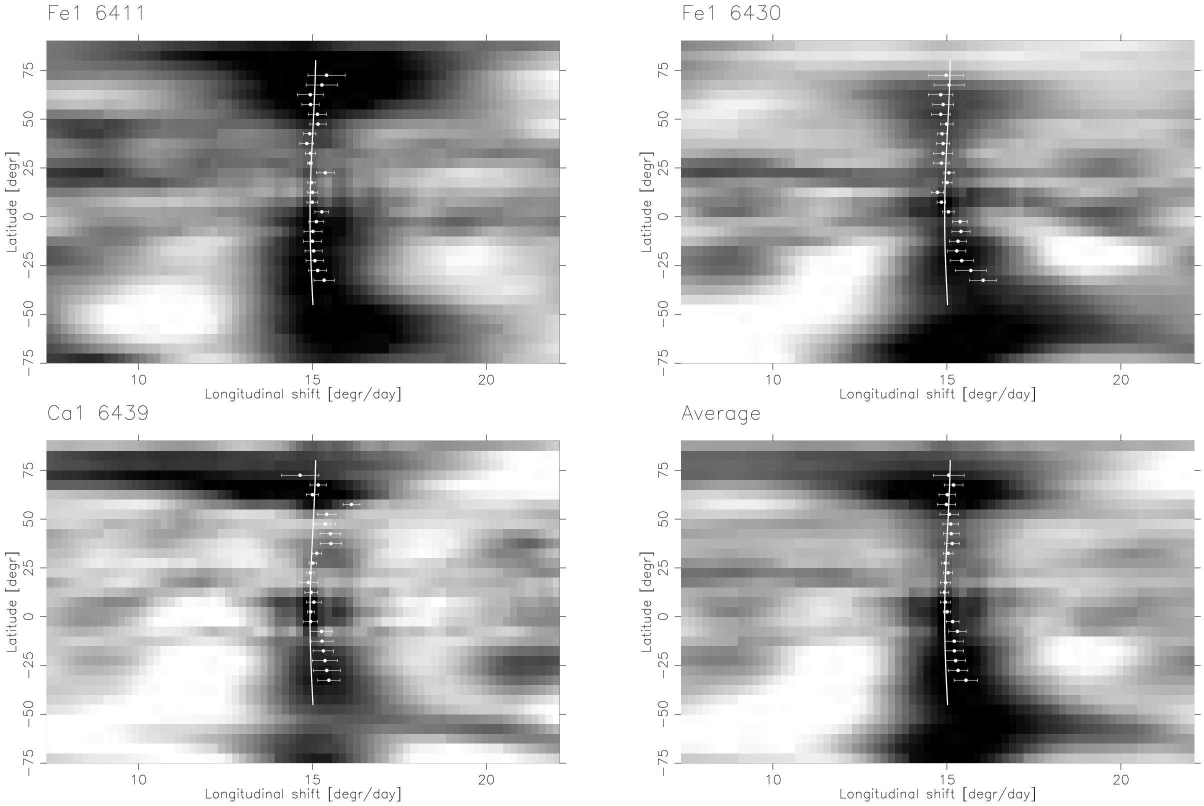

Figure 4.58.: Cross correlation images of HK Lac using the NSO 1996 data set and the spectral lines Fe I 6411, Fe I 6430, Ca I 6439, and the average of the first two. Each image is the average of 15 individual cross correlation that were computed from 21 subsets of the data, each spanning approximately one rotation period. The thick solid line represents a differential rotation law with α=$-$0.05. See text for details.

it has a slightly higher spectral resolution and significantly higher signal/noise ration, we attempted to find the correct differential rotation value by introduction of the differential rotation parameter α as an external parameter for our Doppler imaging code TEMPMAP.

We constructed a two-dimensional parameter space with α and P_{equ}, and varied α from -0.25 to 0.1, and P_{equ} from 23.8 to 24.8 days. For each parameter pair one Doppler image was computed and the quality of the fit to the spectral data (χ^2) was chosen as a quality measure. The results are shown in figure 4.59 for the four individual spectral line regions available for this data set. The results are comparable, but it is hard to draw a firm conclusion out of these four images. All of them prefer negative values for α, but the equatorial period is not very well constrained. This can be explained by the dominance of the Doppler image (see figure 4.56 and 4.57) by one large spot at approximately 60° latitude. Such a single spot would create an almost vertical line (slightly tilted forward) in a χ 2 map (see figure A.7 as an illustration). Averaging these four images (figure 4.60) brings this effect out more clearly. There seems to be evidence for a minimum at P_{equ}=24.2±0.2 and α=$-$0.05±0.05, but this result needs to be confirmed using more suitable data. As noted in section A.2.3, the signal expected from the differential rotation is comparable or less than the signal/noise ratio in our spectra. Averaging the four regions increases the signal a little, but spectra with a signal/noise ratio of at least 300 should be obtained for verifying these results.

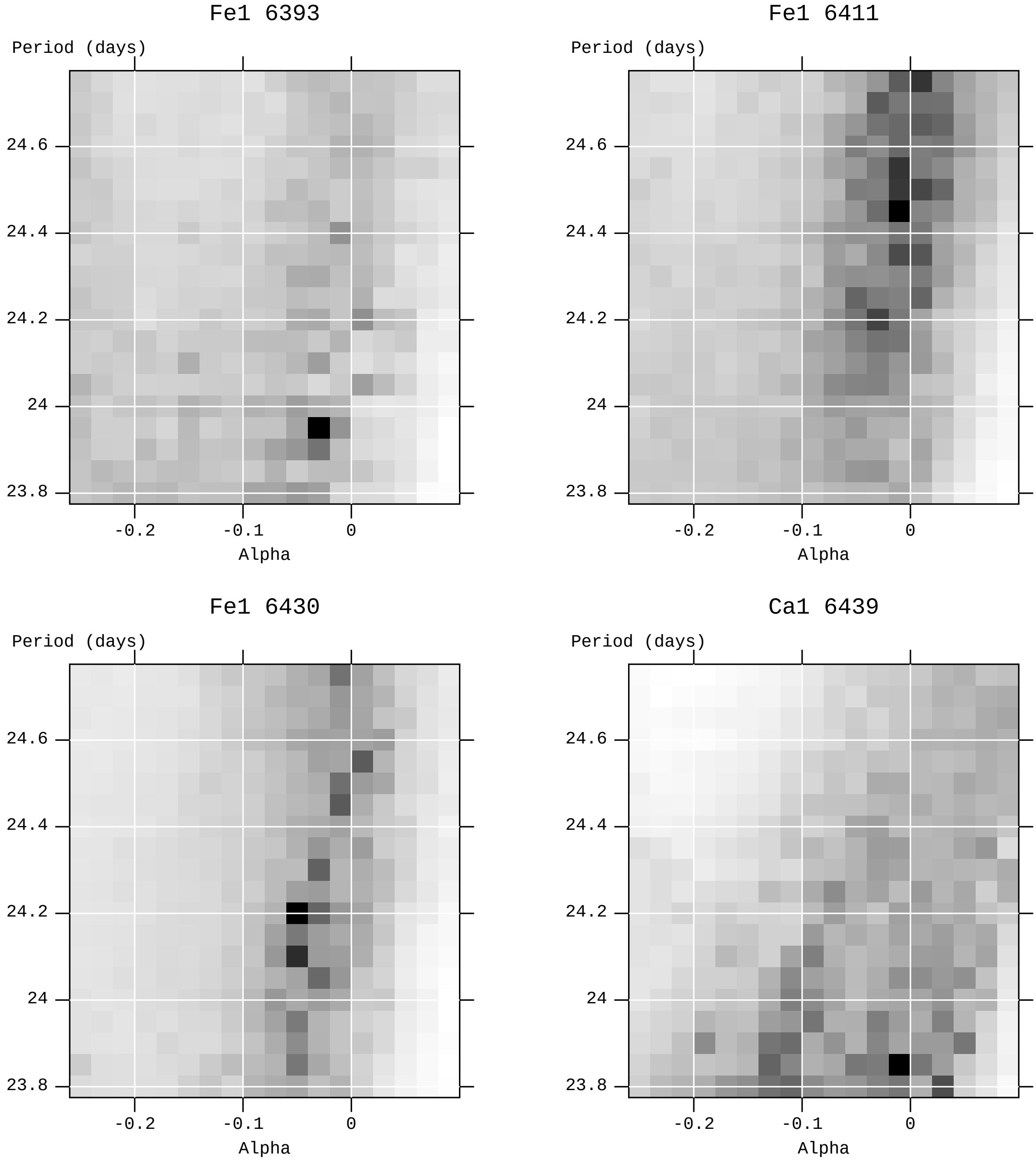

Figure 4.59.: χ^2 maps using the KPNO 1997/98 data set. From top left to bottom right: Fe I 6393, Fe I 6411, Fe I 6430, and the Ca I 6439 line.

4.6.4. Summary

The cross correlation analysis of the NSO 1996 results for HK Lac are not very conclusive. A small anti-solar differential rotation is detected in the two more

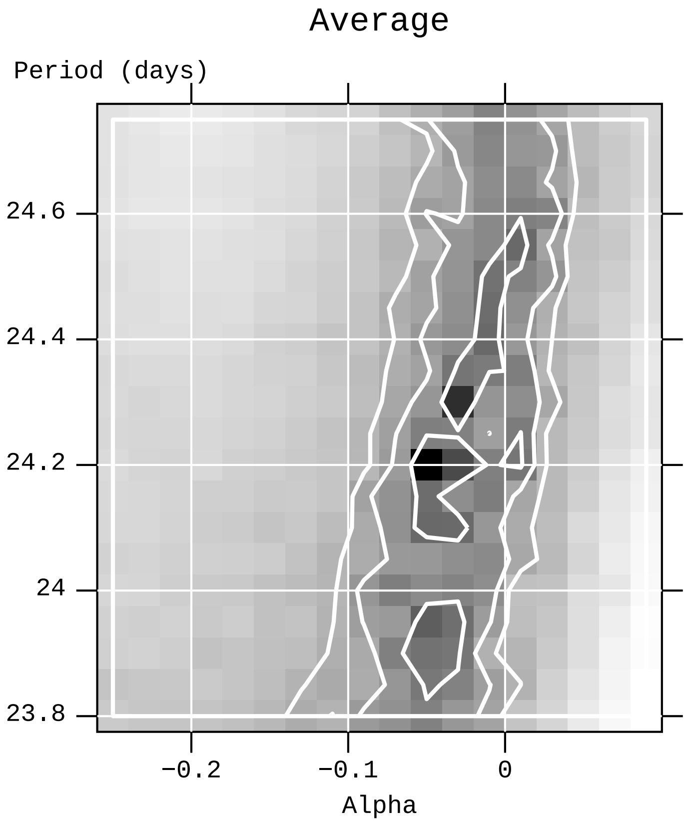

Figure 4.60.: Average χ^2 map of HK Lac. The solid lines are contours of equal χ^2. The landscape resembles that of a star with a single spot at about 60° (see section A.2.2), but it is slightly concentrated at $\alpha \approx -0.05$.

reliable lines (as mentioned above the Ca I 6439 results are unreliable and listed only as a comparison), but the errors are almost one order of magnitude bigger than the differential rotation (see table 4.15).

Table 4.15.: Derived differential rotation parameters from cross correlation analysis for HK Lac

	Ω_0	Ω_1	α
Ca I 6439	14.969	−1.084	0.0724
Fe I 6430	15.094	0.399	−0.0264
Fe I 6411	15.070	0.098	−0.0065
Average map	15.071	0.019	−0.0012
χ^2	14.88 ± 0.25	0.74 ± 0.74	−0.05 ±0.05

The results from the KPNO 1997 data are more significant, but still not fully conclusive. The most likely rotation period is 24.2±0.1 days with a differential rotation parameter α of −0.05±0.05 (see table 4.15 and figures 4.59 and 4.60). Unfortunately, this data set is not long enough to provide a sufficient overlap to fully restrict the rotation period. This limitation causes the image in figure 4.60 to be more vertically elongated (cf. appendix A.2.2). Together with the results from the cross correlation analysis, this can be seen as strong evidence for anti-solar differential rotation, but to derive conclusive results, data spanning approximately two stellar rotation with better signal-to-noise ratio and with higher spectral resolution are needed.

4.7. More stars from NSO 1996

Only a subset of the stars that were observed at NSO in 1996 are presented in this work. Some of them have more complex physical properties (e.g. double-lined binaries or stars showing an ellipticity effect) and are therefore still being worked on. Another sample of stars have been published already and the important physical parameters are summarized in this chapter. All of them share the same long observational baseline, but also share the same instrumental peculiarities. The techniques and computer programs used are essentially the same as for the stars presented in the preceding chapters, therefore I refer the reader to the descriptions that are written there.

4.7.1. KU Peg

Introduction

KU Peg (HD 218153) has been covered in a fairly recent paper by (Weber & Strassmeier 2001). Since there is no new data available to present, I restrict myself to repeat the basic stellar parameters in table 4.16. An image of the star showing the direction and magnitude estimates of surface flows is given in figure 4.61. In section 4.7.1, the cross-correlation analysis is repeated using the technique described in the previous chapters since averaging several cross correlation functions helps to reduce noise and thus should lead to a more precise measurement.

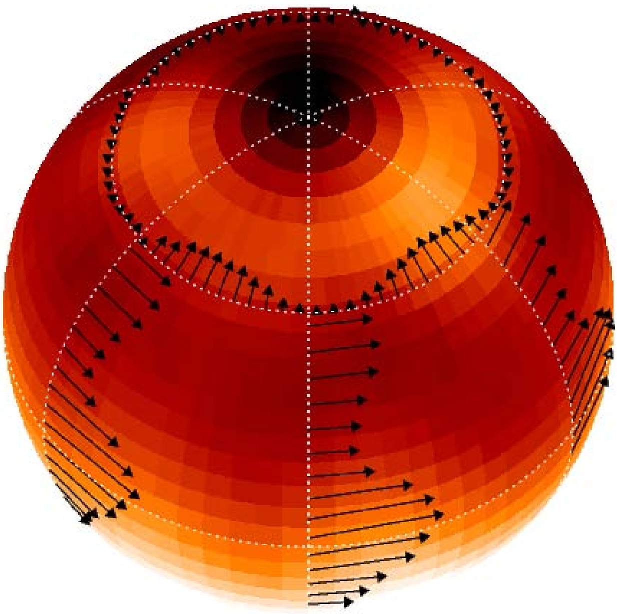

Figure 4.61.: The average Doppler image from the first rotation of KU Peg in orthographic projection at phase zero. The size and the direction of the arrows indicate the surface flows resulting from cross correlations. The basis for the cross correlations are the average images from the first and second rotation, respectively. The longitudes and latitudes at which the arrows are drawn are arbitrary because the net shifts were computed from all longitudes and latitudes (Weber & Strassmeier 2001).

Time-series Doppler imaging

(Weber & Strassmeier 2001) performed a cross-correlation analysis of two consecutive images of KU Peg. Evidence for poleward flows and for anti-solar differ-

Table 4.16.: Stellar parameters of KU Peg.

Parameter	Value
Spectral type	G9–K0 II-III
$\log g$	2.5 ± 0.5
T_{eff}	$4700 \pm 150\,\mathrm{K}$
V_{max}	$7^{\mathrm{m}}\!.61$
$(B-V)$	$1^{\mathrm{m}}\!.13 \pm 0^{\mathrm{m}}\!.02$
$(V-I)$	$1^{\mathrm{m}}\!.17 \pm 0^{\mathrm{m}}\!.01$
$v \sin i$	$28.2 \pm 0.7\mathrm{km\,s^{-1}}$
Inclination i	$50^\circ \pm 10^\circ$
Distance d	188^{+38}_{-28} pc
Radius R	$18^{+4}_{-3}\,\mathrm{R}_\odot$
Rotation period P_{orb}	24.96 ± 0.04 days
Microturbulence ξ	$2.0\,\mathrm{km\,s^{-1}}$
Macroturbulence $\zeta_{\mathrm{R}} = \zeta_{\mathrm{T}}$	$4.0\,\mathrm{km\,s^{-1}}$
$\log[Ca]$ abundance	1.0 dex below solar
$\log[Fe]$ abundance	0.6 dex below solar

ential rotation was found. Using the same dataset, I applied the average cross-correlation technique as in the other stars presented here. The dataset spanning more than two stellar rotations was divided into 21 subsets of approximately one rotation period in length and with a time distance between neighboring sets of three days in average. Image pairs with a similar time difference were then cross-correlated, and the cross-correlation function normalized to a time difference of one rotation period. A total number of 15 cross correlation images was obtained for each of the two available spectral lines, namely Fe I 6430, and Ca I 6439.

For each of the spectral lines and for the combined sample, the cross-correlation images were averaged. The 15% highest and lowest pixels (2 for the individual lines, 5 for the combined set) were rejected in the averaging process. For the three cross-correlation functions obtained that way, the peak of the correlation function for each latitude was measured using a Gaussian function. The resulting images with the cross-correlation peaks and their corresponding error are shown in figure 4.62. The parameters obtained by fitting a solar-type differential rotation pattern (see equ. A.1) are listed in table 4.17, and the function corresponding to the combined images in overplotted in figure 4.62.

The results from the time-series cross-correlation analysis confirms the result obtained by Weber & Strassmeier (2001). The average differential rotation law found is $\Omega(b) = 15.14 - 0.47 \sin^2 b$ (see table 4.17) and thus even a little smaller than the lower boundary established there. The absolute number has to be taken with caution, since the magnitudes of differential rotation are easily underestimated, mainly due to the equator-ward elongation of the reconstructed spots. The double-peaked shape of the cross-correlation function is clearly visible in both spectral lines and indicates that the surface motion pattern is more complex than a simple $\sin^2$ pattern. But to make firm conclusions, observations with higher signal level and higher spectral resolution are necessary. The same holds true for application of the “sheared image” technique.

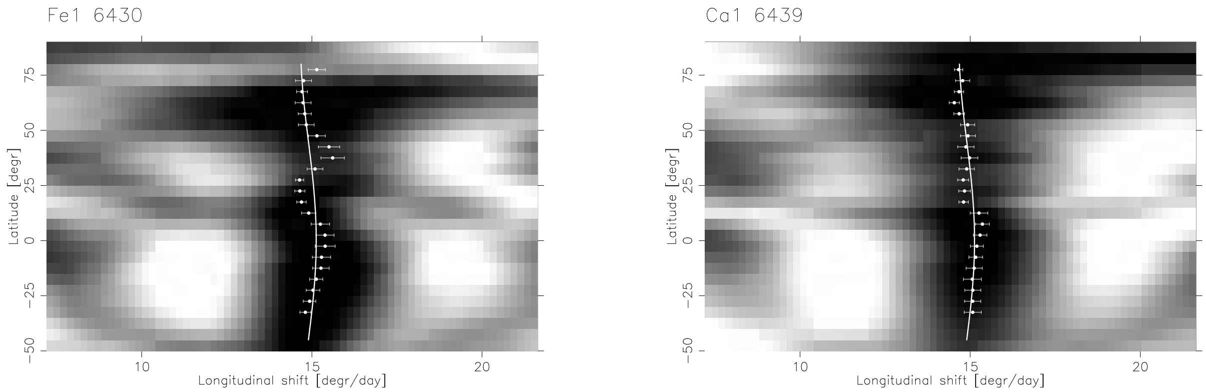

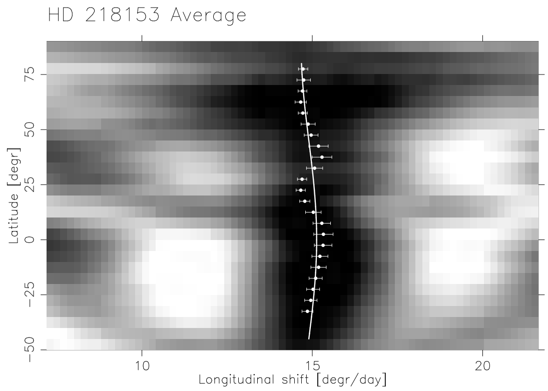

Figure 4.62.: Average cross-correlation images for the individual lines Fe I 6430 and Ca I 6439, and for the combination of the two. The data points shown are Gaussian fits measured from the cross-correlation functions shown, the solid line is a fit to the data of the combined cross-correlation measurements.

Table 4.17.: Summary of the differential rotation measurements for KU Peg

	Ω_0	Ω_1	α
Ca I 6439	15.1476	−0.5633	0.037
Fe I 6430	15.1446	−0.3828	0.025
Combined	15.1279	−0.4594	0.030
Average	15.14±0.03	−0.47±0.3	0.03±0.03

4.7.2. HD 31993

As for KU Peg, Doppler imaging results using the data presented here have been published recently (Strassmeier et al. 2003). The basic stellar parameters are listed in table 4.18, while the average surface map is shown in figure 4.63. This section therefore focuses on the different techniques used to derive a reliable differential rotation law.

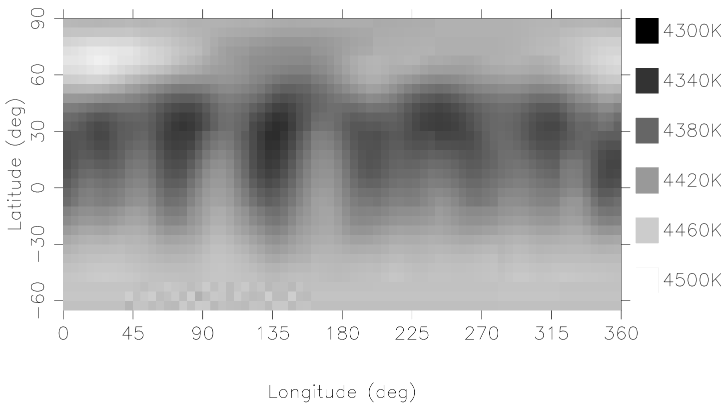

Figure 4.63.: The average Doppler image for both spectral regions and both rotations of HD 31993. (Strassmeier et al. 2003).

Table 4.18.: Stellar parameters of HD 31993.

Parameter	Value
Classification	K2III, single star
Distance (Hipparcos)	238^{+83}_{-49} pc
Luminosity, L	97^{+94}_{-36} $L_\odot$
$\log g$	$2.5^{+0.23}_{-0.42}$
$T_{\rm eff}$	4500 ± 25 K
$(B-V)_{\rm Hipparcos}$	1.254 ± 0.015 mag
$(V-I)_{\rm Hipparcos}$	1.21 ± 0.02 mag
$v\sin i$	33.2 ± 0.5 km s^{-1}
Inclination, i	$65\pm10°$
Period, $P_{\rm rot}$	25.3 ± 0.3 days
Radius, R	$16^{6}_{-4}R_\odot$
Microturbulence, ξ	2.0 km s^{-1}
Macroturbulence, $\zeta_{\rm R}=\zeta_{\rm T}$	3.0 km s^{-1}
Chemical abundances	solar (adopted)

Differential rotation

As for most stars observed at NSO in 1996, the two spectral line regions Fe I 6430 and the Ca I 6439 were used to compute Doppler images. Due to the very long rotation period of more than 25 days, exactly two independent data sets could be constructed, each covering about one stellar rotation. The overall spot distribution can be seen in figure 4.63, where all four Doppler images were averaged. The image shows very little temperature variations compared to the other stars in our sample. Since the lightcurve amplitude of this star was only about 0.01 mag at the time of the spectral observations, very low surface activity was expected. Most of the spots seem to be concentrated belt-like in an intermediate latitude range

By cross-correlation of the consecutive images, changes in the spot pattern on timescales of one stellar rotation can be tracked. For each latitude, the longitudinal band of one image is cross correlated with the corresponding band of the subsequent image. Plotting the cross-correlation functions over latitude again form an image (see figure 4.64). The peak of each cross-correlation function is then fitted with a Gaussian, and if one assumes a solar-type differential rotation law, the differential rotation parameter α and the equatorial rotation rate can be measured by a least-squares fit to that data points.

Estimating the errors in the differential rotation measurement

Since only two stellar rotations are available, the result can not be verified. We therefore chose to test the magnitude of the differential rotation by using a Monte-Carlo approach. This has the additional effect of obtaining an error estimate.

We chose to leave out one to four spectroscopic phases for each of the two spectral line regions for each of the two stellar rotations. Randomly, 50 combinations of phases were chosen for each of the four available images. Then cross-correlated corresponding pairs of images (again randomly chosen) for the first rotation with images from the second stellar rotation. We then end up with 50 cross correlation images and for each of those images we measured the positions of the peak of

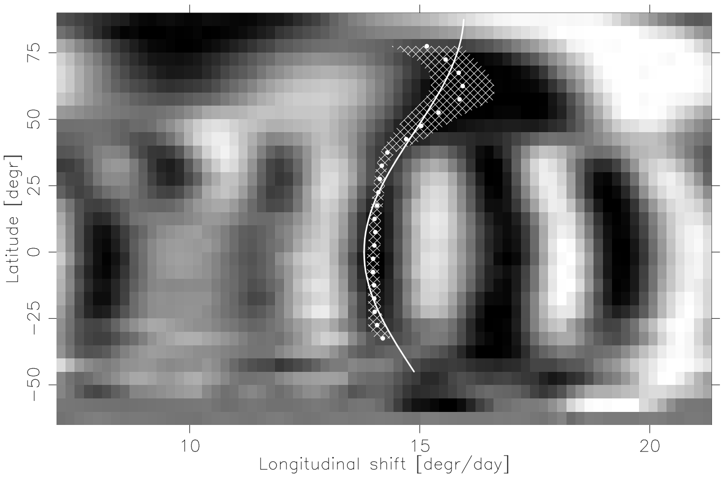

Figure 4.64.: Cross correlation image of HD 31993. The grey scale image is an average image of 100 Cross-correlations derived from Monte-Carlo variations of the maps for the two stellar rotations. The dots are the cross-correlation peaks averaged over all cross-correlations, the shaded are the corresponding uncertainty. The solid line is a least-squares fit of a solar differential rotation law ($\Omega(b) = 13.87 + 1.73 \sin^2 b$). See text for details.

the cross-correlation function for each latitude. The average of those 50 measurements gives the average longitudinal shifts per latitude bin, while the standard deviation is a measure of the uncertainties of those shifts. The result is plotted in figure 4.64 along with the corresponding (anti-)solar differential rotation law $\Omega(b) = 13.87 \pm 0.22 + (1.73 \pm 0.67) \sin^2 b$. This corresponds to a differential rotation parameter α=$-$0.125$\pm$0.050.

4.8. Discussion

Differential rotation has been measured for a number of stars in the past using various techniques. One early attempt to study the possible dependence of differential rotation with rotational period and Rossby number was done by Hall (1991). They track the periodic lightcurve variations of a sample of more than 80 stars over several decades. Changes of the period are attributed to the fact that due to differential rotation, spots located on different latitudes rotate with a different period. To convert the so obtained δP and $\mathrm{P_{rot}}$ to the differential rotation parameter α, one only needs to apply a correction about the latitudinal distribution of the spots (Hall & Henry 1994). If the spots were distributed evenly over the whole star no correction needs to be applied, but if only two spots are assumed a correction factor of two would have to be applied. Intermediate cases would be corrected with intermediate factors. The result is an exponential correlation between α and $\mathrm{P_{rot}}$ where the exponent is 0.79±0.06 (with an additional term involving the Roche filling factor). Henry et al. (1995a) updated that sample and extended it with four more stars and get a very similar result (see figure 4.65):

$$\log\alpha = -2.12(\pm 0.12) + 0.76(\pm 0.06)\log \mathrm{P_{rot}} - 0.57(\pm 0.16)F \tag{4.3}$$

F is a Roche filling factor which anti-correlates with the differential rotation parameter. Close binaries are thus expected to rotate almost rigidly, as do very fast rotators.

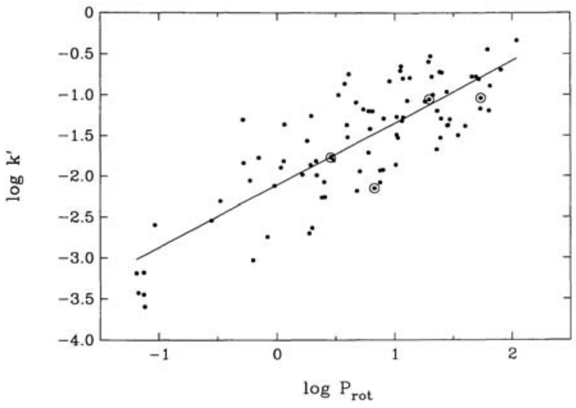

Figure 4.65.: The correlation between the differential rotation parameter α (=k') and the rotation period from Henry et al. (1995a). The slope of the regression curve is 0.76±0.06 (see text).

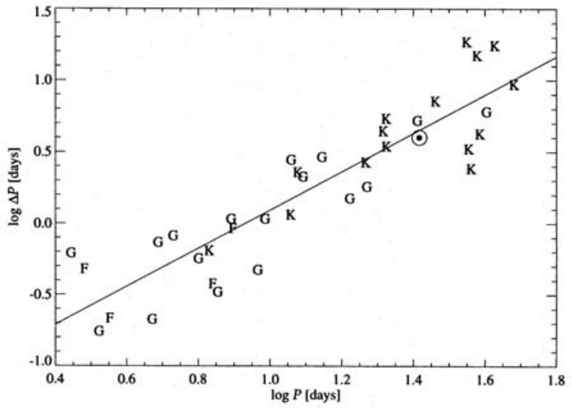

Figure 4.66.: The correlation between the differential rotation parameter (δP is a lower limit for $\alpha\times\mathrm{P_{rot}}$) and the rotation period from Donahue et al. (1996). The slope of the regression curve is 1.3±0.1, transforming to 0.3±0.1 in the α - $\mathrm{P_{rot}}$ parameter space (see text).

Donahue et al. (1996) used the Ca II H&K fluxes from the Mount Wilson study to look for variations in the rotation periods between the seasons. Many of the stars observed in this study show cyclic activity variations on short and long time scales, which are interpreted as rotation period and activity cycle period, respectively. They argue that the variation of the rotation period δP is a lower limit for the differential rotation parameter α, similar to the photometric study above. The main difference is, that the stars in that sample are selected being solar-type, and are therefore mostly main sequence stars. The result (reproduced in figure 4.66) shows a similar behavior as found above, but with a significantly smaller slope. This could be due to the systematic distributions of G stars being mostly short period, and K stars being mostly long period stars. Models for main sequence stars shown (Kitchatinov & Rüdiger 1999) that the slope is smaller for later spectral types, which could (at least qualitatively) explain the discrepancy.

Table 4.19.: A summary of differential rotation measurements and basic stellar parameters. The values are from 1: Donati et al. (2000), 2: Wolter (2004), 3: Donati & Collier Cameron (1997), 4: Barnes et al. (2000), 5: Donati et al. (2003), 6: Korhonen et al. (2004), 7: Petit et al. (2004), 8: Oláh et al. (2003), 9: Vogt & Hatzes (1991), 10: Strassmeier (1994), 11: Newton & Nunn (1951). A dash (–) marks stars discussed in the previous chapters. See text.

Star	P_{rot}	α	T_{eff}	$B-V$	R_0	bin	ref
LQ Lup	0.3100 ± 0.0002	0.0064 ± 0.001	5750	0.690	0.01517	n	1
HD 197890	0.380 ± 0.004	0.004 ± 0.002	5200	0.920	0.01765	n	2
AB Dor	0.5130	0.0046	5000	0.830	0.02334	n	3
PZ Tel	0.9450	0.0113 ± 0.002	5240	0.780	0.04407	n	4
LQ Hya	1.570 ± 0.004	0.048 ± 0.050	5070	0.933	0.07196	n	5
FK Com	2.376 ± 0.002	0.018 ± 0.003	5000	0.880	0.07653	n	6
HR 1099	2.825 ± 0.005	0.010 ± 0.005	4800	0.920	0.06304	y	5
HD 199178	3.25 ± 0.06	0.04 ± 0.01	5400	0.790	0.11192	n	7
UZ Lib	4.7683 ± 0.0007	-0.0026	4800	1.025	0.15031	y	8
UX Ari	6.40	-0.020 ± 0.002	4875	0.900	0.14400	y	9
II Peg	6.52 ± 0.16	0.04 ± 0.07	4600	1.030	0.14225	y	-
HU Vir	10.52 ± 0.02	-0.022 ± 0.006	4800	1.010	0.32744	y	10
IL Hya	12.76 ± 0.05	0.026 ± 0.016	4700	1.020	0.20075	y	-
HD 208472	22.09 ± 0.10	-0.03 ± 0.04	4900	1.066	0.70428	y	-
KU Peg	23.77 ± 0.04	0.03 ± 0.03	4700	1.130	0.18620	n	-
HK Lac	24.19 ± 0.40	-0.05 ± 0.05	4800	0.936	0.46904	y	-
IM Peg	25.0 ± 0.33	-0.04 ± 0.03	4500	1.150	0.73958	y	-
Sun	25.03	0.206	5750	0.660	1.30811	n	11
HD 31993	25.95 ± 0.41	-0.125 ± 0.05	4500	1.250	0.78869	n	-

Since these studies has been published, differential rotation has been detected on a fair number of stars using Doppler imaging. Even though the number of stars that have such measurements is still too low for a reliable statistical study, it seems still rewarding to see if trends are visible and see what parts of the parameter space are poorly covered. Table 4.19 (which is certainly not complete) lists the stars for which such measurements exist to date. The Rossby number was derived as follows: $R_0 = P_{rot}/\tau_c$, where τ_c is the convective turnover time from Gilliland

(1985). A correction of the Rossby numbers for stars above the main sequence has been applied as prescribed by Hall (1991). The values for the sun in this table are from Newton & Nunn (1951), since they measure the rotational velocities of recurring sunspots, which is close to what can be done on stars by comparing two consecutive surface images. The measurement for UZ Lib (Oláh et al. 2003) was done photometrically, but the result is backed up by Doppler images which restrict the possible values and therefore the sign is unambiguous. For UX Ari, spot positions of three spots were compared between two Doppler images taken about half a year apart, which implies spot lifetimes on that timescale, which is backed by the long term stability of the lightcurves of many spotted stars. The differential rotation values for the other stars in the table are either measured with the cross-correlation technique or with the differential rotation included in the inversion process ("sheared image") or both. For more than one measurement for a specific star, the more significant result was used, or, if still in doubt, the higher absolute value was used.

Figure 4.67 shows the distribution of the available measurements in the P_{rot}-$|\alpha|$ space. The lack of main sequence stars with long rotation periods strikes most at first. This is of course a selection effect, since the Doppler imaging method requires a minimum projected rotational velocity of approximately 15km s^{-1}, which translates to a maximum rotation period of about 3–4 days for a star with 1 $R_{\odot}$. The other outstanding feature is the lack of differential rotation of the same magnitude and direction like on the sun. The stars with comparable rotation periods as the sun exhibit anti-solar differential rotation, but this might be also a selection effect since only very luminous stars can be detected in that period regime.

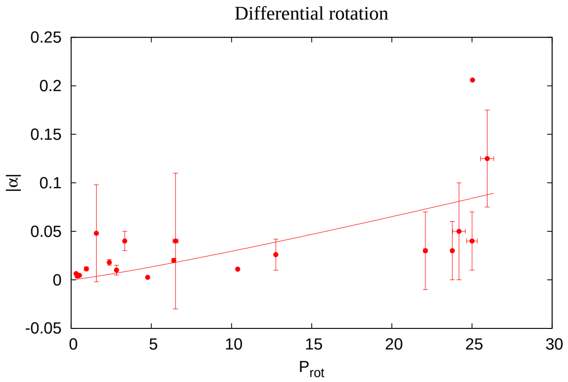

Figure 4.67.: Graphical representation of the sample in table 4.19 with error bars where available. The line is an exponential fit to all stars in the dataset with an exponent of 1.14±0.67.

To detect systematic differences between stars with a solar-like differential rotation and those with the opposite behavior, these two subsamples are analyzed separately (figure 4.68). We made an exponential fit similar to equation 4.3 to the data points and get an exponent of 0.87±0.46 for the solar case, and 5.1±4.0 for the anti-solar case. The difference of the slope is formally not significant and furthermore, the measurement of one of the low period points on the anti-solar side (UZ Lib) is based on photometry and therefore not directly comparable to the other data points (but backed up by Doppler imaging, that is why it is included here). We conclude that from our data no significant differences in the observed trends dependent on the sign of α can be detected. The overall behavior is compatible with the results in figure 4.65 (Hall 1991).

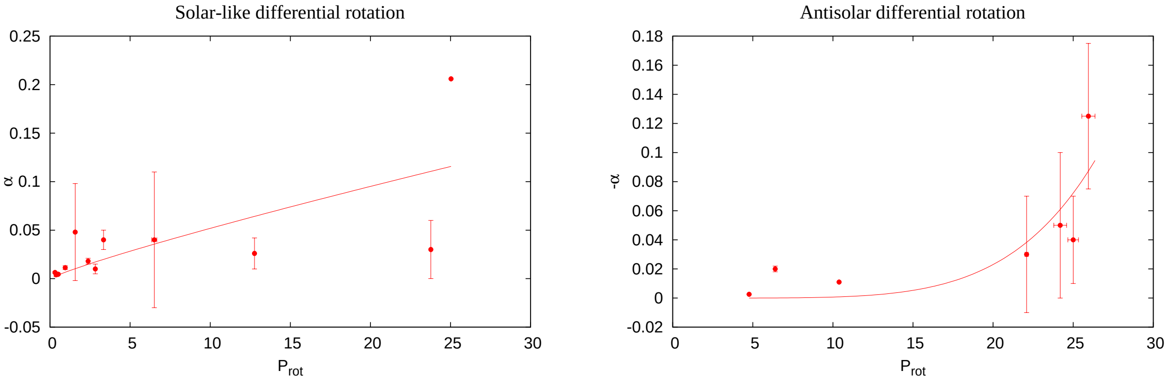

Figure 4.68.: **Left:** The correlation of the differential rotation parameter $\alpha = \delta\Omega/\Omega$ with rotation period for the stars which show solar-like differential rotation. The solid line is an exponential fit with an exponent of 0.87 ±0.46. **Right:** The same for anti-solar rotation. The solid line is the exponential function with an exponent of 5.1±4.0.

Besides the correlation of α with $\mathrm{P_{rot}}$, Henry et al. (1995a) also find correlation between α and the Roche filling factor. It has been discussed (see e.g. Moss & Tuominen 1997) that the tidal interactions in close binaries can reduce differential rotation on the surfaces of the involved stars. Again, our sample is too small to do a very detailed analysis, but one can subdivide the data set into binary and effectively single systems (the latter are real single stars and binaries where the rotation period is not locked to the orbital period). Figure 4.69 shows the binary and single stars separately, and for each of the two subsets an exponential is attempted. For the single stars the exponent is 0.62±0.32, for the binaries it is 0.63±0.26. Thus the slopes are effectively identical and also compatible to the result for the combined sample.

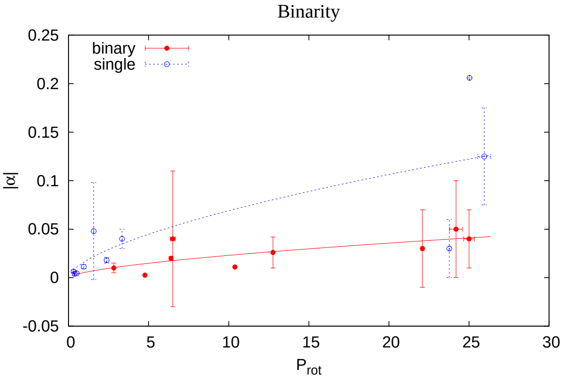

Figure 4.69.: The correlation of absolute value of the differential rotation parameter $\alpha = \delta\Omega/\Omega$ with rotation period for binaries (filled circles) and for (effectively) single stars. The exponent is 0.63±0.26 for the binaries and 0.62±0.32 for the single stars.

An attempt was made in figure 4.70 to distinguish additionally between more evolved (luminosity II and III) stars and main sequence stars and stars close to the main sequence (luminosity classes IV and V). For the single stars, the results for both subsets are compatible with the total sample of stars (Fig. 4.67 and 4.69). For the binary stars, there is no significant correlation in case of the main sequence and sub-giant stars, but a significant correlation for the giant stars. The main sequence stars thus show less differential rotation in binary systems, which can be

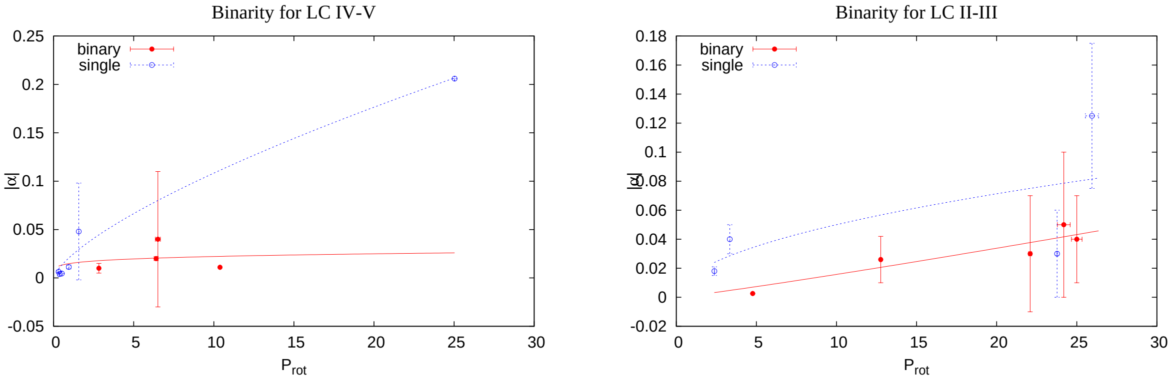

Figure 4.70.: Differential rotation parameter α with rotation period, differentiated for binarity and luminosity. For the main sequence and sub-giant stars (luminosity classes IV and V), the exponents of the fits are 0.17±0.92 for the binaries and 0.70±0.09 for the single stars. In the case of the giants (luminosity classes II and III) the exponents are 1.10±0.47 for the binaries and 0.51±0.61 for the single stars.

explained by tidal forces that inhibit the differential rotation (Moss & Tuominen 1997). In case of the giant stars, this can not be concluded from the present data set. Since many of the giant stars show anti-solar differential rotation, which is likely produced by a different mechanism than the solar-like differential rotation, this could be a selection effect. An analysis separating anti-solar and solar-like differential rotation needs to be done to clarify this, but the present data set is not big enough for this endeavor.

At last it can be noted, that all significant correlations that were found are compatible with an exponent of one, which would mean that the absolute value of the differential rotation (ΔP) is constant.

Outlook

Clearly, more complete and systematic observations (like the Mt. Wilson Ca II H&K study) of differential rotation are needed to get results that are really useful to compare them to theoretical predictions. Luckily several observing capabilities will become available that can address this issues. Space experiments that look for extraterrestrial planets and astroseismology mission both will provide high precision photometric data of many targets in their respective field of view. These data will be of very high quality and therefore ideally suited to look for photometric signatures differential rotation (Strassmeier & Oláh 2004). Even before these space based missions will launch, several robotic telescopes will go into routine operations. While photometric robotic telescopes have been around for a while (Granzer et al. 2001), spectroscopic facilities are a recent development. One new telescope that will be available soon is the STELLA robotic observatory, which is partly dedicated to stellar activity work (Strassmeier et al. 2002).

A. Tests

A.1. Inclination

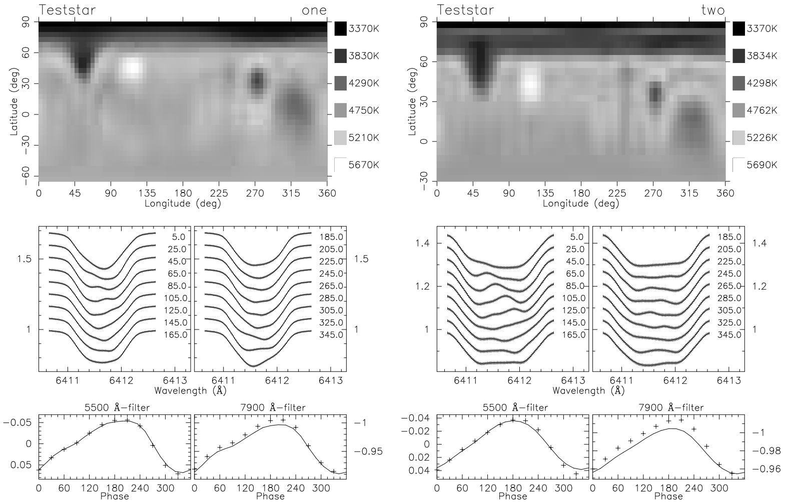

Figure A.1.: The two artificial stars used to test this method for finding the right inclination. Star number one has a inclination of 30° and $v \sin i$ of $28 \mathrm{km\,s}^{-1}$, star number two 65° and $41 \mathrm{km\,s}^{-1}$.

The inclination of a star can usually only be derived indirectly. In double stars, one can use the mass function and the fact that it is not eclipsing (otherwise the inclination of the stellar rotation value is obvious) to get a range of possible values if one assumes that the orbital rotation axis is parallel to the stellar inclination axis.(see e. g. Weber & Strassmeier 1998). Using the rotation period in combination with the projected rotational velocity $v \sin i$, one can calculate the projected stellar radius Rsini and can derive the inclination by using a radius from tables for the right spectral type or derived from distance and brightness. Since giant stars can have a very wide range of radii, this is not a practical approach to derive the inclination value, but if the inclination can be determined independently, Rsini can be used to get a good estimate for the stellar radius.

Another possibility is to use a realistic value (for example one derived by the above methods) for the inclination as a starting point for Doppler imaging, then, after having a satisfying Doppler image and line profile fits, vary the inclination while fixing all other mapping parameters and look for the inclination value which yields the minimal χ^2 (Kürster et al. 1994).

I used the two artificial stars from Rice & Strassmeier (2000) to test this approach. Fig. A.1 shows the Doppler images of those two stars along with the fits to the line profiles and the photometric data obtained with the correct inclination values of 30° and 65°, respectively. One can see clearly, that the bottom of the line profiles are flatter for the higher inclination value. The results of the variation of the inclination from 5° to 85° in steps of 5° are shown in Fig. A.2. In the case of the star with 30° inclination, the χ^2 minimum is very pronounced and at exactly 30°. For the 65° star, the minimum is at 60° and is very shallow toward higher

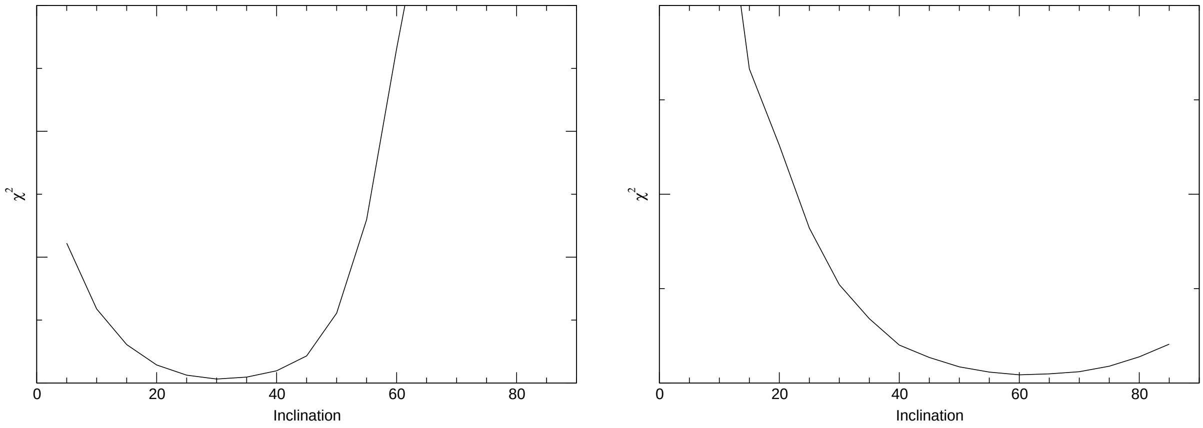

Figure A.2.: The variation of χ^2 as function of the inclination of the stellar rotation axis. Left: Test star one, with a real inclination of 30°, right: Test star two with an inclination of 65°.

inclination values. Nevertheless, this method proofs to be reliable to determine the inclination of the stellar rotation axis with an accuracy of 10° to 15°.

A.2. Differential rotation

A.2.1. Cross correlation

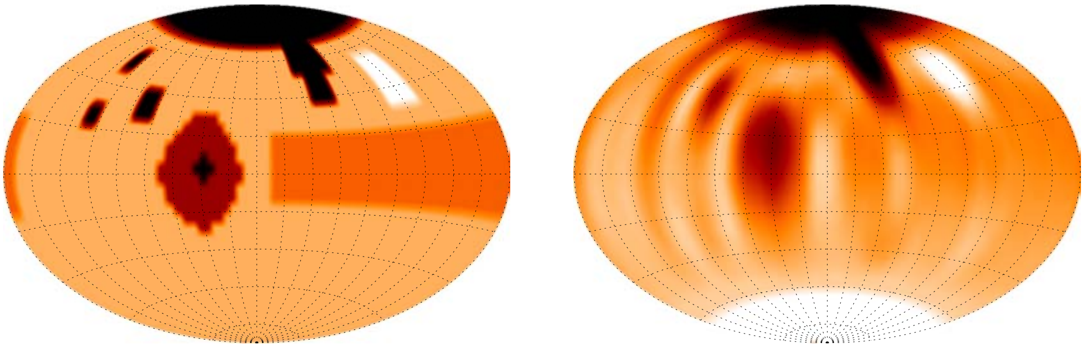

Figure A.3.: **Left.** The map used for the tests in this section. Artificial spectra have been computed at intervals representing two stellar rotations. A differential rotation with α=0.05 was assumed. **Right.** The image reconstructed using the artificial spectra. Note that the differential rotation in comparison to the original image is most noticeable at the near-to-polar spot.

Recently, differential rotation has been measured for several stars using cross-correlation techniques on Doppler images taken at different times. The first star for which differential rotation has been measured using this technique was AB Dor (Donati & Collier Cameron 1997). Other stars include IL Hya (Weber & Strassmeier 1998) and HD 218153 (Weber & Strassmeier 2001), PZ Tel (Barnes et al. 2000), Speedy Mic (Barnes et al. 2001), and σ Gem (Kővári et al. 2001).

I want to test the ability of this technique using our Doppler imaging code TEMPMAP to reconstruct a differential rotation law of the form

$$\Omega(b) = \Omega_0 - \Omega_1 \sin^2 b. \tag{A.1}$$

The differential rotation parameter α is then define (with a positive sign for a solar-type behavior of the equator rotating faster than the pole)

$$\alpha = \Omega_1 / \Omega_0 \tag{A.2}$$

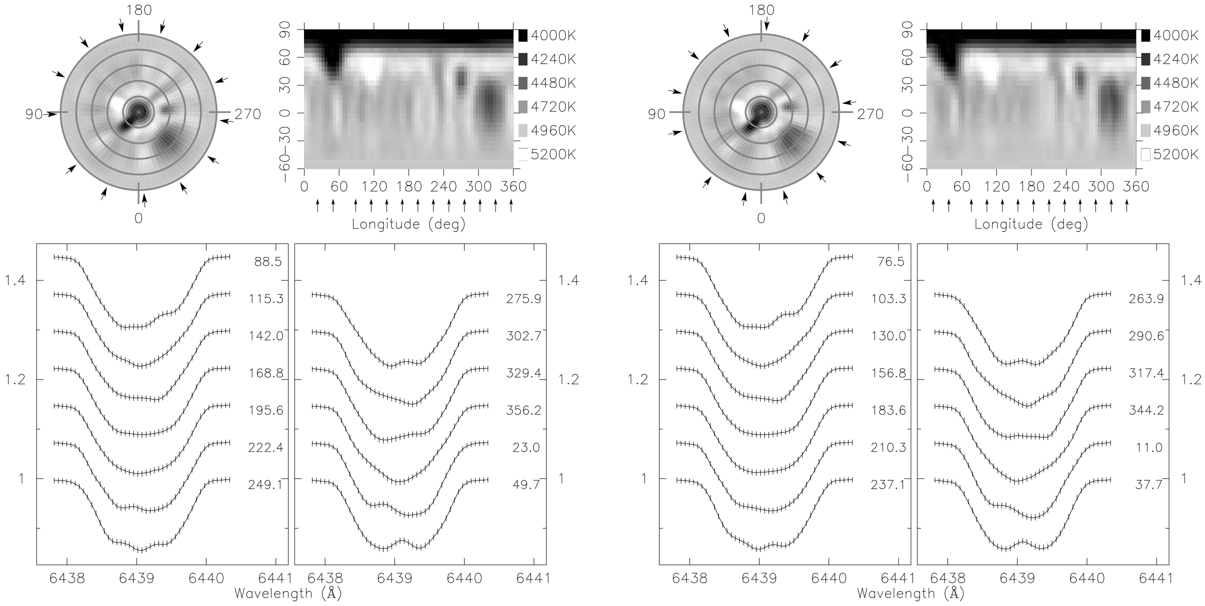

Figure A.4.: The images with the corresponding artificial spectra used to test the reconstruction of the differential rotation law. The first stellar rotation is shown at the left, the second at the right hand side.

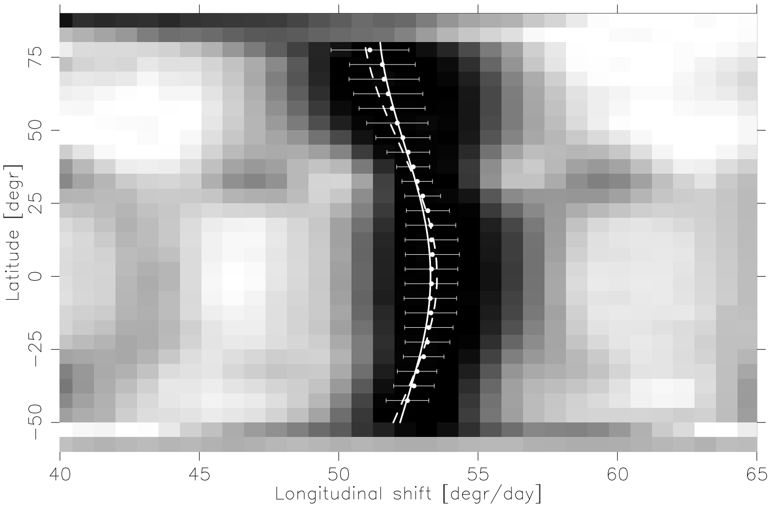

Figure A.5.: Result of the cross-correlation of the artificial images. The black line is the relation used for creating the artificial data. The dots represent the cross correlation results along with error estimates from measuring the width of the cross-correlation peak. The white line represents a east-square fit assuming the differential rotation law from Equ. A.1.

The first technique used to detect Doppler imaging was cross-correlation. Two independent images, which should be close in time since changes in the spot pattern would wash out the differential-rotation pattern quite fast, are computed.

Table A.1.: Comparison of the differential-rotation parameters derived using the above methods.

	Ω_0 (°/day)	Ω_1 (°/day)	α
Original	*53.537*	*2.677*	*0.05*
Cross-correlation	53.295±0.303	1.865±0.660	0.035±0.012
Sheared-image	53.41±0.31	2.67±1.06	0.05±0.02

Then each longitudinal band with a certain latitude from the first image is cross-correlated with the same latitude's band of the second image. The obtained cross-correlation functions for each latitude are assembled into a cross-correlation image, and the correlation peak is fitted with a Gaussian. The FWHM of this Gaussian fit is used to estimate the error of this cross-correlation.

Using the artificial star from Rice & Strassmeier (2000), we rotated it differentially according to a differential rotation law of $\Omega(b) = 53.537 - 2.677 \sin^2 b$ °/day (α=0.05). With one calculated spectral line (Ca I 6439) for each half–day for two stellar rotations (the artificial star was modeled after II Peg with a rotation period of 6.72 days), two data sets with 13 phases each were constructed. The images reconstructed from these to data sets are shown in figure A.4. Note that the features close to the pole are distorted most, since the phases were calculated using the equatorial rotation period,

Now the cross-correlation technique is applied to these two images. The resulting cross-correlation image (figure A.5 shows the overall differential-rotation pattern, but the scarce phase-coverage combined with the limited spectral resolution and signal/noise ratio (realistic conditions corresponding to our KPNO/CF observations were used) produce very elongated spots in the reconstructed images. These elongations affect especially the equatorial regions, an thus the equatorial rotation rate is underestimated (see table A.1).

A.2.2. Sheared-image method

Another possibility to reconstruct the differential rotation using Doppler imaging is to include the latitude-dependent rotation pattern in the inversion code. Due to the already large number of free parameters in Doppler imaging, the image shear is kept fixed. Calculations are done for a wide range of possible equatorial-rotation rates and α-values. Each of the resulting Doppler images have a χ^2-value associated to it which describes the goodness-of-fit to the spectral line profiles. Plotting these χ^2-values in a Period/α diagram, the best combination of these two values can be determined (see figure A.6). Since a longer timespan increases the absolute value of the shear, all 26 phases from the artificial dataset described above where used here. Using real data one would have to find a compromise between the positive effect of a larger shear and the negative effect of spot evolution.

This method performs better for our simulated data than the cross-correlation method. The results in table A.1 show an almost perfect reconstruction of the original differential rotation law. The better performance of this method is at least in part due to the added hard restriction of a $\sin^2 b$ differential rotation law. To find a more complex pattern, the cross-correlation method can not avoided, but it would take a better, more densely spaced data set than the one simulated here to really detect significant deviations from a $\sin^2 b$ behavior.

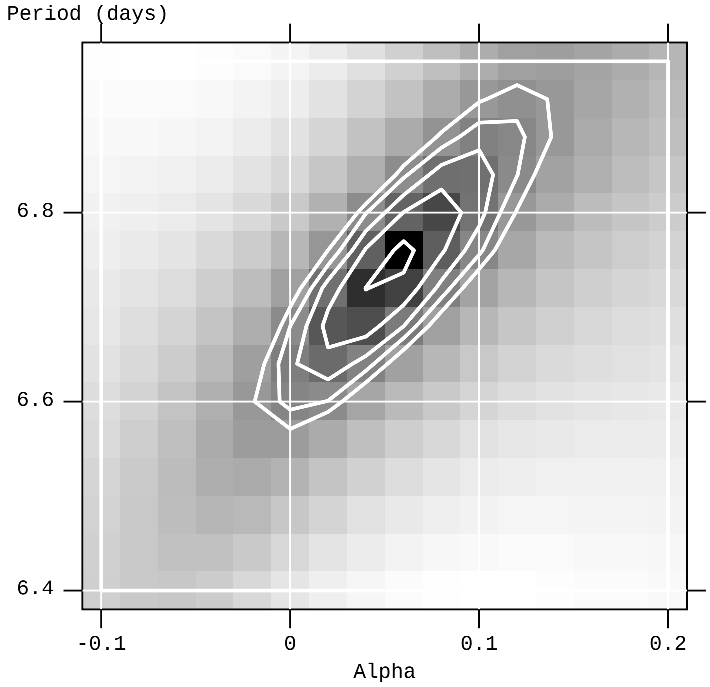

Figure A.6.: χ^2 map from the variation of the equatorial rotation period and the differential rotation parameter α. The rotation law from Equ. A.1 is assumed and the goodness of fit for each value-pair is plotted. Darker pixels represent a better fit. The contours are lines of equal goodness-of-fit with a separation of $\approx 3\sigma$.

Differential rotation with only one spot?

Imagine a star with only one spot. The only rotational parameter that can be measured using the Doppler imaging technique is the rotation rate of this spot. One can assume a equatorial rotation rate and then the differential rotation can be calculated from the difference of the spot rotation rate and the equatorial rotation rate.

Figure A.7 shows a test star with one high latitude spot, and the results obtain by applying the “sheared image” technique described above. The outcome should be a landscape centered on the thick line, which is simply the differential rotation law (see equation A.1) for a fixed latitude and the corresponding rotation rate. The slight concentration towards the (true) value α=0 is due to the elongation of the spot (e.g., Petit et al. 2002).

A.2.3. Strength of the differential rotation signal

To be better able to judge the quality of data needed to reconstruct differential rotation, a comparison between the simulated data from above with data for the same star but rigidly rotating was done. The difference of the spectral lines belonging to the same rotational phase is plotted in figure A.8 to demonstrate the order of magnitude of this effect. The maximum deviation is about 2%, but in average the signal contribution from the differential rotation alone is about 1%.

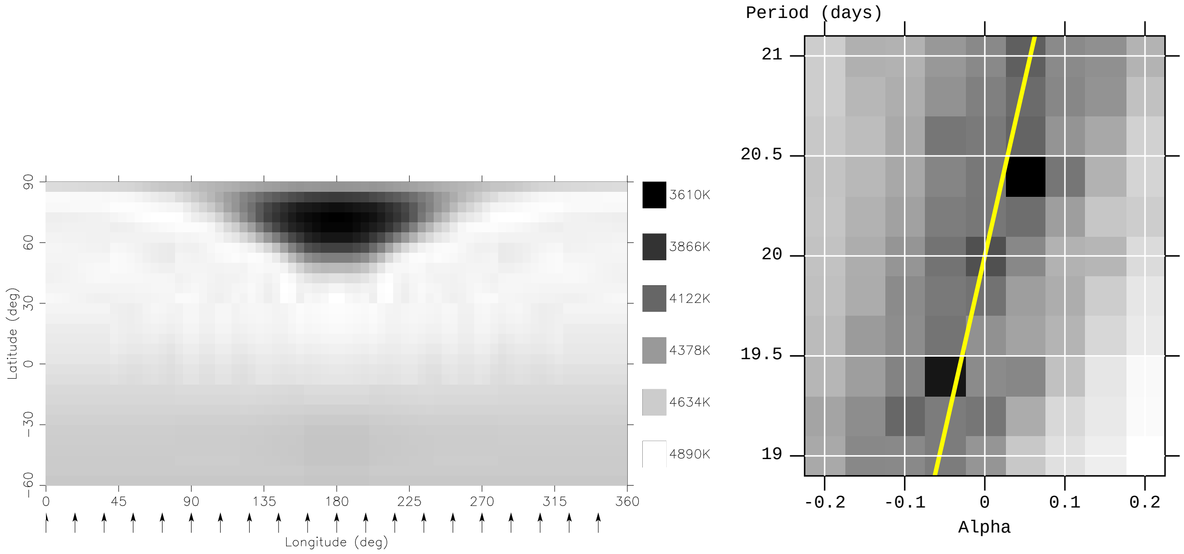

Figure A.7.: Variation of the differential rotation parameter α and the equatorial rotation period. The thick line shows the linear correlation of $alpha$ and P_{equ} for a spot at 70°. The deviation from that line and the slight concentration towards α=0 stems from the spot-extent.

This shows that the signal/noise ratio of the data should probably be at least 300 to reliably detect differential rotation of the strength assumed here (α=0.05, the solar value is about 0.2).

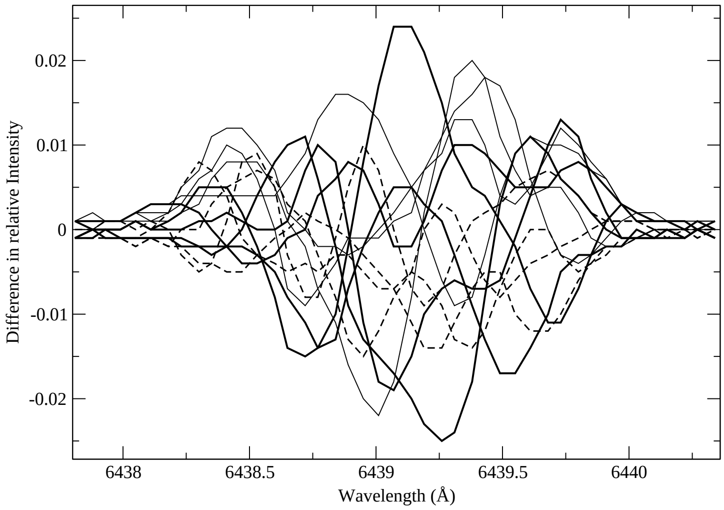

Figure A.8.: Difference of the artificial line profiles for a star with differential rotation with α=0.05 and a star which rotates rigidly. This shows the typical signal strength due to differential rotation to be approximately 1% for the simulated data presented here.

Bibliography

Allende Prieto, C. 2004, AN, (in press)

Barnes, J. R., Collier Cameron, A., James, D. J., & Donati, J.-F. 2000, MNRAS, 314, 162

Barnes, J. R., Collier Cameron, A., James, D. J., & Donati, J.-F. 2001, MNRAS, 324, 231

Beck, J. G. 2000, Sol. Phys., 191, 47

Bell, R. A. & Gustafsson, B. 1989, MNRAS, 236, 653

Berdyugina, S. V., Berdyugin, A. V., Ilyin, I., & Tuominen, I. 1998a, A&A, 340, 437

Berdyugina, S. V., Berdyugin, A. V., Ilyin, I., & Tuominen, I. 1999a, A&A, 350, 626

Berdyugina, S. V., Berdyugin, A. V., Ilyin, I., & Tuominen, I. 2000, A&A, 360, 272

Berdyugina, S. V., Ilyin, I., & Tuominen, I. 1999b, A&A, 347, 932

Berdyugina, S. V., Jankov, S., Ilyin, I., Tuominen, I., & Fekel, F. C. 1998b, A&A, 334, 863

Bessell, M. S. 1979, PASP, 91, 589

Bopp, B. W. & Fekel, F. 1977, AJ, 82, 490

Brandenburg, A. & Subramanian, K. 2004, ArXiv Astrophysics e-prints

Carrington, R. C. 1863, Observations of the spots of the sun : from November 9, 1853, to March 24, 1861, made at Redhill (Williams and Norgate, London)

Cutispoto, G. 1995, A&AS, 111, 507

da Costa, L. 2004, in Toward an International Virtual Observatory, Proceedings of the ESO/ESA/NASA/NSF Conference held in Garching, Germany, 10-14 June 2002. Edited by P.J. Quinn, and K.M. Gorski. ESO Astrophysics Symposia. Berlin: Springer, 2004, p. 153., 153–+

Donahue, R. A., Saar, S. H., & Baliunas, S. L. 1996, ApJ, 466, 384

Donati, J.-F. & Collier Cameron, A. 1997, MNRAS, 291, 1

Donati, J.-F., Collier Cameron, A., & Petit, P. 2003, MNRAS, 345, 1187

Donati, J.-F., Mengel, M., Carter, B. D., et al. 2000, MNRAS, 316, 699

Donati, J.-F., Semel, M., Carter, B. D., Rees, D. E., & Collier Cameron, A. 1997, MNRAS, 291, 658

Eggen, O. J. 1973, PASP, 85, 42

ESA. 1997, The Hipparcos Catalogue (ESA SP-1200)

Fekel, F. C. 1997, PASP, 109, 514

Fekel, F. C., Moffett, T. J., & Henry, G. W. 1986, ApJS, 60, 551

Fekel, F. C., Strassmeier, K. G., Weber, M., & Washuettl, A. 1999, A&AS, 137, 369

Gilliland, R. L. 1985, ApJ, 299, 286

Goncharskii, A. V., Stepanov, V. V., Khokhlova, V. L., & Yagola, A. G. 1982, Soviet Astronomy, 26, 690

Goncharskii, A. V., Stepanov, V. V., Kokhlova, V. L., & Yagola, A. G. 1977, Soviet Astronomy Letters, 3, 147

Granzer, T. 2004, AN, (in press)

Granzer, T., Reegen, P., & Strassmeier, K. G. 2001, AN, 322, 325

Hall, D. S. 1976, in ASSL Vol. 60: IAU Colloq. 29: Multiple Periodic Variable Stars, 287

Hall, D. S. 1991, LNP Vol. 380: IAU Colloq. 130: The Sun and Cool Stars. Activity, Magnetism, Dynamos, 353

Hall, D. S. & Henry, G. W. 1994, International Amateur-Professional Photoelectric Photometry Communications, 55, 51

Harper, W. E. 1920, Publications of the Dominion Astrophysical Observatory Victoria, 1, 203

Hatzes, A. P. 1993, Bulletin of the American Astronomical Society, 25, 874

Hauck, B. & Mermilliod, M. 1990, A&AS, 86, 107

Henry, G. W., Eaton, J. A., Hamer, J., & Hall, D. S. 1995a, ApJS, 97, 513

Henry, G. W., Fekel, F. C., & Hall, D. S. 1995b, AJ, 110, 2926

Hoyng, P. 1992, in NATO ASIC Proc. 373: The Sun: A Laboratory for Astrophysics, 99–+

Huenemoerder, D. P., Ramsey, L. W., & Buzasi, D. L. 1989, AJ, 98, 2264

Küker, M. & Stix, M. 2001, A&A, 366, 668

Kővári, Z., Strassmeier, K. G., Bartus, J., et al. 2001, A&A, 373, 199

Kővári, Z., Strassmeier, K. G., Granzer, T., et al. 2004, A&A, 417, 1047

Kitchatinov, L. L. & Rüdiger, G. 1999, A&A, 344, 911

Kitchatinov, L. L. & Rüdiger, G. 2004, AN, (in press)

Kjeldsen, H. & Frandsen, S. 1992, PASP, 104, 413

Korhonen, H., Berdyugina, S. V., Hackman, T., et al. 2004, A&A, ?, ?, submitted

Küker, M. & Rüdiger, G. 1997, A&A, 328, 253

Kürster, M., Schmitt, J. H. M. M., & Cutispoto, G. 1994, A&A, 289, 899

La Dous, C. & Giménez, A. 1994, International Ultraviolet Explorer - Uniform low dispersion archive. Chromospherically active binary stars (ESA SP-1181)

Meunier, N. 1999, ApJ, 527, 967

Moss, D. & Tuominen, I. 1997, A&A, 321, 151

Newton, H. W. & Nunn, M. L. 1951, MNRAS, 111, 413

Oláh, K., Jurcsik, J., & Strassmeier, K. G. 2003, A&A, 410, 685

Olah, K., Eaton, J. A., Hall, D. S., et al. 1985, ApJS, 108, 137

Oláh, K., Kővári, Z., Bartus, J., et al. 1997, A&A, 321, 811

Oláh, K., Kolláth, Z., & Strassmeier, K. G. 2000, A&A, 356, 643

O'Neal, D., Neff, J. E., Saar, S. H., & Mines, J. K. 2001, AJ, 122, 1954

O'Neal, D., Saar, S. M., & Neff, J. E. 1998, ApJ, 501, L73+

Ossendrijver, M. 2003, A&AR, 11, 287

Petit, P., Donati, J.-F., & Collier Cameron, A. 2002, MNRAS, 334, 374

Petit, P., Donati, J.-F., Oliveira, J. M., et al. 2004, MNRAS, 351, 826

Radick, R. R., Lockwood, G. W., Skiff, B. A., & Baliunas, S. L. 1998, ApJS, 118, 239

Randich, S., Gratton, R., & Pallavicini, R. 1993, A&A, 273, 194

Ribarik, G., Oláh, K., & Strassmeier, K. G. 2003, AN, 324, 202

Rice, J. B. & Strassmeier, K. G. 2000, A&AS, 147, 151

Rice, J. B., Wehlau, W. H., & Khokhlova, V. L. 1989, A&A, 208, 179

Rodonò, M., Messina, S., Lanza, A. F., Cutispoto, G., & Teriaca, L. 2000, A&A, 358, 624

Rüdiger, G. 1989, Differential rotation and stellar convection. Sun and the solar stars (Berlin: Akademie Verlag, 1989)

Sabbey, C. N. 1999, in ASP Conf. Ser. 172: Astronomical Data Analysis Software and Systems VIII, 129–+

Savanov, I. 2004, private communication

Schechter, P. L., Mateo, M., & Saha, A. 1993, PASP, 105, 1342

Sivaraman, K. R., Gupta, S. S., & Howard, R. F. 1993, Sol. Phys., 146, 27

Sivaraman, K. R., Sivaraman, H., Gupta, S. S., & Howard, R. F. 2003, Sol. Phys., 214, 65

Snodgrass, H. B. & Ulrich, R. K. 1990, ApJ, 351, 309

Stawikowski, A. 1994, Acta Astronomica, 44, 393

Steenbeck, M., Krause, F., & Rädler, K. H. 1966, Zeitschrift Naturforschung Teil A, 21, 369

Stix, M. 2004, The sun : an introduction (The sun : an introduction, 2nd ed., by Michael Stix. Astronomy and astrophysics library, Berlin: Springer, 2004. ISBN: 3540207414)

Strassmeier, K. G. 1994, A&A, 281, 395

Strassmeier, K. G. 2004, AN, (in press)

Strassmeier, K. G., Boyd, L. J., Epand, D. H., & Granzer, T. 1997, PASP, 109, 697

Strassmeier, K. G., Granzer, T., Weber, M., et al. 2002, in Conference Proceedings: 1st Potsdam Thinkshop on Sunspots and Starspots, 11

Strassmeier, K. G., Kratzwald, L., & Weber, M. 2003, A&A, 408, 1103

Strassmeier, K. G. & Oláh, K. 2004, in Second Eddington Workshop: Stellar structure and habitable planet finding, 9 - 11 April 2003, Palermo, Italy. Edited by F. Favata, S. Aigrain and A. Wilson. ESA SP-538, Noordwijk: ESA Publications Division, ISBN 92-9092-848-4, 2004, p. 149 - 161, 149–+

Strassmeier, K. G., Serkowitsch, E., & Granzer, T. 1999, A&AS, 140, 29

Ulrich, R. K., Boyden, J. E., Webster, L., Padilla, S. P., & Snodgrass, H. B. 1988, Sol. Phys., 117, 291

Vandame, B. 2002, in Astronomical Data Analysis II. Edited by Starck, Jean-Luc; Murtagh, Fionn D. Proceedings of the SPIE, Volume 4847, pp. 123-134 (2002)., 123–134

Vogt, S. S. 1981, ApJ, 250, 327

Vogt, S. S. & Hatzes, A. P. 1991, LNP Vol. 380: IAU Colloq. 130: The Sun and Cool Stars. Activity, Magnetism, Dynamos, 297

Washuettl, A. 1998, private communication

Weber, M. & Strassmeier, K. G. 1998, A&A, 330, 1029

Weber, M. & Strassmeier, K. G. 2001, A&A, 373, 974

White, R. L. & Percival, J. W. 1994, Bulletin of the American Astronomical Society, 26, 1513

Willson, R. C. & Mordvinov, A. V. 2003, Geophys. Res. Lett., 30, 3

Wilson, O. C. 1978, ApJ, 226, 379

Wolter, U. 2004, PhD thesis, Universität Hamburg

Zappala, R. A. & Zuccarello, F. 1991, A&A, 242, 480

Zhao, J. & Kosovichev, A. G. 2004, ApJ, 603, 776